THE EFFECT OF TRANSVERSE ELEMENTS ADDED TO GEOGRID ON PULLOUT RESISTANCE AND LOAD BEARING PERFORMANCE

Master's Thesis

Asker Alp GÜLTEKİN

Eskişehir 2024

THE EFFECT OF TRANSVERSE ELEMENTS ADDED TO GEOGRID ON PULLOUT RESISTANCE AND LOAD BEARING PERFORMANCE

Asker Alp GÜLTEKİN

Master's Thesis

Department of Civil Engineering

Programme in Geotechnics

Supervisor: Assoc. Prof. Dr. Burak EVİRGEN

Eskişehir

Eskişehir Technical University

Institute of Graduate Programs

January 2024

This thesis has been supported by the TÜBİTAK 2210-A National MSc Scholarship Program, approved by the Scientific and Technological Research Council of Türkiye.

FINAL APPROVAL FOR THESIS

This thesis titled THE EFFECT OF TRANSVERSE ELEMENTS ADDED TO GEOGRID ON PULLOUT RESISTANCE AND LOAD BEARING PERFORMANCE has been prepared and submitted by Asker Alp GÜLTEKİN in partial fulfillment of the requirements in "Eskişehir Technical University Directive on Graduate Education and Examination" for the Degree of Master's in Civil Engineering Department has been examined and approved on 19/01/2024.

Committee Members		**Title, Name and Surname**	**Signature**
Member	:	Assoc. Prof. Dr. Burak EVİRGEN	
Member	:	Prof. Dr. Ahmet TUNCAN	
Member	:	Assoc. Prof. Dr. Kamil Bekir AFACAN	

Prof. Dr. Semra KURAMA
Director of the Institute of Graduate Programs

19/01/2024

SUPERVISOR APPROVAL

Master's student Asker Alp GÜLTEKİN, whom I supervise, has completed this thesis titled THE EFFECT OF TRANSVERSE ELEMENTS ADDED TO GEOGRID ON PULLOUT RESISTANCE AND LOAD BEARING PERFORMANCE. According to my inspections, the work is scientifically and ethically appropriate for the student to the thesis defense exam.

Supervisor
Assoc. Prof. Dr. Burak EVİRGEN

ABSTRACT

THE EFFECT OF TRANSVERSE ELEMENTS ADDED TO GEOGRİD ON PULLOUT RESİSTANCE AND LOAD BEARİNG PERFORMANCE

Asker Alp GÜLTEKİN

Department of Civil Engineering

Programme in Geotechnics

Eskişehir Technical University, Institute of Graduate Programs, January 2024

Supervisor: Assoc. Prof. Dr. Burak EVİRGEN

The utilization of geosynthetics is a widely adopted practice to improve the strength of soils. Among geosynthetics, geogrids stand out due to their cellular structure, high strength, cost-effective and environmentally friendly characteristics. The internal failure mechanisms of geogrid primarily involve rupture due to tensile stress and pullout from the soil. This study aimed to increase the interaction between the geogrid and the soil, thereby enhancing pullout resistance thanks to the adopting of vertical geomembrane barriers in front of the geogrid's transverse ribs. Furthermore, the study investigated the impact of adding geogrid barriers at various distance of intervals. The effectiveness of geomembrane barriers was assessed through pullout experiments conducted in silty gravel with sand type of soil (GM) with a 99.13% compaction ratio. Results from experiments conducted under three different normal stresses highlighted the positive contribution of geomembrane barriers to pullout resistance. Additionally, reducing the distance between barriers strengthened soil-reinforcement interaction. The added barriers caused deformations in the geogrid longitudinal rib to concentrate more in the section where pullout force was applied. Beyond pullout experiments, the study examined the impact of barriers through load-bearing tests by constructing a 1.00 m high mechanically stabilized earth wall with modular block facing subjected to strip footing loading. The beneficial effects of geomembrane barriers were clearly observed concerning both load-bearing capacity and facing displacement.

Keywords: Geosynthetics, Pullout Resistance, Load Bearing Capacity, Transverse Element, Reinforced Soil.

ÖZET

GEOGRİDE EKLENEN YANAL ELEMANLARIN SIYRILMA DİRENCİ VE YÜK TAŞIMA PERFORMANSI ÜZERİNDEKİ ETKİSİ

Asker Alp GÜLTEKİN

İnşaat Mühendisliği Anabilim Dalı

Geoteknik Bilim Dalı

Eskişehir Teknik Üniversitesi, Lisansüstü Eğitim Enstitüsü, Ocak 2024

Danışman: Doç. Dr. Burak EVİRGEN

Geosentetik malzemelerin kullanımı zeminlerin mukavemetini arttırmak için yaygın olarak tercih edilen bir uygulamadır. Geosentetik malzemeler arasında geogrid, hücresel yapısı, yüksek dayanımı, uygun maliyeti ve çevre dostu özellikleri nedeniyle ön plana çıkmaktadır. Geogridlerin içsel göçme mekanizmaları çekme gerilmelerine bağlı olarak geogridin kopması ve zemin içerisinde sıyrılmasıdır. Bu çalışma, geogrid ile zemin arasındaki ilişkiyi arttırmayı ve dolayısıyla geogrid enine liflerinin önüne eklenen düşey geomembran bariyerler sayesinde sıyrılma direncini daha iyi hale getirmeyi amaçlamaktadır. Ayrıca çalışmada bariyerlerin farklı açıklıklarla eklenmesinin etkisi de incelenmiştir. Geomembran bariyerlerin etkisi, %99.13 sıkıştırma oranına sahip kum içeren siltli çakıl zemininin içerisinde gerçekleştirilen sıyrılma deneyleri aracılığıyla değerlendirilmiştir. Üç farklı normal gerilme altında yapılan deneylerden elde edilen sonuçlar, geomembran bariyerlerin sıyrılma direncine olumlu katkısını ortaya koymuştur. Ayrıca, bariyerler arasındaki mesafenin azaltılması zemin ile donatı arasındaki etkileşimi güçlendirmiştir. Eklenen bariyerler nedeniyle boyuna lifteki deformasyonlar çekme kuvvetinin uygulandığı kısımda yoğunlaşmıştır. Ayrıca bu çalışmada, 1.00 m yüksekliğinde toprakarme istinat yapısı şerit temel yüklemesine maruz bırakılarak, taşıma kapasitesi deneyleri ile bariyerlerin etkisi değerlendirilmiştir. Geomembran bariyerlerin olumlu katkısı hem taşıma kapasitesi hem de yüzey deplasmanları bakımından açıkça görülmüştür.

Anahtar Sözcükler: Geosentetikler, Sıyrılma Direnci, Taşıma Kapasitesi, Enine Eleman, Donatılı Zemin.

ACKNOWLEDGEMENTS

I wish to extend my sincere appreciation to Assoc. Prof. Dr. Burak EVİRGEN, whose extensive expertise has been instrumental throughout my academic journey, providing invaluable support in every facet.

I would like to express my profound thanks to all Eskişehir Technical University faculty members who generously shared their knowledge and served as mentors during both my undergraduate and graduate educations.

Gratitude is also extended to the proficient staff at the Central Workshop of Eskişehir Technical University, for their integral role in facilitating my experimental studies.

Special acknowledgment is owed to Istanbul Technical Corporation for their pivotal contribution in supplying geogrid and geomembrane during the experimental phase, as well as to Danış Construction Industry and Trade Inc. for their support in soil procurement.

I extend my deep appreciation to the Scientific and Technological Research Council of Turkey (TÜBİTAK) for their support in scholarship under the TÜBİTAK 2210-A National MSc Scholarship Program.

Asker Alp GÜLTEKİN

19/01/2024

STATEMENT OF COMPLIANCE WITH ETHICAL PRINCIPLES AND RULES

I hereby truthfully declare that this thesis is an original work prepared by me; that I have behaved in accordance with the scientific ethical principles and rules throughout the stages of preparation, data collection, analysis and presentation of my work; that I have cited the sources of all the data and information that could be obtained within the scope of this study, and included these sources in the references section; and that this study has been scanned for plagiarism with "scientific plagiarism detection program" used by Eskişehir Technical University, and that "it does not have any plagiarism" whatsoever. I also declare that, if a case contrary to my declaration is detected in my work at any time, I hereby express my consent to all the ethical and legal consequences that are involved.

Asker Alp GÜLTEKİN

CONTENTS

Page

LIST OF TABLES

LIST OF FIGURES

GLOSSARY OF SYMBOLS AND ABBREVIATIONS

a	:	The Constant Coefficient Determined through Linear Regression is Found to be 0.02.
A_b	:	Bearing Area of Geogrid
ASTM	:	American Society for Testing and Materials
B	:	Thickness of the Transverse Rib
B_{eq}	:	Thickness of the Equivalent Uniform Strip Rib
C	:	Cost Increase Percentage
c	:	Cohesion
CBR	:	California Bearing Ratio
C_c	:	Coefficient of Curvature
CH	:	High Plasticty Clay
CMD	:	Counter Machine Direction
CPE	:	Chlorinated Polyethylene
CSPE	:	Chlorosulfonated Polyethylene
C_u	:	Coefficient of Uniformity
$C_{\alpha b}$	:	Interference reduction factor
DIC	:	Digital Image Correlation
D_r	:	Relative Density
D_{50}	:	Average Particle Size
EPS	:	Expanded Polystyrene
FHWA	:	The Federal Highway Administration
GM	:	Silty Gravel
G_s	:	Specific Gravity
GP	:	Poorly Graded Gravel
GW	:	Well Graded Gravel
G-A	:	Geogrid-Anchorage
HDPE	:	High Density Polyethylene
LLDPE	:	Low-Density Polyethylene
LVDT	:	Linear Variable Differential Transformer
MD	:	Machine Direction
ML	:	Silt

MSE	:	Mechanically Stabilized Earth
PET-G	:	Glycol-Modified Polyethylene Terephthalate
PG	:	Pegged-Geogrid
PIR	:	Improvement Ratios in Pullout Resistance
PIRC	:	Pullout Resistance Improvement Ratio Based on The Cost Increase Percentage
PIV	:	Particle Image Velocimetry
P_R	:	Pullout Resistance
P_{RB}	:	Bearing Resistance
P_{RS}	:	Skin Friction
R_c	:	Compaction Ratio
RVDT	:	Rotary Variable Differential Transformer
S	:	Spacing Between Transverse Ribs
SG	:	Strain Gauge
SM	:	Silty Sand
SP	:	Poorly Graded Sand
SW	:	Well Graded Sand
T_T	:	Head Tensile Force
U_T	:	Head Displacement
U_q	:	Rear Displacement
VLDPE	:	Very Low-Density Polyethylene
XPS	:	Extruded Polystyrene
γ_d	:	Dry Unit Weight
γ_{dmax}	:	Maximum Dry Unit Weight
γ_n	:	Natural Unit Weight
ρ_w	:	Density of Water
σ_a	:	Normal Stress due to Applied Load
σ_N	:	Normal Stress
σ_s	:	Normal Stress Created by Surcharge Load over the Geosynthetic
ω	:	Water Content of Soil
ω_{opt}	:	Optimum Water Content
ϕ	:	Friction Angle

1. INTRODUCTION

Ensuring the stability of the soil is one of the primary concerns for geotechnical engineers. In cases where soil stability cannot be maintained, the soil mass is prone to movement. The deterioration of stability can lead to serious situations such as slope failures and the collapse of retaining walls, resulting in both human and material losses. Soil improvement practices are implemented to increase the bearing capacity of the soil and reduce the excessive settlements. On the other hand, recognizing the insufficiency of the soil in withstanding tensile stresses, the Sumerians employed reed mats as a soil reinforcement to build statues of their kings 3500 years ago (Ziegler, 2017).

The application of materials to improve the properties of soil is known as soil reinforcement. In situations when natural soil is not strong enough to support structural loads or withstand external forces, this technique comes into prominence. Soil reinforcements are divided into two categories to be extensible and inextensible. Inextensible reinforcement is identified as a material exhibiting substantially less deformation than the surrounding soil upon failure, while extensible reinforcement refers to a material that deforms in a manner comparable to the surrounding soil (Berg et al., 2009). In mechanically stabilized earth (MSE) structures, inextensible reinforcements such as steel strips or wire mats can be used. In the mid-1980s, the utilization of geogrids as extensible reinforcements marked the introduction of MSE structures (Federal Highway Administration, 2011).

Geogrids, which are polymeric materials with open grid-like structures, have proven to be effective in strengthening the mechanical properties of soil and mitigating the potential instabilities. The main internal failure mechanisms of geogrid in reinforced soil structures are pullout and rupture. The rupture type of failure is experienced when subjected to forces that exceed their tensile strength. The pullout mechanism is depending on the skin friction between the soil-geogrid surface and the bearing resistance of transverse ribs generated by the passive resistance of the soil.

This study focused on improving the bearing resistance of the geogrid to enhance soil-reinforcement interaction. Within the scope of mitigating the risk of reinforcement pullout from the soil, several quantities of vertical geomembrane elements were introduced ahead of the transverse ribs. The investigation examined the pullout and load bearing performance of the geogrid including geomembrane barriers.

2. GEOSYNTHETICS

Introduction to the concept of soil reinforcement emerged in the mid-1960s through the utilization of soil reinforcement by French architect Henri Vidal in the construction of a retaining wall, although efforts had been made to enhance soil properties by adding various materials to the soil since ancient times (Holtz, 2004). Geosynthetics started to be used to reinforce the soil in the 1970s, followed by a rapid expansion of the use of geosynthetics, especially in recent years. The factors contributing to the increased usage of geosynthetics encompass their quality control ensured by a mass production, a rapid installation, an ease of design possibility for difficult projects, an active marketing, widespread availability, a cost competitiveness against conventional construction materials, and a reduced carbon footprint compared to traditional solutions. Geosynthetic refers to using chemically synthesized or manufactured materials relating to the earth. Almost all of the geopolymers using geosynthetic production are fabricated by the plastic industry (Koerner, 2016). The types of geopolymers produced from coal and petroleum oil are presented in the Table *2.1*. Additionally, the primary reason for not using natural fibers in geogrid production is their relatively short lifespan (Shukla & Yin, 2003).

Table 2.1. *Geopolymers used for the production of geosynthetics and their abbreviations (Shukla & Yin, 2006)*

Type of geopolymers	Abbreviations
Polypropylene	PP
Polyester	PET
Polyethylene	PE
Polyvinyl chloride	PVC
Polystyrene	PS
Polyamide	PA

2.1. Type of Geosynthetics

The categorization of geosynthetics, including geotextile, geogrid, geonet, geomembrane, geosynthetic clay liner, geofoam, and geocomposite, was explained by breaking them down into subheadings.

2.1.1. Geotextiles

The underlying reason for the production of geotextiles using synthetic fibers is attributed to the low water absorption and excellent resistance to both biological and chemical degradation (Lawrence, 2014). PP constituting almost 95.00% of it, PET, PE, and PA are the geopolymers employed for producing geotextiles. Various types of fibers due to different fabrication processes are utilized to form them (Figure *2.1*). According to the production methods, geotextiles are divided into three categories as woven, nonwoven, and knitted.

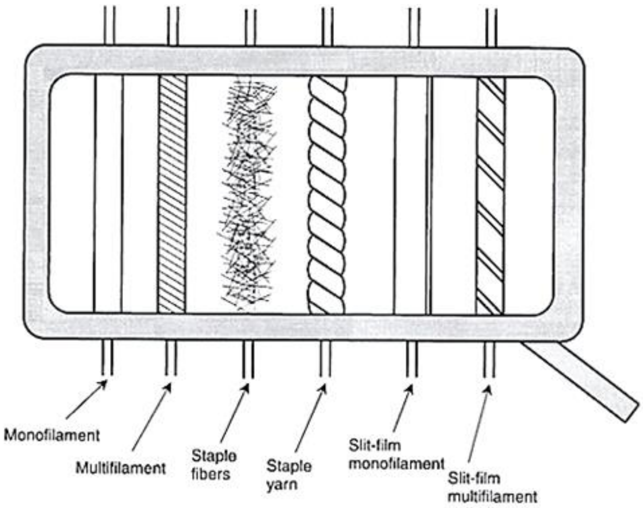

Figure 2.1. *Type of fibers (Koerner, 2016)*

2.1.1.1. Nonwoven geotextiles

Nonwoven geotextiles have the potential to be integrated with textile-related structures, resulting in multifunctional geocomposite products. These fibrous sheets feature fibers that can be oriented in a nearly random fashion. A prominent type within geosynthetics is the nonwoven needle-punched geotextile known for its thin profile and suitability for separation and filtration functions (Figure *2.2*) (Lawrence, 2014).

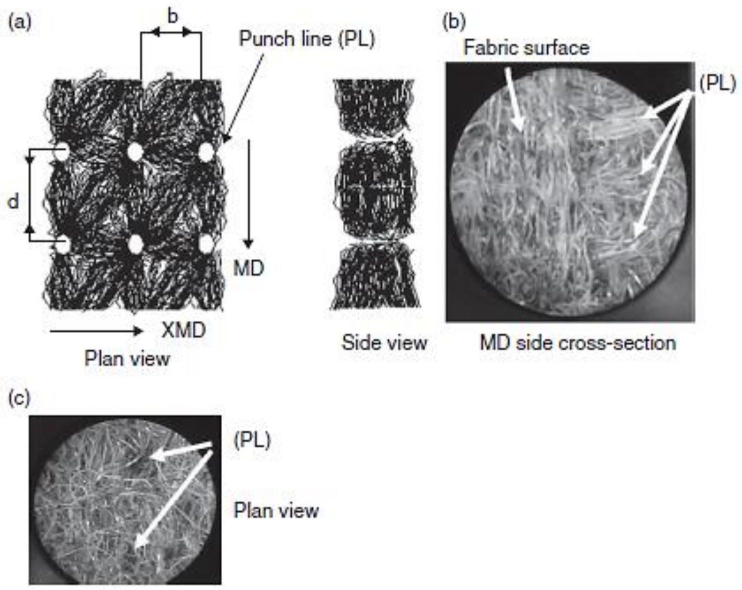

Figure 2.2. *Plan and side view of needle punched structure (Lawrence, 2014)*

2.1.1.2. Woven geotextiles

A geotextile made from PET or PP in a woven structure displays a visual pattern of two sets of parallel threads crossing each other at right angles within the fabric, as depicted in Figure 2.3. This type of geotextile exhibits high tensile strength along the warp direction, but the weft direction demonstrates limited elongation at rupture. Woven geotextiles exhibit both higher tensile resistance and California Bearing Ratio (CBR) values than nonwoven ones (Figure *2.4*) (Lawrence, 2014).

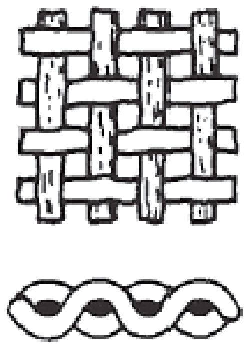

Figure 2.3. *Structure of woven geotextile (Lawrence, 2014)*

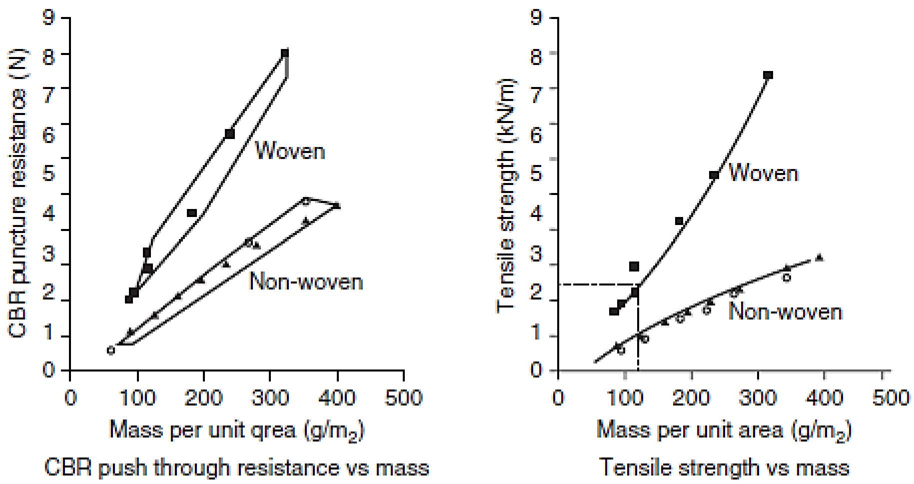

Figure 2.4. *Tensile strength and CBR values according to mass per unit area (Lawrence, 2014)*

2.1.1.3. Knitted geotextiles

Among the geosynthetic materials, knitted geotextiles are unique since they are made using complex knitting techniques. In contrast to their woven counterparts, these geotextiles have an interlocking web of loops that provide the fabric structure with special mechanical properties. Because of their extraordinary flexibility, knitted geotextiles are very useful for drainage systems, erosion control, and soil stabilization. Increased tensile strength is imparted by the knitted structure in multiple directions, improving overall performance in geotechnical engineering projects. Knitted geotextiles are a common tool in civil engineering and provide a reliable and an effective way to preserve the environment and to reinforce the soil.

2.1.2. Geogrids

The geogrid, employed as a soil reinforcement element, stand out itself through its emphasis on safety, cost-effectiveness, and ecological compatibility. A fundamental characteristic setting geogrids apart from geotextiles in diverse soil structures lies in their apertures. These cell-like openings not only increase the interaction between soil and reinforcement but also establish an interlocking effect. Furthermore, it is significant that geogrid fibers exhibit greater stiffness in comparison to geotextiles (Koerner, 2016). On the other hand, the point where longitudinal and transverse ribs touch is denoted as the "junction". In reinforced earth structures utilizing geogrids, the tensile strength assumes considerable significance, particularly at the junctions and along the longitudinal ribs.

Geogrids surpass inextensible reinforcements with their numerous features. Geogrid rolls can be effortlessly unfolded and deployed, expediting the installation process compared to the precise placement of individual strip reinforcements. They can be easily cut to the desired length without requiring any specialized procedures at the cutting points. Due to their lightweight nature, geogrids have an ease of transportability. Their strong resistance against ultraviolet rays eliminates the necessity for dedicated enclosed storage spaces at construction sites (Emir, 2005; Tezcan & Buket, 1999).

Geogrids divide categories according to production process and aperture shape. Though, there are some ways to fabricate geogrids, one of the most popular is extruded geogrid (Figure 2.5(a)). In the initial phase of extruded geogrid production, circular perforations are introduced to plates made of either polyethylene or polypropylene. These perforated plates are then subjected to an elongation inside the oven with temperatures ranging from 100°C to 140°C. Within this procedure, bidirectional stretching is employed to amplify the size of the perforations. Simultaneously, the accumulation of material is observed at the nodal points. This process gives rise to protrusions at mentioned nodal points, introducing an additional height in the third dimension to the extruded geogrid and contributing to its enhanced strength. The other most popular one is woven geogrids (Figure 2.5(b)), utilizing a wrap-knitting machine. The manufacturing process involves the uniform application of a coating material to the fabric using a precise padder, taking into account the geogrid's specific application and function. Following this, the coated fabric undergoes pre-heating in a vertical oven to prevent the coating material from adhering to the clips. Subsequent treatment in a horizontal heat chamber modifies and optimizes physical and chemical standards, enhancing heat stability and compatibility. After the drying process, the machine cuts the fabric to the desired width (Wendy Fu, 2018).

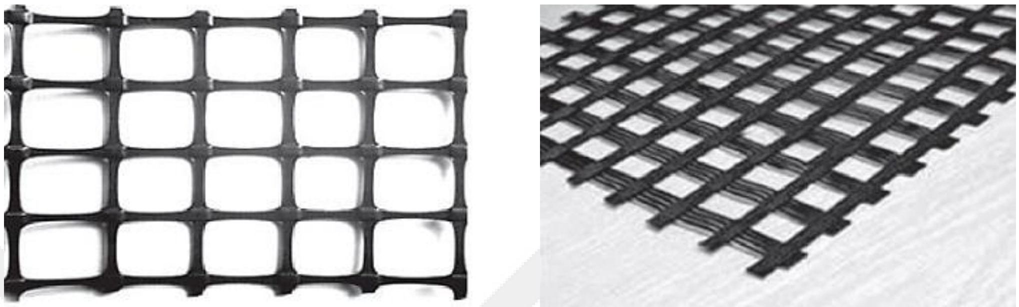

(a) (b)

Figure 2.5. *Biaxial geogrids a) Extruded and b) Woven (Lawrence, 2014)*

Geogrid type based on their shape, as seen in Figure 2.6(a), (b), and (c), was defined in subheadings.

2.1.2.1. Uniaxial geogrids

Uniaxial geogrids, usually produced using high density polyethylene (HDPE) geopolymer, derive their strength primarily from ribs oriented in one direction, while the transverse ribs having notably shorter lengths compared to the longitudinal ones. Their effectiveness lies in the superior strength of ribs in this specific direction, making them a preferred choice for applications where reinforcement and increased strength in a singular direction are essential, such as in retaining walls and slopes.

2.1.2.2. Biaxial geogrids

The most preferred type of geogrid in the industry is the biaxial geogrid. With square or rectangular apertures, it provides strength in both directions. It is used in various areas, including the foundations of heavy structures and highways. It is generally produced using PET and PP geopolymers.

2.1.2.3. Triaxial geogrids

These geogrids are emerging in the market and gaining popularity. They feature triangular apertures, providing a superior interlocking effect compared to other geogrid types.

(a) (b) (c)

Figure 2.6. *Types of geogrid due to working direction; a) Uniaxial* (Lawrence, 2014)*, b) Biaxial (http-1, Retrieved:14/01/2024), and c) Triaxial (http-2, Retrieved:10/01/2024)*

2.1.3. Geonets

Two sets of coarse, parallel, extruded plastic strands intersecting at an acute angle generate the rigid, crisscross, open grid-like sheet materials known as geonets (Figure 2.7) (Lawrence, 2014). Geonets developed by Bryan Mercer were usually used for carrying supermarket products until 1984 adapting into the geosynthetic engineering. While possessing specific tensile strengths, geonets are utilized for drainage instead of reinforcement. Additionally, they contribute to the formation of geocomposite materials when combined with diverse materials like geotextiles and geomembranes, as substantial reductions in drainage capacity may occur when soil enters the apertures of the geonet (Koerner, 2016).

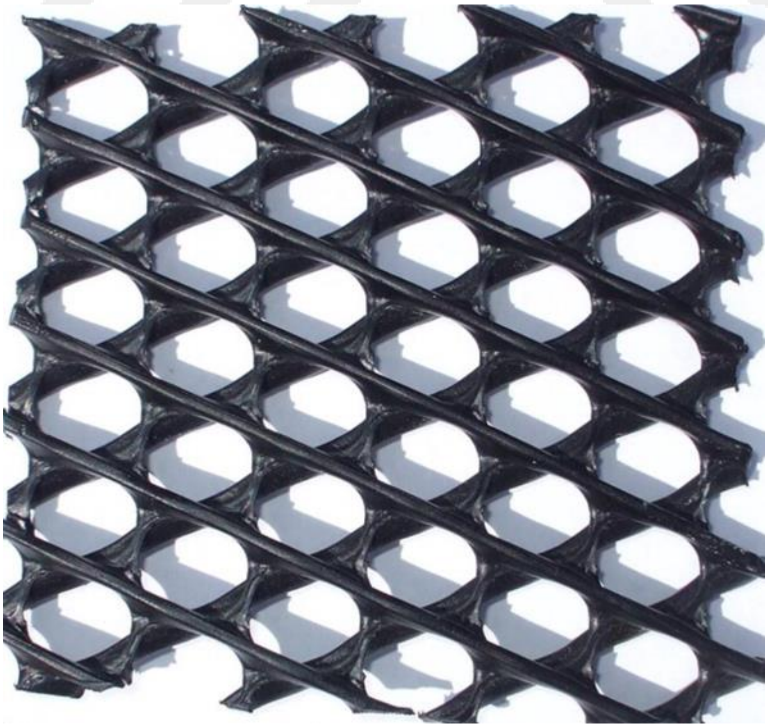

Figure 2.7. *Geonet (Dickinson et al., 2010)*

2.1.4. Geomembranes

Geomembranes can be classified in usage area, performance, and type of raw material. Geomembranes can be produced from various geopolymers such as HDPE, LLDPE (low-density polyethylene), VLDPE (very low-density polyethylene), PVC, CPE (chlorinated polyethylene), CSPE (chlorosulfonated polyethylene), PP, and many others. Waterproofness, expandability, and a high strain against rupture capacity are the key characteristics of geomembranes. The geomembrane's permeability range from 10^{-11} to 10^{-14} m/s makes it relatively impermeable, while it has a substantial deformation capacity between 200% and 1000%. Also, its low specific mass ranging from 1000 to 1300 kg/m³ is the other reason for preference. The property of its chemical inertness stands out prominently in waste storage areas. Regarding the plastic material employed, geomembranes can be sorted into thermoplastic, elastomeric, or rubber-like, and thermosetting classifications. It can be produced in situ, enabling cost savings in transportation in addition to the separation between soil and sewage (Figure 2.8). However, imperfect joints or damage to the geomembrane can cause serious problems such as punctures, ruptures, or chemical deterioration (Gamski, 1984).

Figure 2.8. *HDPE geomembrane used in sewage pond (Lavoie et al., 2020)*

2.1.5. Geosynthetic clay liners

The development of geosynthetic clay liners involves encapsulating sodium or calcium bentonite within a layer or layers of geosynthetic materials, a process integral to geotechnical engineering applications. This configuration, where bentonite is positioned between two geotextile layers, is specifically termed geotextile-based geosynthetic clay liners, displayed in Figure 2.9(a). The bonding within this system is established through techniques like adhesive bonding, needle punching, or stitch bonding. In instances where a geomembrane supports the geosynthetic clay liners (seen in Figure 2.9(b)), a non-polluting adhesive is applied to affix bentonite to the geomembrane, and during installation, the bentonite is shielded by attaching it with a thin open-weave geotextile. This arrangement is characterized by its geotechnical advantages, including rapid installation, reduced dependency on highly skilled labor, cost-effectiveness, ease of repair, and notably low hydraulic conductivity to water when properly implemented in geotechnical projects. Typically, the hydraulic conductivity of geosynthetic clay liners hinges on the inherent properties of bentonite, falling within the geotechnically relevant range of $2*10^{-12}$ to $2*10^{-10}$ m/s. The hydraulic conductivity may exhibit variation when geosynthetic clay liners interact with liquids other than water, and additional geotechnical factors influencing this property encompass aggregate size, montmorillonite content, the thickness of the adsorbed layer, prehydration, and void ratio of the mineral component (Bouazza, 2002).

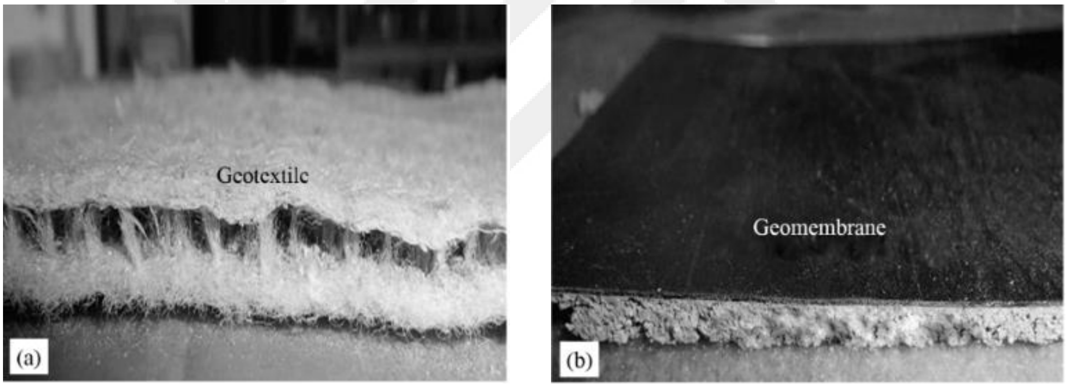

Figure 2.9. *a) Geotextile and b) Geomembrane based clay liners (Kong et al., 2017)*

2.1.6. Geofoams

Geofoam is essentially expanded polystyrene (EPS) molded into large, lightweight blocks. Another variant of geofoam is Extruded Polystyrene (XPS), produced through the expansion process of polystyrene. Geofoam blocks serve as efficient lightweight fill materials for diverse construction applications, including projects on soft soil, the construction of seating structures in stadiums and theaters, noise and vibration reduction, slope stabilization, rail embankments, bridge approaches, highways, culverts, pipelines, and subterranean structures. Geofoam plays a crucial role in substantially lessening vertical loads and preventing potential future settlement problems for underground utilities. This approach is frequently adopted in scenarios where the existing soil conditions exhibit softness or looseness, making them inadequate for supporting the required loads. Geofoam blocks, typically weighing between 150 and 300 N/m^3, offer a practical solution for construction projects, allowing for easy manual placement and resulting in cost savings and reduced construction time, as seen in Figure 2.10. The design flexibility is evident through a range of block sizes tailored to meet project needs. Proven over time, EPS Geofoam ensures predictable performance throughout the project's lifespan, offering stability without shifting or compacting like other fill materials (Khushefati et al., 2015; Mittal, 2018).

Figure 2.10. *Placement process of EPS geofoam (Puppala et al., 2019)*

2.1.7. Geocells

Geocell is recognized as economical, environmentally friendly, and sustainable. Its versatile application extends to various weather conditions and is particularly suitable for use in foundations, embankments, pavements, erosion control, etc. Geocells offer the advantages of confinement, tensioned membrane effect, and broader stress distribution, ultimately leading to enhanced bearing capacity and elastic modulus in reinforced soil. Studies have demonstrated the effectiveness of geocells in reducing permanent deformation of soil. The material's low maintenance requirements further contribute to its appeal in diverse engineering applications (Sheikh & Shah, 2021). Geocell is very easy to transport as it occupies significantly less space when in a closed state compared to when it is in an open state, as shown in Figure 2.11(a) and (b).

Figure 2.11. *Close and open state of geocell (Bagli, 2022)*

2.1.8. Geocomposites

In geotechnical engineering, geocomposites are important because they combine different materials to create new substances with specific qualities. Typically, these mixtures come from blending various geosynthetic materials, providing numerous possible combinations. For instance, in geocomposite materials made by using both geotextile and geonet, placing geotextile between the geonet and the soil addresses issues related to soil particles filling and clogging geonet openings, as seen in Figure 2.12. Strengthening and improving friction capacity can be achieved by connecting geomembrane and geogrid, both made from the same geopolymers. Additionally, when using backfill with low permeability, a geogrid geocomposite with needle-punched nonwoven geotextile can be used. This combination of geogrid enhances tensile strength and enables effective drainage in the geocomposite structure, making it valuable in geotechnical engineering (Koerner, 2016).

Figure 2.12. *Geocomposite material based on geotextile and geonet (Narejo et al., 2013)*

2.2. Functions and Applications of Geosynthetics

The different characteristics of geosynthetic types lead to their usage in various applications, aligning with their intended production purposes.

2.2.1. Separation

The primary objective of geosynthetic employment in geotechnical engineering is to facilitate the separation of distinct soil layers, particularly under the influence of applied loads that might otherwise induce undesirable blending problem. The preference for geosynthetics, predominantly geotextiles, arises from their efficiency in terms of preventing the mixing of fine and coarse soils. In the context of utilizing geogrid within clayey soil, it is recommended to accompany its placement with a thin layer of fine granular soil. The utility of separation function provides an opportunity for geogrids in clayey soils (Abdi & Zandieh, 2014). Moreover, the infiltration possibility of fine-grained soil inside the granular soil designated for drainage must be eliminated with geotextile usage, as this phenomenon has the potential about a clogging effect. The tensile strength of separation material is crucial, as it must endure sustained loads throughout its operational lifespan, while it is finding universal application between the subgrade and stone base in road construction (Figure 2.13), the subgrade and ballast in railroad engineering, and between geomembranes and sand drainage layers. Its multipurpose application extends to foundation construction, embankment soils, and interlayers within asphalt pavement, thus showing its crucial role in diverse geotechnical contexts (Koerner, 2016; Lawrence, 2014).

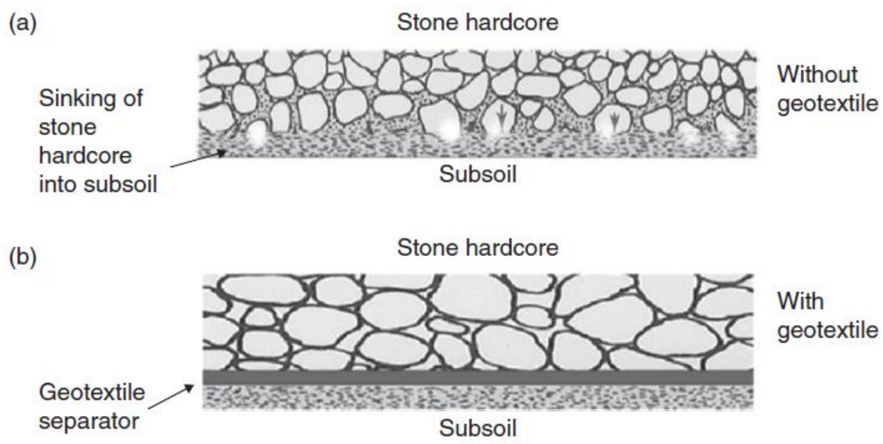

Figure 2.13. *Stone hardcore and subsoil a) Without geotextile and b) With geotextile (Lawrence, 2014)*

2.2.2. Reinforcement

Soil tends to undergo a situation of lateral displacement, leading to a reduction in the mechanical properties of the soil under external loading conditions. To reduce this decrease in lateral strength, the application of confinement becomes necessary. Geosynthetics play a crucial role in this context by mitigating the reduction in lateral strength and redistributing the excess stress concentration more uniformly, as illustrated in Figure 2.14. The transfer of shear stress to the geosynthetic is effectively managed by its tensile strength, thereby imparting increased stiffness to the soil. Geogrids and geocells are particularly effective for reinforcement due to their apertures, creating a confinement mechanism known as the interlocking effect. Geotextiles can also serve as reinforcement, especially in silty and clayey soils, such as over soft soil for road construction, landfills, and airfields. Additionally, geogrids find application in asphalt to mitigate reflection cracks (Evirgen et al., 2021). Other notable applications of geogrids include their use in embankments, earth dams, MSE walls, and with ballast in railroad construction, among various other applications (Zornberg, 2017).

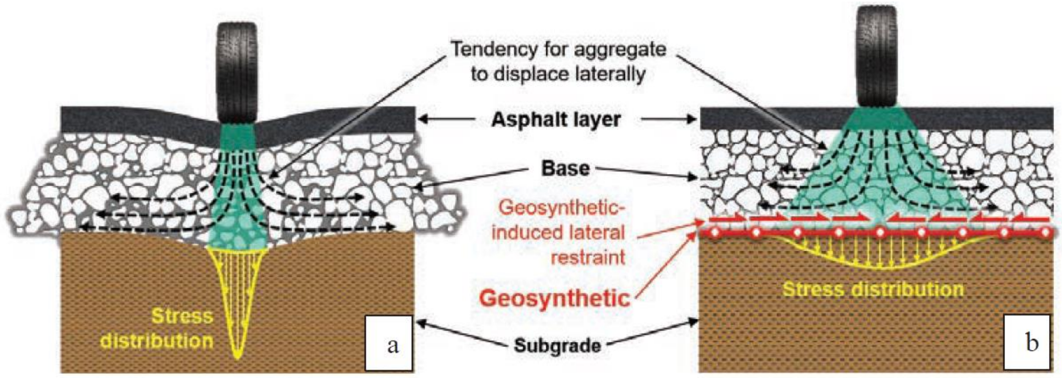

Figure 2.14. *Road under traffic load a) Without geosynthetic and b) With geosynthetic (Zornberg, 2017)*

2.2.3. Filtration

Certain types of geosynthetics serve as filters, allowing liquids to pass through while preventing the passage of soil particles (Figure 2.15). Plane geosynthetics possess sufficient permeability to facilitate flow. Therefore, the pore size of these materials must be appropriately calibrated to prevent the passage of fine soil particles while maintaining adequate permeability. Geotextiles, among various geosynthetics, exhibit these desirable properties (Lawrence, 2014). They find utility as filters in applications such as surrounding crushed stone with or without drains, between gabions and backfill soils, and in various other contexts where the controlled passage of liquids is essential while restricting the movement of soil particles (Koerner, 2016).

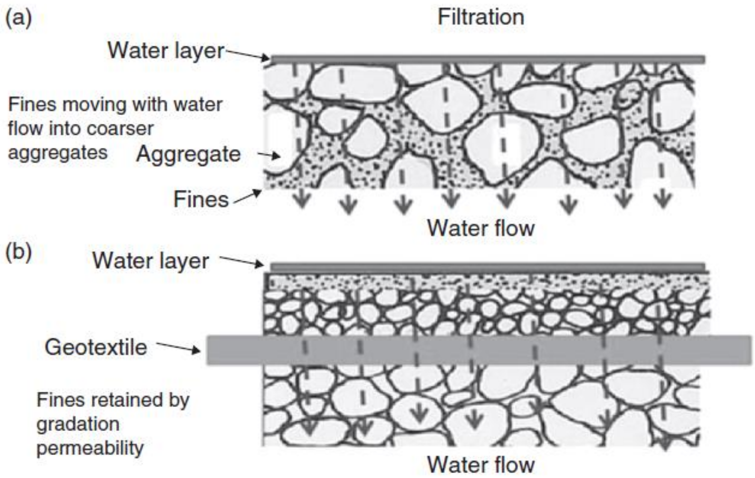

Figure 2.15. *Water flow and behavior of fine particles, a) Without geotextile, and b) With geotextile (Lawrence, 2014)*

2.2.4. Drainage

The function of drainage in geotechnical engineering is closely linked to that of filtration, wherein fluid pass into the geosynthetic occurs perpendicular to its plane. Geotextiles, geonets, and geocomposites are commonly employed for drainage purposes. Similar to the filtration function, effective drainage necessitates considerations for soil retention, adequate flow capacity, and the establishment of long-term equilibrium between soil and geotextile flow to minimize clogging of the pore spaces. These criteria ensure that drainage systems operate efficiently in diverse geotechnical applications, contributing to the sustained effectiveness of soil drainage and water management. Various application areas exist for these geosynthetics, including utilization in retaining walls, earth dams, and the stabilization of flowing rock slopes (Lawrence, 2014).

2.2.5. Waterproofing

In particular, geomembranes and geosynthetic clay liners are employed for waterproofing purposes, capitalizing on their exceptionally low permeability. They serve to prevent soil contamination and to protect various structures from water entrance. These materials find application areas to be dams and reservoirs for seepage control, as covers in solid waste landfills, and in various other contexts.

3. KEY FEATURES AND AFFECTING FACTORS OF GEOGRID

3.1. Pullout Resistance

The pull-out resistance of the geogrid comprises two elements: skin friction and bearing resistance, as depicted in Equation(3.*1*). Skin friction arises from the interaction between the geogrid surface and the soil due to friction phenomenon. On the other hand, bearing resistance pertains to the passive resistance caused by the soil. The soil in front of the transverse ribs faces the motion if the pull-out motion activate leading to the development of bearing resistance. The skin friction on longitudinal ribs and bearing resistance of transverse ribs are displayed in Figure 3.1.

$$P_R = P_{RS} + P_{RB} \tag{3.1}$$

P_R : Pullout resistance (kN/m)

P_{RS} : Skin friction (kN/m)

P_{RB} : Bearing resistance (kN/m)

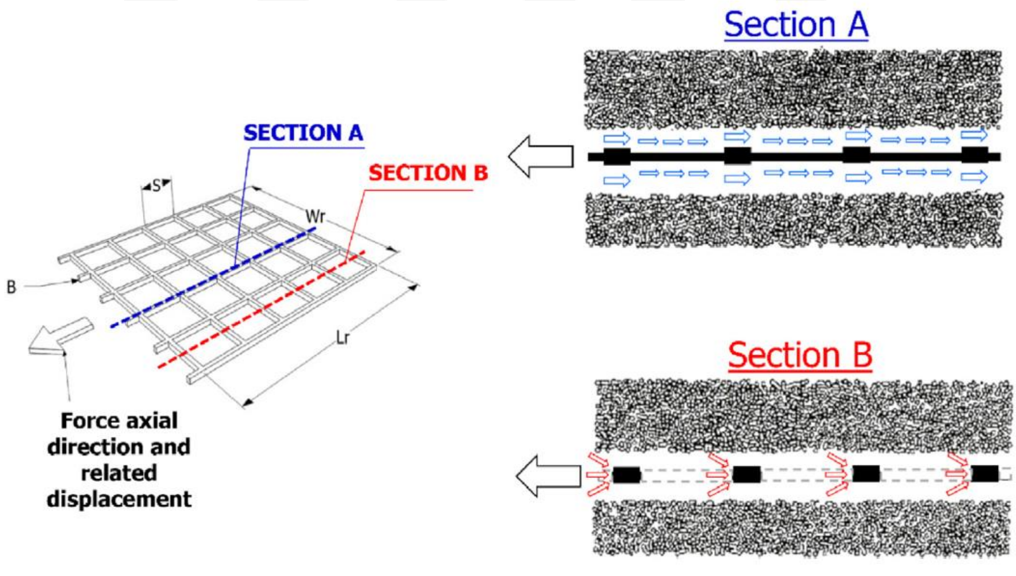

Figure 3.1. *Skin friction and bearing resistance (Cardile et al., 2017; Jewell, 1985)*

3.2. Interference Mechanism and Soil Dilatancy

Studies have been conducted on the use of geogrids in clayey soils, although geogrids are used with granular backfill material in practice. Under shear forces, the movement of granular particles over each other results in a transition from a dense structure to a looser one, which is creating additional volume. It is called dilatancy. Similar to soil-soil interaction, it is possible to discuss the dilatancy potential of granular soil in soil-geogrid interaction. Due to the pull-out movement, soil particles in front of the transverse rib exposed to shear forces move towards the upper part of the transverse rib and then pass over the transverse rib to fall behind. This behavior leads to void regions of the loosen soil at the back of the transverse rib, reducing the geogrid's pull-out resistance. This mechanism is referred to as interference. During pull-out, it is necessary to leave the required spacing between transverse ribs to prevent them from reaching the loose soil void zones. In an area of 36.00 mm^2, the movement of two particles was observed at different time intervals by Zhou et al. Figure 3.2 shows the movement of particles and created void. Cardile et al. developed a reduction factor to consider the interference mechanism in Equation (3.2a) and (3.2b).

$$C_{\alpha b} = a * \frac{S}{B_{eq}} \qquad if \ \frac{S}{B_{eq}} \leq 50 \tag{3.2a}$$

$$C_{\alpha b} = 1 \qquad if \ \frac{S}{B_{eq}} > 50 \tag{3.2b}$$

$C_{\alpha b}$: Interference reduction factor

a : The constant coefficient determined through linear regression is found to be 0.02.

S : Spacing between transverse ribs

B_{eq} : Thickness of the equivalent uniform strip rib

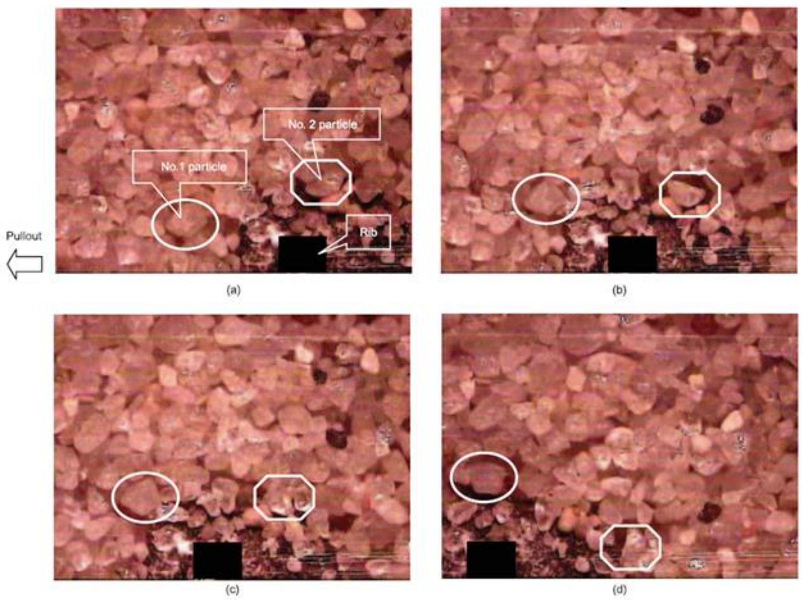

Figure 3.2. *The motion of particles at a) Initial, b) after 25 second, c) after 50 second, and d) after 75 second (Zhou et al., 2012)*

3.3. Interlocking Effect

The geogrid employed in coarse-grained soil restricts lateral expansion by providing support to the coarse particles within its apertures through confinement. This phenomenon is denoted as the interlocking effect. It allows the soil regions within the geogrid apertures, to mutually support one another and to minimize lateral movement (Figure 3.3) (Ziegler, 2017).

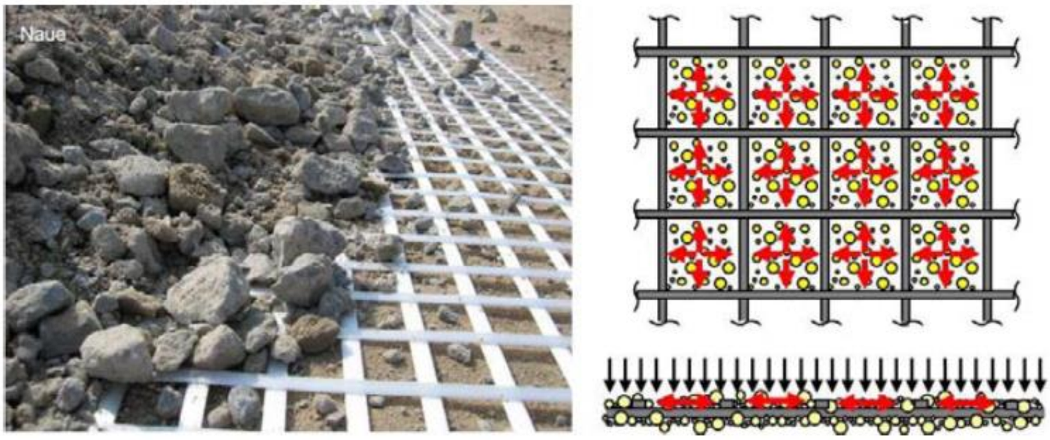

Figure 3.3. *Interlocking mechanism (Ziegler, 2017)*

3.4. Indirectly Active Geogrid

Indirectly active geogrid mechanisms are shown in Figure 3.4. Zone I corresponds to the pushout region, where soil displacement surpasses geogrid displacement. In Zone II, representing the pullout region, geogrid displacement exceeds soil displacement, activating the reinforcement element and providing passive resistance. Zone III is characterized as the interlocking region, where minimal displacement difference between soil and geogrid occurs, and the dominant effect is interlocking. In a typical structure, not all zones necessarily need to be active. The interlocking zone becomes prominent when the geogrid length is sufficient; if the reinforcement length is too short, it cannot effectively transfer the strength from the geogrid to the soil (Derksen et al., 2021).

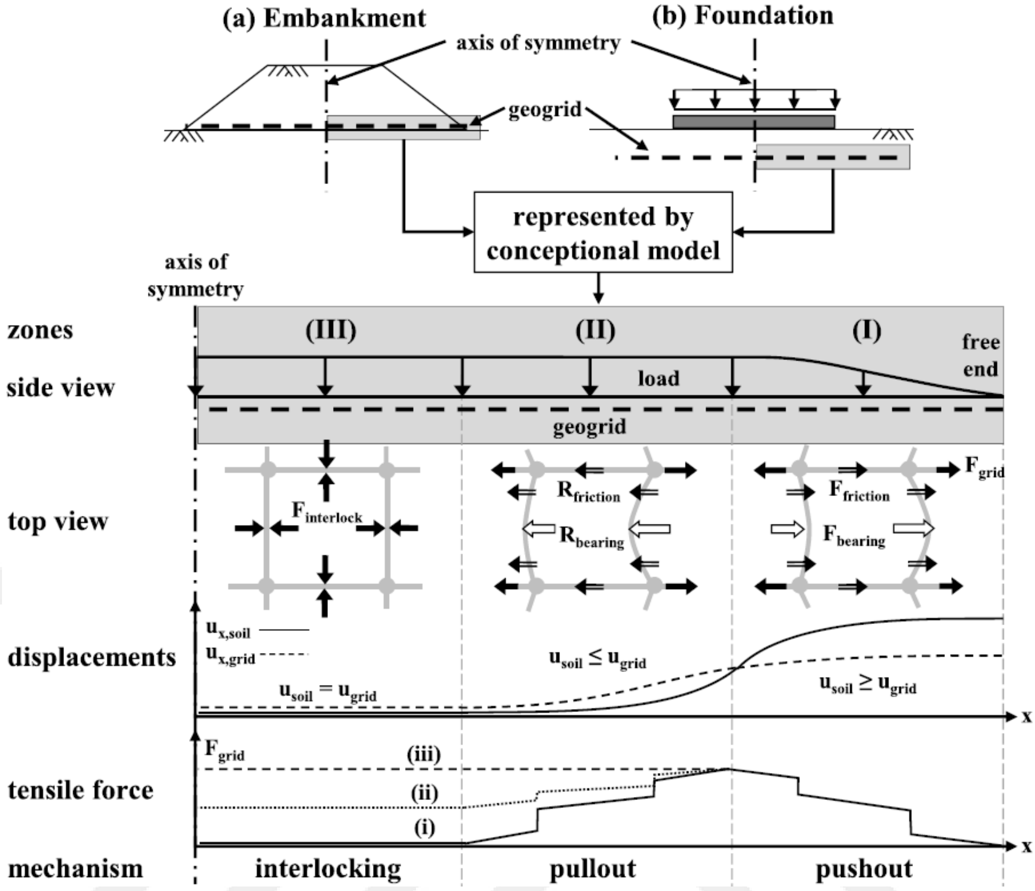

Figure 3.4. *Zones of indirectly activated geogrids (Derksen et al., 2021)*

4. LITERATURE

4.1. Pullout Experiment

The primary objective of the research carried out by Cardile et al. (2017) was to devise a former analytical approach aimed at determining the maximum pullout resistance when employing extruded geogrid with compacted granular soil. To compute the interference mechanism in the computations, a reduction factor ($C_{\alpha b}$) was developed. Four bidirectional PP geogrids and three unidirectional HDPE extruded geogrids were utilized in the pullout tests. The primary distinction in the geogrids arises from their varying transverse rib thicknesses, as passive resistance is generated by the elevations at the geogrid junctions and the transverse rib. The unit weights of the SP and SW class soils utilized were 16.24 and 18.36 kN/m^3, respectively. All pullout assessments were conducted under normal loads of 10.00 kPa, 25.00 kPa, and 50.00 kPa. The formula for the reduction factor relating the interference mechanism is presented in Equation (3.2a) and (3.2b). Upon comparing the theoretically calculated values utilizing the formula with the reduction factor to the experimental outcomes, deviations ranging from 1.00 to 38.00% were observed.

Since transverse ribs constitute a significant portion of the resistance against pullout behavior, the carrying capacity of these ribs is crucial. The interaction between geogrid and soil can be divided into two distinct categories: the microscopic behavior of the soil (size, shape, rotation, fractures, relative movement of soil particles) and boundary conditions (roughness of the sliding plane, stress level, deformation history). Zhou et al. (2012) investigated the micro-scale interaction mechanism between the transverse ribs of geogrid and sandy soil. In the pull-out experiment conducted within the 60.00 cm *40.00 cm *40.00 cm sized box (Figure 4.1). Facilitating the transmission of the load to the soil from a specified distance, a 15.00 cm long metal arm was inserted at the entrance of the box, aiming to reduce stresses on the front wall of box. For microscale examination of the interaction between geogrid and soil, a camera with high resolution (Particle Image Velocimetry ‘PIV’ system) was employed. The experiments utilized medium sand with a quartz content of 96% and a relative density of 66.00%. Results from the direct shear box tests revealed an internal friction angle of 27.30° for the soil. Geogrid reinforcement was produced with high-density polyethylene (HDPE) material. To minimize friction between the box and the soil in the experimental setup, silica oil was applied to the front face of the apparatus. Sand fell from a constant height of 60.00 cm and was placed into the box using the dry pluviation method. When the sand level reached a depth of 20.00 cm, a geogrid has a dimension of 30.00 cm * 36.00 cm was positioned along the machine's direction. The geogrid was pulled at a speed of 1.00 mm/min under four different normal stresses from 10 kPa to 50 kPa.

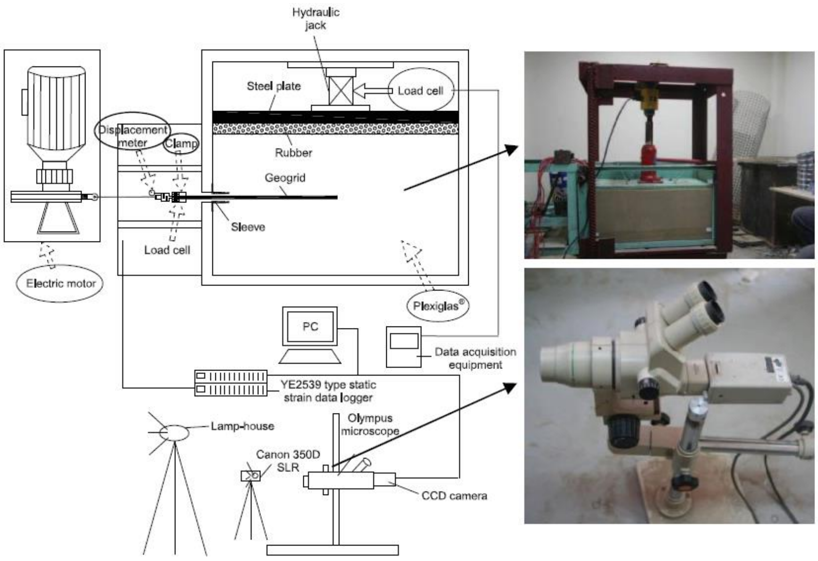

Figure 4.1. *The pull-out test setup to observe micro-scale (Zhou et al., 2012)*

After reaching the maximum point, a decrease in pullout resistance was observed in the experiment results. The cause of this decrease has been attributed to strain-softening trend observed at low cell pressures. Since the objective of this study is to investigate the interaction between sand particles and geogrid, the experiment was terminated when the displacement of the geogrid reached 2.00 cm. It was determined that as the normal stress increased, the apparent coefficient for friction decreased, and a primary reason was identified as dilatancy. The apparent coefficient of friction was 0.36 under 10.00 kPa normal stress, while it was 0.27 at 50.00 kPa normal stress level. The reason behind this was discussed as the ability of the round shaped quartz particles, due to easy rotation capacity on the surface between the soil and the geogrid. Therefore, low apparent friction coefficient and low pullout resistance were obtained. Additionally, low relative density reduces dilatancy variations, making the apparent friction coefficient uncertain relative to normal stresses. Particles located in front of the transverse ribs of the geogrid experienced compression, rotation, and movement towards both the upper and lower sides in response to pullout displacements. Also, particles fell into the voids created by the transverse ribs (Figure 3.2). The soil in front of the transverse ribs was in a passive state, while the soil behind them was in an active state. As the pullout displacement rose, shear zones formed within the sand. These zones, induced by the transverse ribs, were asymmetric relative to the soil-geogrid interface. The uplift failure mode was well-reflected by the experimental results and calculated values using the improved (Jewell, 1985) formula, which is based on scaling and shape factors related to the transverse rib. The wedge-like shear zones observed in front of the fiber resemble features that support the uplift failure mode.

In recent years, there has been a notable increase in the utilization of lightweight cellular concrete material, alongside traditional fill materials like sand and gravel. (Ye et al., 2022) investigated the impact of factors such as cement-to-fly ash ratio, aerated concrete age, normal stress, and cold joints on pullout resistance when uniaxial geogrid or steel strips were added into cellular concrete. Additionally, the study examined the outcomes of conducting pullout tests at two different time intervals (re-pullout) on the same sample. Uniaxial geogrids were fabricated from high-density polyethylene (HDPE) material subjected to the punched-drawn process. The embedded length of the geogrid in the aerated concrete was 140.00 cm, with a width of 30.00 cm and a thickness of 3.00 mm. The aperture was 1.50 cm wide and extended for 45 cm, with a maximum tensile stress of 114.00 kN/m. Steel strips, measuring 140.00 cm in effective length, 5.00 cm in width, and 4.00 mm in thickness, were employed. The yield strength of the steel strips was 450.00 MPa. The cellular concrete used in the study had dimensions of 140.00 cm in length, 42.00 cm in width, and 27.00 cm in height. Geogrids embedded within cellular concrete exhibited hardening behavior under high stresses and softening behavior under low stresses. Conversely, all steel strips demonstrated a softening behavior attributed to the arching effect. The addition of fly ash in cellular concrete had a favorable impact on pullout resistance. The pullout factor increased with the advancing age of aerated concrete, while it decreased with the escalating normal stress applied to the steel strip.

(Cazzuffi et al., 2014) investigated the influence of vertical stress and geogrid length on soil-reinforcement interaction. Displacement-controlled pullout tests were conducted using a 170.00 cm*68.00 cm*60.00 cm pullout box. Friction between the soil and the box's inner wall was minimized by employing teflon film. Steel cables were placed at six points for displacements and connected to the Rotary Variable Differential Transformer (RVDT). The uniformity coefficient, D_{50}, maximum dry unit weight, optimum water content, and shear strength angle values for the SP-type soil were 1.96, 0.32 mm, 16.24 kN/m^3, 13.50%, and 42°, respectively. HDPE uniaxial extruded geogrid was used, and tensile tests were performed for wide thicknesses according to EN ISO

10319, but with a displacement rate of 1.00 mm/min as used in the pullout test. The sample lengths used in the experiments were 40.00 cm, 90.00 cm, and 115.00 cm, while normal stresses were 10.00, 25.00, 50.00, and 100.00 kPa. The experiments were remained until geogrid rupture or displacement reached 10.00 cm. The pullout resistance of the samples was found to be strongly correlated with sample length and vertical stress. As vertical stress decreased, the wrapping effect on the geogrid diminished, resulting in a reduction in pullout resistance. Dilatancy behavior was observed in the soil. The elongation effect was prominently seen in longer geogrids subjected to high normal stresses. As the geogrid surface facilitating passive interaction enhanced, the peak pullout resistance ascended.

Different numbers of uniaxial geogrids containing transverse and longitudinal ribs were investigated in pullout tests using two different fill materials by Pant et al. (2019). The effect of the transverse rib aperture on the pullout behavior was also examined. Bottom ash and fly ash were used as fill materials, which were classified as SM and ML, respectively. A uniaxial geogrid coated with polyvinyl chloride on polyester (PET) was used as the reinforcement material. The tensile strength in the machine direction (along the longitudinal rib) of the geogrid was 80.00 kN/m, and the tensile strength in the direction perpendicular to the machine direction (along the transverse rib) was 30.00 kN/m. The longitudinal rib width was 5.75 mm, and the thickness of the reinforcement was 1.017 mm. The dimensions of the pullout box were 90.00 cm * 60.00 cm * 60.00 cm. The soil was compacted in two layers of 15.00 cm in the lower layer of the box. Experiments were conducted at a constant displacement rate of 1.00 mm/min according to ASTM-6706 with the help of 0, 4, 8, and 16 transverse ribs (Figure 4.2).

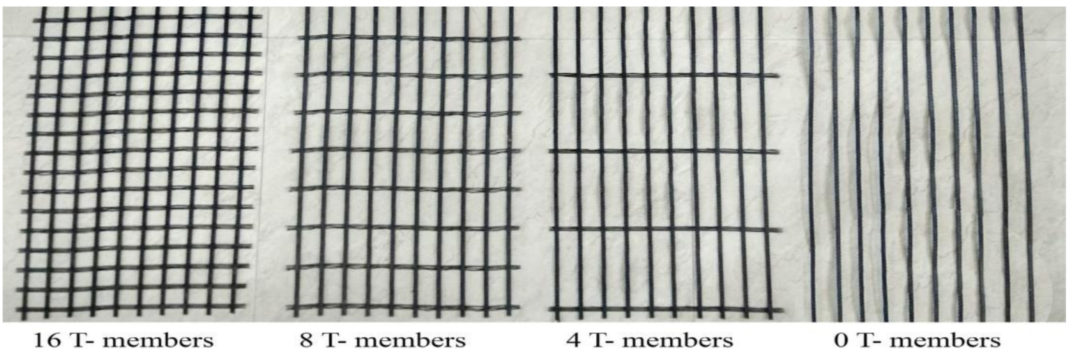

Figure 4.2. *The various numbers of transverse members (Pant et al., 2019)*

If the number of transverse ribs was enhanced, displacements in maximum pullout force also rose. This phenomenon was related to the expandability of the sample. Bearing resistance emerged after a 2.00 cm displacement, while pullout resistance contributed to sliding behaviour in the beginning. Sliding resistance constituted 70.00-75.00% of pullout resistance under a normal stress of 20.00 kPa (Figure 4.3). In samples with a large number of transverse ribs, the contribution of sliding resistance decreased to 55.00-60.00%. When the aperture was low, the geogrid behaves like a single plate. In case of the number of longitudinal ribs increases from 2 to 4 for a 27.00 mm aperture, the peak pullout force doubled. This indicated that the longitudinal ribs act independently of each other and their effective areas did not overlap at a 27.00 mm aperture. When fly ash was used as the fill material, after displacement in the range of 6.00-10.00 mm, transverse ribs developed bearing resistance. The pullout resistance obtained in fly ash corresponded to around 60.00% of the bottom ash. When the stiffness of PET geogrid was lower than HDPE and PP, the contribution of transverse ribs was more pronounced.

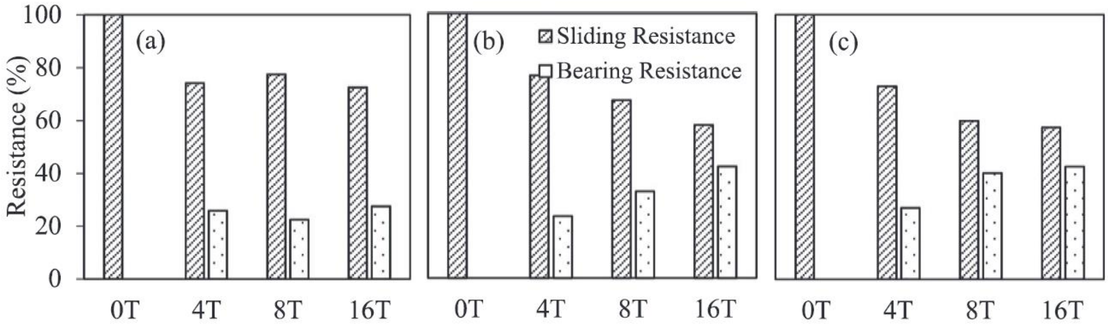

Figure 4.3. *The bearing and sliding resistance contribution of total pullout resistance at a) 20.00 kPa, b) 40.00 kPa and c) 80.00 kPa normal stress (Pant et al., 2019)*

Moraci et al. (2014) examined the soil-geogrid interface interaction through pullout behavior. Pullout tests with a displacement rate of 1 mm/min were conducted in a 1700 mm*680 mm*600 mm sized box in a displacement-controlled setup. The SP and SW soils used in the experiments had D_{50}, uniformity coefficient, maximum dry unit weight, water content, and peak shear strength angle values were 0.32 mm and 1.47 mm, 1.96 and 7.48, 16.24 kN/m^3, and 18.36 kN/m^3, 13.50% and 9.80%, 42.00° and 49.00°, respectively. Uniaxial extruded HDPE geogrids and biaxial extruded PP geogrids were used. Three different sample sizes, 0.40 m, 0.90 m, and 1.15 m, were used. Effective vertical stresses were 10.00, 25.00, 50.00, and 100.00 kPa. The experiments were finished when a 10.00 cm displacement was reached or failure occurred. The scaling effect in SW was depending on the D_{50} value and transverse rib thickness. Under a vertical stress of 25.00 kPa and a reinforcement effective length of 90 cm, SW yielded the highest pullout force for all reinforcements. It was determined that the integral of the interfacial tangent stress corresponded to the pullout force. Notably, a substantial increase in pullout resistance was observed when the soil particle size resembled the transverse rib thickness and was less than the geogrid aperture size. This increase was primarily attributed to the improved shear strength of the soil and the scaling effect. Geogrids within SW exhibited greater displacements. The pullout resistance hinged on the mechanical properties of the soil, the stiffness, and the geometry of the geosynthetic. As the shear strength of the soil and the geogrid's bearing area (A_b) increased, pullout resistance ascended, while the B/D_{50} ratio diminished.

The ability of bearing resistance through transverse ribs in the geogrid is also achievable in steel strips with the utilization of supplementary materials. Suksiripattanapong et al. (2020) investigated the efficiency of bearing reinforcement applied to steel strips on soils characterized by varying moisture content and particle size within GW and SP type of soils (Figure 4.4). Consequently, experiments were conducted for each soil type at two different moisture content levels for below and above the optimum moisture content. The experimental setup involved a pullout test apparatus with dimensions of 270.00 cm * 60.00 cm * 40.00 cm. The experiments incorporated one and two transverse elements. Maximum pullout forces were attained at displacement levels ranging from 3.00 to 7.00 mm. The ultimate pullout resistances were observed when the moisture content fell below the optimum level. This phenomenon was attributed to the higher sliding resistance angle exhibited by the soil under 80.00% conditions. In situations involving a solitary transverse element, an increase in moisture content approached punching shear failure. Contrarywise, when the number of transverse elements exceeded one, interference behavior revealed. Moreover, the moisture content and soil gradation exhibited no noticeable impact on interference behavior. The locking effect occurred when the B/D_{50} ratio dropped below 12.00, and the normal stress was less than 120.00 kPa. The deployment of a transverse element exceeded the predicted increase in pullout resistance, owing to the inclined pull effect induced by high stiffness and shear resistance.

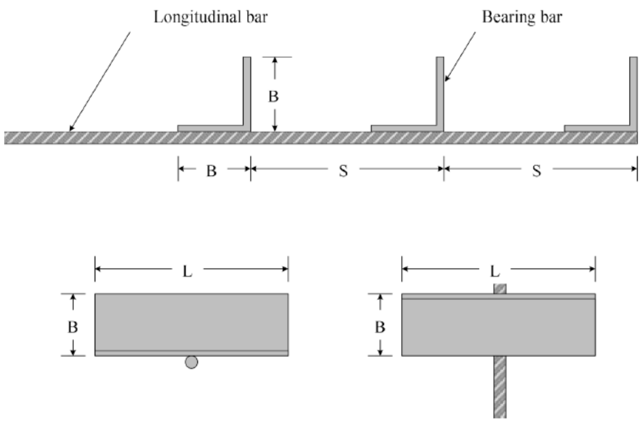

Figure 4.4. *Bearing reinforcement on the steel strip surface (Suksiripattanapong et al., 2020)*

Lajevardi et al. (2014) investigated the physical mechanisms and capacities of geosynthetic anchor systems, specifically focusing on the simple run-out and wrap-around configurations. The pullout test apparatus adhered to ASTM Standard D6706-01 (2007) and EN 00189016 (1998) standards, featuring dimensions of 1.10 m in width, 1.10 m in depth, and 2.00 m in length (Figure 4.5). Coarse gravel and fine sand were selected as the materials for coarse-grained and fine-grained components, respectively. The reinforcement materials comprised two distinct geotextiles, one biaxial and one uniaxial, along with a biaxial polyester geogrid established for its high tensile strength and low creep characteristics. To mitigate the impact of the front wall, a guide box with a 0.50 m width embedded within the soil was utilized. The initial 0.18 m thick soil layer was systematically compacted and placed using a tamper, followed by the placement of the geosynthetic element on the leveled surface. In the case of the simple run-out anchor system, soil layers ranging from 0.40 to 0.50 m were sequentially compacted and layered a top of the geosynthetic. Specifically, the 0.40 m scenario involved two layers of 0.20 m each, whereas the 0.50 m condition incorporated three layers of 0.20 m, 0.10 m, and 0.20 m, respectively. The experiments, performed at a controlled rate of 1 mm/min, were concluded upon reaching the maximum pullout force.

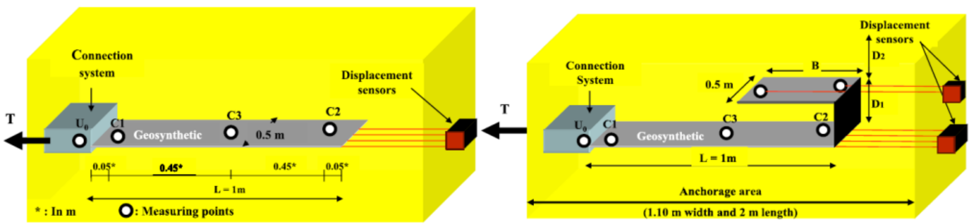

(a) Simple run-out (b) Wrap around

Figure 4.5. *Pull-out test setup with a) Simple run-out and b) Wrap around anchor system (Lajevardi et al., 2014)*

The featured displacement at the front side of geogrid leads the formation of the initial curve in the initial phase of the pullout in the case of mobilization transpired according to Lajevardi et al. (2014). Observed displacements increased subsequent to the completion of mobilization as a giving rise to a secondary slope in the curve. Full-scale mobilization of friction along the entire length of the geogrid indicated its behavior as a stiff reinforcement. Especially, in experiments conducted with sand, the displacement threshold of the geogrid was observed to be lower compared to those involving geotextile, highlighting the pivotal role of geosynthetic shape. The mobilization characteristics of geosynthetic plates exhibited remarkable similarity across both soil types and anchor systems. Within the wrap-around anchor system, the displacement curve against pullout force showcased three obvious slopes (Figure 4.6). In contrast, the simple anchor system exhibited two or three slopes, contingent upon stiffness and material characteristics. As the head displacement approached the predetermined limit, movement in the rear section ensued. This movement was depending on factors such as stiffness, geosynthetic shape, confinement stress, and soil type. Elevating confinement pressure correlated with an increase in the maximum pull force, with the wrap-around anchor system demonstrating superior resistance compared to the simple anchor. For modest displacements, the influence of both anchor systems was similar.

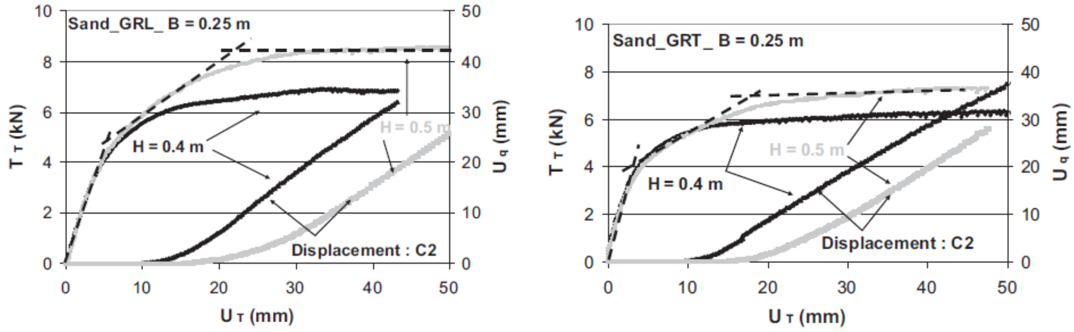

Figure 4.6. *The head displacement (U_T) and rear displacement (U_q) versus head tensile force (T_T) under two different confinement stresses (Lajevardi et al., 2014)*

In the study conducted by Esfandiari and Selamat (2012), the objective was to prevent the stripping of reinforcement from the soil by adding an element at a 90° angle to the surface of a steel strip. The study utilized SW type of soil as the filling material, featuring a maximum dry unit weight of 17.14 kN/m^3 and an optimum water content of 12.23%. Friction angles at 60.00% and 90.00% relative density were 39° and 45°, respectively. A total of 21 distinct steel strips, including those with anchoring elements, were employed, as illustrated in Figure 4.7. The pullout box, measuring 130.00 cm in length, 100.00 cm in width, and 50.00 cm in depth, was used. The anchoring elements were positioned facing downward at the midpoint of the box, maintaining a 17.00 cm gap between the box's bottom surface and the sample incorporating an 8.00 cm long anchoring element. This arrangement aimed to mitigate interference effects that could arise on the friction surface between the box and the soil. Normal stresses of 50.00, 60.00, 65.00, 75.00, and 100.00 kPa were applied, with a pullout rate of 1.00 mm/min. Compression was applied every 10.00 cm, achieved by dropping a 44.5 N hammer from a height of 45.7 cm, with 25 blows per layer. The soil had a water content of 2.50%, and its relative density was 60.00%. While an increase in the number and depth of anchoring elements enhanced pullout resistance, the impact of anchoring depth was more significant concerning pullout resistance angle. For each anchoring depth, an optimal distance was determined. The study concluded that the effective length of the reinforcement could be reduced, allowing for the shortening of the reinforcement length due to the presence of the anchoring element. This investigation offered a solution for mechanically stabilized earth, particularly in situations involving confined or limited construction areas.

Figure 4.7. *Steel strips with anchoring elements (Esfandiari & Selamat, 2012)*

Biabani et al. (2016) focused on the investigating the passive resistance exerted by geocell-reinforced soil, utilizing a setup where normal stress was applied parallel to the pullout direction, aligning with the shear plane. The study examined the slippage behavior of the geocell, employing crushed basalt as the soil material with a dry unit weight of 19.00 kN/m^3 and an average particle diameter of 3.30 mm. To explore the impact of open area ratio on passive resistance, four variations of geogrids and two types of geomembranes were transformed into geocell forms (Figure 4.8). Geogrids were merged and adapted to form cells, which of them classified as triaxial or biaxial and produced from high-density polypropylene.

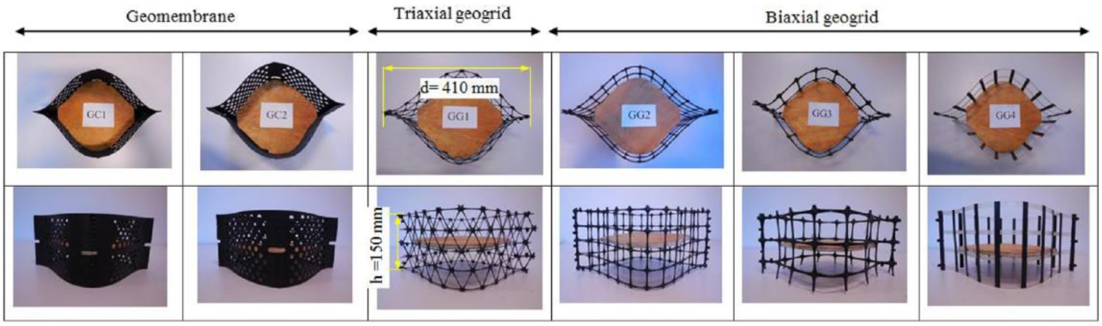

Figure 4.8. *The geocell samples (Biabani et al., 2016)*

The experimentation utilized a broad pullout apparatus measuring 80.00 cm in length, 60.00 cm in width, and 50.00 cm in height (Figure 4.9). A total of 36 experiments were conducted at different normal pressures, with the soil's relative density being 77.00% as layers were compacted using a vibrating hammer by Biabani et al. (2016). Vertical displacements were measured through LVDTs, and strain gauges were strategically positioned at various heights on a 150 mm high geocell cell. The overlay pressure ranged from 1.00 kPa to 45.00 kPa, with a constant overlay pressure maintained throughout the experiments. Maximum pullout forces were attained within a vertical displacement range of 4.00 to 8.00 mm. An observable trend revealed an increase in pullout forces with a rise in normal pressure. The subsequent reduction in pullout force post-peak was associated with aggregate dilation. Volume expansion occurred at lower normal pressures, while volume reduction was observed beyond 20.00 kPa normal pressures. The optimal interlocking effect in the triaxial sample was achieved due to the triangular cell opening and optimum cell size. The measured normal stress on the geocell cell surpassed the theoretical calculation using the finite element method. As overlay pressure increased, both slippage and passive resistance exhibited an upward trend. The stiffness of the geocell positively correlated with increased pullout strength, while the stiffness of the geosynthetic exhibited negligible impact on behavior. A coefficient of friction resulted in an increase in passive resistance. The critical factors influencing passive resistance on the geocell included the geocell's open area and lateral pressure inducing slippage. The load mechanism was major in geocell behavior, with geocell yielding under high passive resistance values. During pullout, significant passive resistance was observed in the transverse fibers of the geogrid, with higher values recorded in geogrid samples compared to those with geomembrane. Passive resistance emerged as a crucial factor in interfacial shear strength, with a reciprocal relationship observed as stiffness decreased and passive resistance increased.

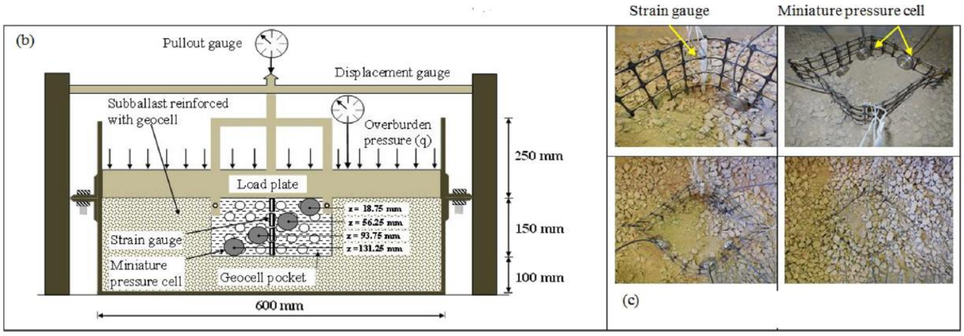

Figure 4.9. *Vertical pullout test setup and measurement equipment (Biabani et al., 2016)*

Another study aimed at increasing pullout resistance on a soft steel strip by adding transverse elements was conducted by Han et al. (2021). Steel strips with drilled holes were connected using pin elements to create transverse elements. Experiments were conducted using a pullout apparatus with displacement control. SW class soil was used as the filling material, with a maximum dry unit weight of 18.82 kN/m^3 and an optimum water content of 14.10%. The cohesion value was 8.70 kPa, and the internal friction angle was 35.60°. Cases without transverse elements and with one, two, and three transverse elements were examined under normal stresses of 25.00, 50.00, 100.00, 150.00, and 200.00 kPa. The sample without transverse fibers reached the maximum pullout force value at a displacement of 1.20 mm. In reinforced samples, a sudden increase in pullout force was observed when a displacement value of 4.00 mm was achieved. The effect of using more than two transverse fibers was not observed when the normal stress was below 100.00 kPa. Transverse elements came into play when displacements reached 4.00 mm and normal stress exceeded 100.00 kPa. The highest pullout force was attained when two transverse elements were used, and transverse elements were placed in positions 1 and 3. This indicates that the interference effect depends on the distance between transverse elements. As normal stress increased, pullout resistance also rose, with a greater growth observed in samples with transverse elements. Bearing strength increased with an uplift in the number of transverse elements. In cases of low normal stress, a general shear failure was approached at a displacement of 50.00 mm. In cases of high normal stress, punching shear failure was approached. The contribution of transverse elements to pullout resistance varies between 33.00% and 66.00% depending on the number of transverse elements. The bearing bond coefficient, which has a reduction factor, could increase with a rise in the number of transverse fibers thanks to the interference effect. Normally, as the number of transverse fibers increases, bearing resistance stress will also climb, causing the bearing bond coefficient to fall. When normal stresses are high, bearing resistance is greater, and the effect of the number of transverse elements on the bearing bond coefficient is low. The rate of increase in the bearing bond coefficient under low stresses decreased. Therefore, when estimating the number of transverse fiber elements, bearing resistance stress and the bearing bond coefficient should be considered. The use of transverse elements allowed a reduction in the number of reinforcements used in mechanically stabilized retaining structures. The effective length of the reinforcement did not affect bearing resistance. The total pullout resistance was composed of the friction of the longitudinal element and the bearing resistance of the transverse element. The quality of the transverse element and a slight increase were observed as normal stress and the number of transverse elements went up in the bearing strength dependent on the transverse element. The interference effect also increases with an increase in normal stress and the number of transverse elements.

The interaction model and experimental apparatus for indirectly active geogrids were investigated within the scope of this study by Derksen et al. (2021). Micro-mechanical interaction between soil and geogrid could not be observed since the geogrid was surrounded by soil. Therefore, a new experiment setup was developed aimed to investigate interfacial interactions between surfaces without disturbing the soil, examine displacements and tension force distribution, minimize scaling effects, and study the indirect activation of soil surrounded by geogrid (Figure 4.10). Two-axis pressure experiments were conducted on transparent soil reinforced with geogrid to investigate the geogrid-soil interface interaction. Biaxial PET geogrids were used in the experiments. The tensile tests of the geogrid were conducted in oil-saturated transparent soil. While there was no significant difference between the tensile tests conducted in air and oil-saturated soil up to 2.00% strain, differentiation occurred when the strain exceeded 2.00%. Transparent soil was created using translucent solid materials, usually consisting of quartz glass. The soil class was GP, and the relative density of the soil used in the experiment was 57.00%. Shear box tests were conducted at five different stresses up to 400.00 kPa normal stress, using viscous oil along with the soil. As the added viscous oil increased, the shear strength decreased. The shear strength for the unsaturated soil, partially saturated soil, and fully saturated soil were 49.90°, 47.60°, and 46.50°, respectively. After conducting three axial tests on partially saturated and fully saturated soils, only a 1.00° difference in soil strength angles was observed. Scaling effects were not expected to occur in this study. The front and bottom walls of the test setup were made of acrylic glass. Compression was applied at 20.00 mm intervals. To avoid light reflections in the transparent soil, the experiments were conducted in a dark room. The test setup had its lighting system. Initially, a vertical and horizontal pressure of 2.00 kPa was created. Subsequently, the sample was loaded vertically at a rate of 1.00 mm/min, while maintaining a constant pressure of 2.00 kPa. Soil deformations were determined using a camera and laser, while geogrid movements were detected based on points marked on the geogrid using the LED at the bottom. The Digital Image Correlation (DIC) method was used for shape analysis. Settlements occurred in the vertical stress range of 12.97-62.31 kPa. Under a vertical stress of 62.31 kPa, higher displacement was observed in the upper part compared to the lower part. As a result of indirect geogrid activation, lateral soil movement was observed on the right side of the specimen. Soil sliding over the specimen was observed. Deformation and deflection behavior were observed in the transverse fiber of the geogrid, and no interference effect was observed. If the fill soil was not stiff and tended to settle, the reinforcement would be active vertically, and membrane forces would occur. Three interaction mechanisms, namely pushout, pullout, and interlocking, were defined. The geogrid reached maximum tensile force on the critical shear plane. In the soil shear zone, the soil load was transferred to the geogrid. Subsequently, the geogrid load was transferred to the remaining soil. The transverse fiber displacement created deflection in the pushout and pullout areas. In the pushout area, the transverse fibers moved relative to the soil, while in the pullout area, they moved in the opposite direction to the tensile force. The pushout, pullout, and interlocking zones covered 15.00%, 49.00%, and 36.00% of the total geogrid area, respectively. In the transition zone between pushout and pullout, interfacial stresses reached a peak.

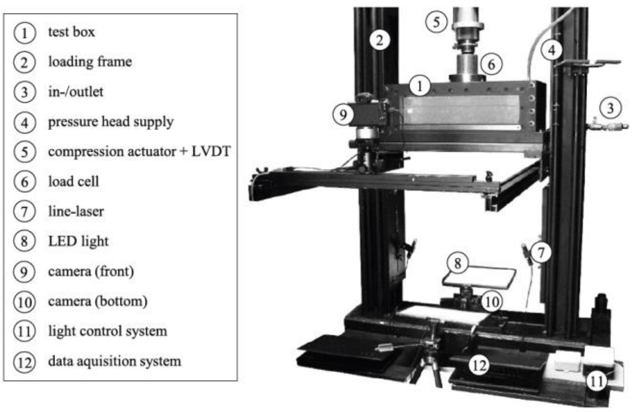

Figure 4.10. *The new experimental setup to observe micro-mechanical interaction between soil and geogrid (Derksen et al., 2021)*

Abdi et al. (2022) introduced the Pegged-Geogrid (PG) which consisted of geogrid added peg to enhance soil-geogrid interaction. After the soil compression stage was completed, the peg could be placed without the need for any additional processing. The use of metal pegs resulted in additional passive resistance, thereby increasing pullout resistance. This allowed for cost and time savings by reducing the amount of geogrid required and the necessary backfill. The influence of the PG system was investigated by using a pullout test setup with dimensions of 100.00*55.00*60.00 cm. SP, SP, and GP type of soils and biaxial geogrid were used in the experimental process. Different types of metal having an 8.00 cm limited height are shown in Figure 4.11. The 90 experiments were performed at 85.00% relative density under normal pressures of 25.00, 50.00, and 100.00 kPa. The upward trend in the soil particle size and vertical stress raised the pull-out force. During the pullout test, a larger displacement was required to activate passive resistance according to skin friction. The displacement values of various nodes can be seen in Figure 4.12. The first 50.00 cm of geogrid was not embedded, and the pegs were located at the end of the geogrid. While the minimum displacement is observed at the end point of the geogrid, the highest displacement is observed at the location of the clamp. The impact of pegs was revealed after a 2.00 cm displacement. When non-pegged samples exhibited strain hardening and softening behavior, the pegged geogrid showed complete hardening behavior in SP-type soils. Thus, the pegs climbed the bearing resistance as well as the pullout resistance. The growth on the peg width enhanced the soil volume that passively resisted the pullout behavior. Better pull-out resistance and displacements matching maximum pull-out forces were obtained by increasing the number of pegs. Maximum pull-out resistances occurred at larger displacements when normal pressure and soil particle size increased in PG samples. Increasing peg width also had this effect. When it comes to increasing pull-out forces, SP particles exhibit less of an enhancement effect from peg width than GP coarser grains. A peg rotated in the experiment caused the reduction of pullout resistance.

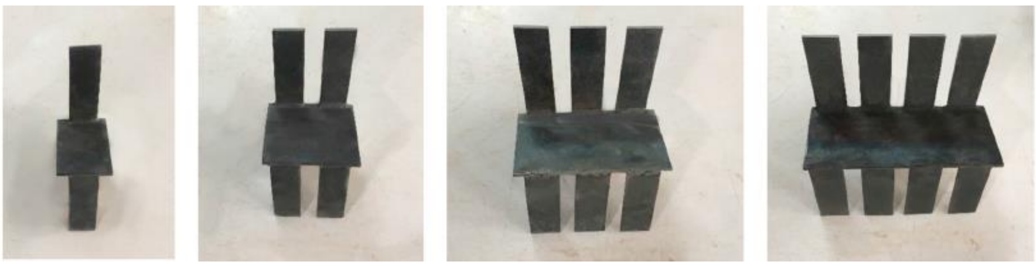

Figure 4.11. *View of different types of metal pegs (Abdi et al., 2022)*

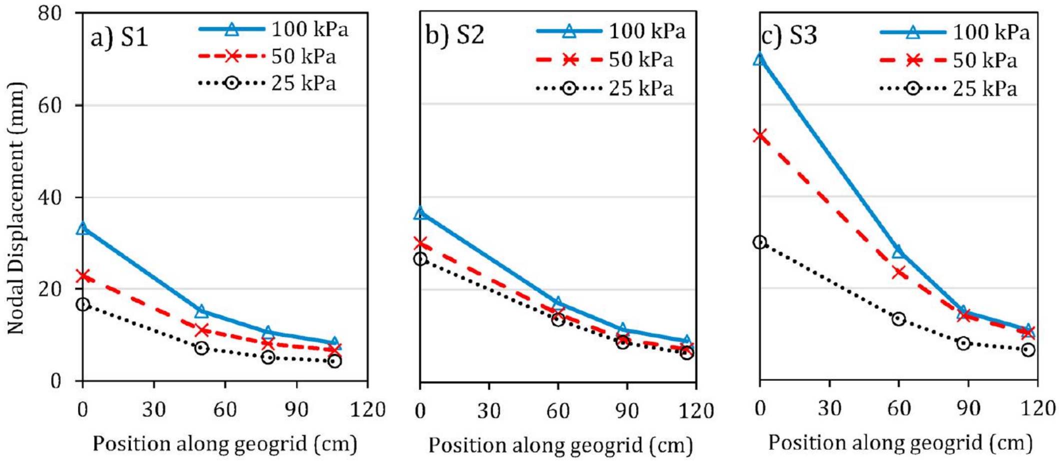

Figure 4.12. *Nodal displacement according to the position of nodes a) SP soil, b)SP soil and c) GP soil (Abdi et al., 2022)*

Abdi and Mirzaeifar (2017)investigated the interaction between soil and geogrid in soils with varying particle sizes and distributions. The pullout test setup included a transparent side on the box to visualize soil deformation. The pullout force was applied by a computer-controlled air-pressure jack, while vertical normal pressure was maintained using an air bag. Particle displacement was measured through Particle Image Velocimetry (PIV), enabling non-invasive measurement of the specimen. The camera captured particle movements. Test specimens included poorly graded sand (SP), well-graded sand (SW), and well-graded gravel (GW) classified according to the Unified Soil Classification System. High-density polyethylene unidirectional geogrid was employed. To reduce friction, the inner surface of the box in the test setup was oiled and coated with polyethylene. Soil was placed in three layers, and the geogrid's longitudinal fiber was aligned parallel to the machine. Linear Variable Differential Transformers (LVDTs) connected to selected points measured displacements. An air bag on the reinforced soil's surface was covered by the top. The finite element method in the ABAQUS program was utilized for the analysis of the conducted experiment. Numerical analysis was specifically conducted for the well-graded gravel soil sample. The test setup was accurately modeled in the program, with established boundary conditions and mesh networks. The pullout force was stabilized after reaching the maximum point under normal pressures of 25.00 and 50.00 kPa. Under a normal force of 150.00 kPa, a subsequent decrease in the maximum pullout force occurred and stabilized. An observable jump in the pullout force during the initial loading stages was attributed to an increase in normal pressure. The correlation between an increase in average particle size and an enhanced pullout force was evident. Particle size, normal pressure, and gradation distribution contributed to an increased interlocking effect. Initially, heightened interaction between particles due to an expanding shear zone resulted in increased resistance. The interaction between well-graded gravel and geogrid proved effective, spreading the shear zone over a considerable thickness. Geogrid displacement led soil particles towards the front side of the geogrid, creating passive resistance. In the context of pullout scenarios, the primary contribution of the soil was passive resistance. It was concluded that particle size stood out as the primary parameter influencing the thickness of the shear zone.

The soil-reinforcement interaction within clayey soil by incorporating high-strength, finely layered granular soil has been investigated interaction in the study conducted by Abdi and Zandieh (2014). Pullout tests were conducted through a pullout test apparatus, with geogrid selected as the soil reinforcement. To achieve a flexible facing on the front side of the pullout test setup box, geofoam was employed. The pullout force was applied by an air-pressure-operated jack, while normal pressure was maintained using an air bag. Experimental specimens were generated by placing geogrid with a thin layer of sandy soil in clayey soil. Numerical analysis was conducted using the PLAXIS program, where uniformly distributed load represented normal pressure, and the pullout force was defined as a point load. Different values for the interaction coefficient "R" were tested until alignment with experimental results was achieved. The pullout test setup was modeled in the PLAXIS program with varying widths while keeping all other parameters constant. Fig. revealed that, in specimens created by surrounding geogrid in clay soil with a thin layer of sandy soil, the thinness of the sandy soil layer had no discernible effect. However, as the thickness of the sandy soil layer increased, a noticeable effect emerged, augmenting the pullout force. The sandy soil layer reached an optimum at a specific point. Tensile pullout forces for specimens with geogrid in sandy soil and specimens with an optimum thickness of a thin sandy soil layer within clay soil, both subjected to the same normal pressure force, exhibited near equivalence. Experimental results demonstrated an increase in soil-geogrid interaction and tensile pullout resistance with increasing normal pressure. A consistent correlation was observed when comparing numerical analysis results with experimental outcomes, indicating that changes in tensile pullout force due to normal force were in harmony. A substantial surge in pullout force occurred as normal stress increased from 25.00 kPa to 50.00 kPa, attributed to the interlocking effect. The alteration in tensile pullout force due to the thickness of the sandy soil layer in the geogrid specimen, surrounded by a thin layer of sandy soil in clay soil, was nearly identical in numerical analysis and experimental findings. The utilization of geogrid surrounded by a thin layer of sandy soil within clay soil was found to enhance soil-geogrid interaction. This improvement heightened the interaction between soil and geogrid surfaces, consequently amplifying pullout resistance. Strengthening interaction between soil particles and geogrid occurred with increased normal pressure. The optimum thickness for the sandy soil layer, in which geogrid was placed in clay soil, was determined to be 8.00 cm, suggesting that the optimum thickness could be computed for individual projects. The congruence between numerical analysis and experimental results was evident.

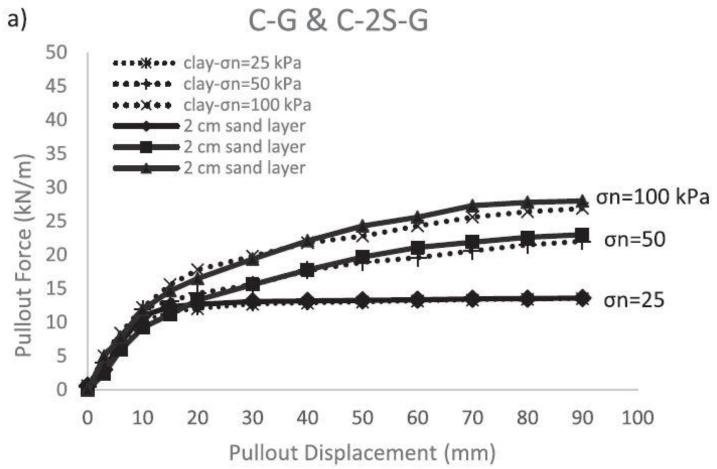

Figure 4.13. *Pullout resistance versus displacement graph for 2.00 cm thin sand layer (Abdi & Zandieh, 2014)*

Tos et al. (2023) studied the sanded geogrid with different granular soil to increase pullout resistance of geogrid. Coarse, medium and fine-grained granular materials were coated via resin. The best adhesion between the geogrid and coating ma material was attained from the soil maximum grain size 4.75 mm. SP and SW types of soil were backfill material in pullout tests, while two types of biaxial geogrid, PET and HDPE, was utilized. Styrofoam with grease oil was used to reduce front wall interaction. Backfill soil was uniformly placed into the metal box employing the dry pluviation method from a standard height of 1.00 meter, assisted by a sand spreader. To evaluate coating impact, the tensile strength tests was performed. The pullout strength increased twice thanks to improvement of geogrid. Hence, the sudden slippage was eliminated. The tensile strength of some geogrids reduced since the resin using coating process made samples more rigid. The sanding method realized savings on time, effort, substances, and expense.

In the research that forms the basis of this thesis, fences have been added to the surfaces of the transverse ribs to enhance the bearing resistance of the geogrid, as seen in Figure 4.14 (Gültekin and Evirgen, 2021). The lengths and angles of fences were chosen as variable parameters, which were added to biaxial extruded geogrid surfaces. The angle between the geogrid surface and the fences differed as 30°, 60°, and 90°, while the length values of fences varied as 1.00 mm, 2.00 mm, and 3.00 mm. Geogrids with fences were produced with a 3D printer by using glycol-modified polyethylene terephthalate (PET-G) filament. Dimensions of the pullout test box were 22.00*22.00*7.00 cm since the produced geogrid size was limited due to the 3D printer. Experiments were conducted in SP-type soil with a relative density of 80.00%. Moreover, tensile strength tests were performed to investigate the effect of the fence.

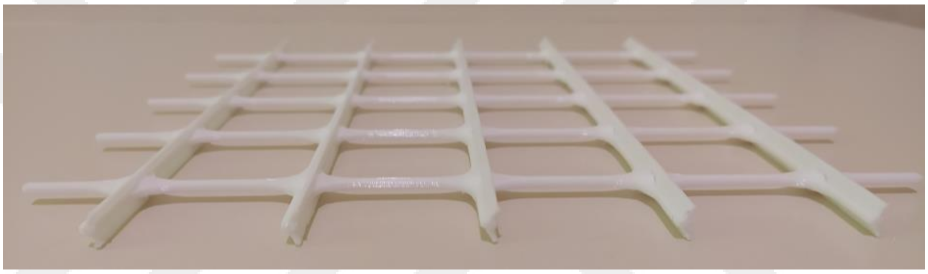

Figure 4.14. *Fences on the geogrid surface (Gültekin & Evirgen, 2021)*

The introduction of geogrid fences along the third dimension contributes to an increase in the tensile strength of the geogrid, when the angle of the geogrid fences approaches 90° and their length increases. When subjected to normal loads of 25.00 kPa, 50.00 kPa, and 75.00 kPa, the 90°-3 mm sample demonstrated a pull-out force resistance of 651.63%, 210.08%, and 256.96%, respectively, in comparison to the original geogrid. The resistance against stripping follows a similar pattern, increasing as the fence angle approaches 90° and its length increases due to the results observed in tensile strength tests. Notably, all specimens exhibited a higher pull-out force than the original geogrid, indicating that the addition of fences has an enhancing effect on the pull-out capacity.

The geomembranes employed in this thesis to boost bearing resistance were positioned 90° from the geogrid surface as a result of this investigation.

Table 4.1 provides a summary of the literature review about pullout tests. The abbreviation "Reinf. Type" in the table stands for "Reinforcement Type". Additionally, geogrid, geotextile, and geomembrane are abbreviated as geog., geot., and geom., respectively.

Table 4.1. *Studies in the literature related to pullout tests*

Author	Objective	Box Sizes (cm)	Normal Stress (kPa)	Soil Properties					Reinf. Type
				Type	D_r (%)	γ_{dmax} (kN/m^3)	ϕ (°)	D_{50} (mm)	
Cardile et al. (2017)	Consider the interference mechanism in pull-out resistance	-	10 25 50	SW SP	95	16.24 18.36	-	0.32 1.47	Geog.
Zhou et al. (2012)	Soil-transverse rib interaction in micro-scale	60 40 40	10 20 30 50	Sand	66	17.07	27	0.34	Geog.
Ye et al. (2022)	Factor affecting pull-out resistance of geogrid and steel strip in lightweight cellular concrete	150 45 60	10 30 60	-	-	-	-	-	Geog. Steel strip
Cazzuffi et al. (2014)	Influence of vertical stress and geogrid length on soil-reinforcement interaction	170 68 60	10 25 50 100	SP	95	16.24	42	0.32	Geog.
Pant el al. (2019)	Impact of transverse and longitudinal ribs on pullout resistance	90 60 60	20 40 80	SM ML	-	9.60 13.70	42 31	0.15 0.035	Geog.
Moraci et al. (2014)	Soil type influence on pullout behavior	170 68 60	10 25 50 100	SP SW	95	16.24 18.36	42 49	0.32 1.47	Geog.

Table 4.1. (Continued) *Studies in the literature related to pullout tests*

Suksiripattanaponga et al. (2020)	Efficiency of bearing member on steel strip	270 60 40	30 50 90	GW SP	90	20.00 16.70	45 40	5.70 0.31	Steel Strip
Lajevardi et al. (2014)	Simple run-out and wrap-around anchor systems	200 110 110	-	Coarse soil Fine sand	-	20.50 15.99	37 35	- -	Geog. Geotx.
Esfandiari et al. (2012)	Prevent the stripping of steel strip by adding an element	130 100 50	50 60 65 75 100	SW	60	17.14	39	1.40	Steel strip
Biabani et al. (2016)	Geocell pullout resistance	80 60 50	1-45	Crushed basalt	77	19.00	-	3.30	Geog. Geom.
Han et al. (2021)	Influence of transverse members added to steel strip	160 76 55	25 50 100 150 200	SW	-	18.82	36	-	Steel strip
Derksen et al. (2021)	Soil-geogrid interaction for indirect activated geogrid	50 22 13.5	12.97 23.42 38.67 62.31	GP	57	21.58	50	7.20	Geog.
Abdi et al. (2022)	The impact of metal pegs addition to geogrid	100 55 60	25 50 100	SP SP GP	85	15.70 15.00 17.08	35 39 42	1.07 3.08 6.39	Geog.
Abdi et al. (2017)	The impact of particle size gradation on soil-reinforcement interaction	100 60 60	25 50 100	SP SW GW	70	16.38 17.66 16.87	33 40 44	0.22 1.50 8.00	Geog.

Table 4.1. (Continued) *Studies in the literature related to pullout tests*

Abdi et al. (2014)	Soil-geogrid interaction of geogrid embedded small layer sandy soil in clayey soil	100 60 60	25 50 100	CL SW	-	15.70 17.00	21 38	-	Geog.
Tos et al. (2023)	Effect of geogrid coating with granular soil on tensile and pullout strength	52 52 22.5	22.9 45.6 68.7	SP SW	80	14.90 17.90	-	-	Geog.
Gültekin and Evirgen (2021)	The tensile strength and pullout resistance effect of added fences to geogrid surface	22 22 7	25 50 75	SP	80	14.35	47	0.60	Geog.

4.2. Direct Shear Experiment

Similar to pullout tests, the main purpose of the large-scale direct shear test is the determination of pullout resistance.

The interaction dynamics of reinforced soil-geogrid systems through pullout experiments were conducted by Mirzaalimohammadi et al. (2019). Two novel reinforcement approaches were implemented to enhance the passive resistance of the geogrid. In the first system, steel bars were affixed to the transverse fibers of a uniaxial geogrid. These bars were securely fastened to some junctions of the transverse fiber using locking nylon cables, aiming to bolster passive strength by intensifying the interaction between the soil and reinforcement. The appropriate use of locking nylon cables was crucial to prevent potential separation between the steel bars and geogrid during pullout. In this investigation, three locking nylon cables were utilized. The second system involved the attachment of plastic dowels to the geocomposite. Both systems were visually depicted in Figure 4.15. The study employed SP-class soil characterized by fine particle content below 1.00%, with an internal friction angle of 35.70° under a load of 1578.00 kg/m³. The natural water content was 0.70%, and the maximum dry unit weight reached 1615.00 kg/m³, indicating a relative density of 80.00%. A PET geogrid with a black polymeric coating was used to provide high tensile strength and low elongation. The geogrid's one-cell area measured 30.00 mm * 25.00 mm, with an open area ratio of 64.00%. According to ASTM D6637, the average maximum tensile strength was determined to be 117.08 kN/m. Additionally, a biaxial geocomposite was incorporated, featuring high-modulus polyester fibers within a non-woven geotextile, and its tensile strength was 60 kN/m. Experimental procedures were carried out using a large direct shear box measuring 30.00 cm * 30.00 cm * 15.00 cm. The top of the box was fixed, while the bottom was free to move, and LVDT was employed to measure vertical displacements. Displacement gauges were utilized to track geosynthetic elongation during shearing. Two tests were conducted for each specimen, and the results demonstrated consistency. The impact of the front face of the test setup on shear behavior was addressed by placing a rubber membrane on the front face. Soil compaction was achieved in three layers using a 6.75 kg rammer with a surface area of 20.00 cm * 20.00 cm, delivering 36 blows to each layer and resulting in a soil compaction degree of 97.00%. Normal stresses of 20.00, 50.00, and 100.00 kPa were applied, and lateral displacements were maintained at a constant rate of 1.00 mm/min.

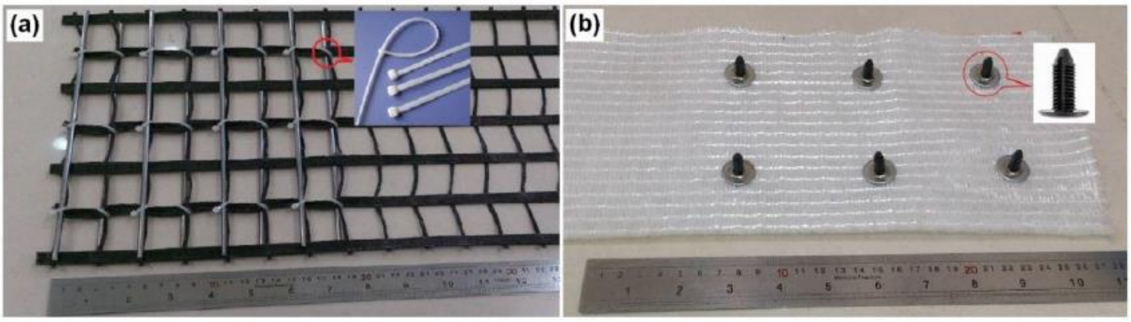

Figure 4.15. *New reinforcement methods a) Geogrid with steel bars and b) Geocomposite with pins (Mirzaalimohammadi et al., 2019)*

The addition of a third-dimensional element to the geosynthetic proved effective in enhancing soil-geosynthetic interaction (Mirzaalimohammadi et al., 2019). Thicker bars were found to reduce displacements by providing higher stiffness and increased passive soil resistance. When displacements between the geogrid and steel bars differed, a decrease in performance was observed. Comparing front and rear displacements revealed that in elongated materials like geogrid, the rear part moved later. Since the force reached the very back of the geogrid later, the least displacement occurred in the rear part. Elastic deformations were observed in the geogrid at low normal stresses, while permanent deformations and bending of transverse fibers were noted under high normal stresses. The strains in the reference geogrid were lower than those in the improved geogrids. In the geocomposite system, the number and arrangement of pins were influential parameters. The displacement of the geotextile forming the geocomposite was greater than that of polyester fibers. Due to the passive resistance captured by the pins, pullout resistance increased. The performance improved with an increasing number of pins and non-sequential arrangement. A more effective pullout resistance occurred when the steel bar spacing and diameter were low. With an increase in normal stress and bar number, unit shape deformation values also increased. The added bars enhanced adhesion, especially by increasing the friction angle. The geogrid with steel bar-sand exhibited more dilation compared to the geogrid-sand. Dilation increased with the number of bars and normal stress. The geocomposite, with added pins, created passive resistance, resulting in increased pullout resistance. The most effective condition was when the pins were not arranged in sequence. The system will provide economic gains in situations where there is limited backfilling space for walls with soil reinforcement.

Han et al. (2018) used both biaxial and triaxial geogrids to examine the effect of soil particle size on the shear behavior of the soil-geogrid interface. Various sizes of crushed limestone aggregates (12.50-19.00 mm, 19.00-25.00 mm, 25.00-37.50 mm) were employed. Biaxial and triaxial geogrids were chosen as reinforcement materials. Experiments were conducted within a large shear box, maintaining a constant room temperature. Soils were layered to achieve a relative density ranging from 55.00% to 58.00%. Tests were carried out under normal stresses of 50.00, 100.00, and 150.00 kPa, with a shear rate of 1.00 mm/min. The experiments concluded upon reaching a displacement of 10.00 cm. With increasing normal stresses, corresponding shear stresses exhibited an upward trend. In terms of the effect coefficient of interfacial shear strength between surfaces, a notable difference was observed between reinforced and unreinforced conditions in the soil, with particle sizes ranging from 19.00-25.00 mm. Conversely, the 12.50-19.00 and 25.00-37.50 soils showed marginal differences. The shear strength presented between interlocked soil samples and the soil particles-geogrid surface. The interlocking effect reduced when particle size was excessively large, resulting in the creation of a large geogrid-aggregate interaction area. Conversely, with very small particle sizes, a low interlocking effect was noted. Successful interlocking occurred when particles could traverse the geogrid aperture and exert an effective confinement effect. The optimal interaction among reinforced soils was identified within the 19.00-25.00 mm particle size range. For biaxial and triaxial geogrids, a better interlocking effect was achieved when the cell size-to-particle size ratio fell within the ranges of 1.30-1.71 and 1.08-1.43, respectively.

In the research conducted by Kayadelen et al. (2018), an experimental investigation was undertaken to assess the pullout resistance of geogrid material within sandy soil. A specially designed apparatus having a unique head, was employed for conducting pullout tests on the geogrid within a shear box. Data acquisition was facilitated through the use of load cells and LVDTs. The saturated unit weight of the SP type of soil, classified as SP, was 2.73 g/cm³. Due to identified limitations of commercially available geogrids for laboratory experiments, a geogrid with a 1.00 cm grid opening and 0.85 mm thickness was fabricated in the laboratory, as seen in Figure 4.16. Experiments were systematically carried out at relative densities of 50.00%, 60.00%, and 70.00%, considering two gradations with particle sizes either below or above 1.00 mm. Varied Normal stresses of 27.20, 54.40, and 108.80 kPa were applied. It was observed that elevated normal stresses amplified pullout resistance as relative density increased. Despite the similarity in the force-displacement curve between the reinforced and unreinforced samples, the reinforced sample displayed a higher maximum pullout force, indicative of a stiffer soil-geogrid interaction. A detailed analysis of the pullout force against normal stress, considering different relative densities, revealed that at 70% density, the lowest result occurred under low normal stress. In contrast, higher relative densities demonstrated improved performance with increasing normal stresses. This phenomenon was attributed to an increased number of particles entering the geogrid cell under high normal stresses, enhancing the locking effect. The relationship between pullout force and normal stress exhibited a linear correlation.

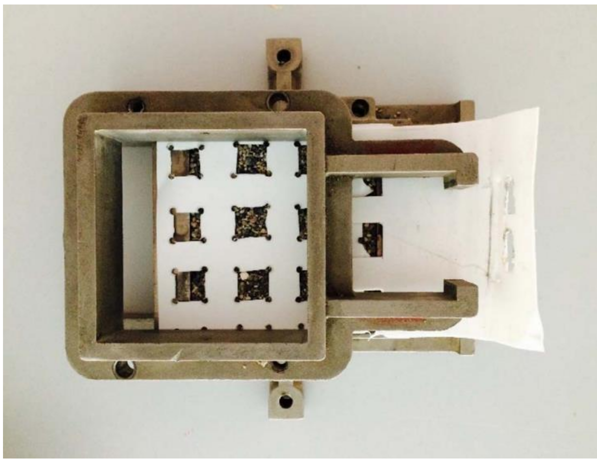

Figure 4.16. *Geogrid utilized in experiments and simple shear box (Kayadelen et al., 2018)*

Mosallanezhad et al. (2016) carried out an experimental investigation comparing the Geogrid-Anchorage (G-A) system (Figure 4.17), formed by integrating geogrid with polymeric anchorage. 10.00*10.00*10.00 mm^3 cubic elements with an elastic bar were embedded on the surface of geogrids at a specific angle, and denoting it as G-A. To compare the normal geogrid with the G-A system, large-scale direct shear box tests were performed. A flexible pressure bag was employed to induce overburden pressure in the test setup, and a rigid plate was utilized to concentrate vertical stresses on the front side of the apparatus. Linear variable differential transformers (LVDTs) were utilized to quantify both vertical and lateral deformations. Test specimens were prepared employing well-graded sand (SW). Two biaxial geogrids with different tensile strengths were implemented in the experiments. Lubricated rubber membranes were preferred over teflon, or smooth aluminum, glass, in order to reduce friction on the sidewalls during shear box testing. The soil was compacted in five layers of 5 cm thickness. One end of the geogrid was clamped, while the other end was left free, and cables were arranged for measurements. After placing the soil, the test setup was compressed, a flexible pressure bag was introduced, and the head used in the shear box test was positioned on top. The upper part of the device was retracted at a speed of 1.00 mm/min, initiating vertical and lateral displacements. No discernible damage was noted in the geogrid-anchorage junction post-tests. Twenty extensive direct shear tests were carried out, establishing G-A systems at a rate of 80 anchors per m^2.

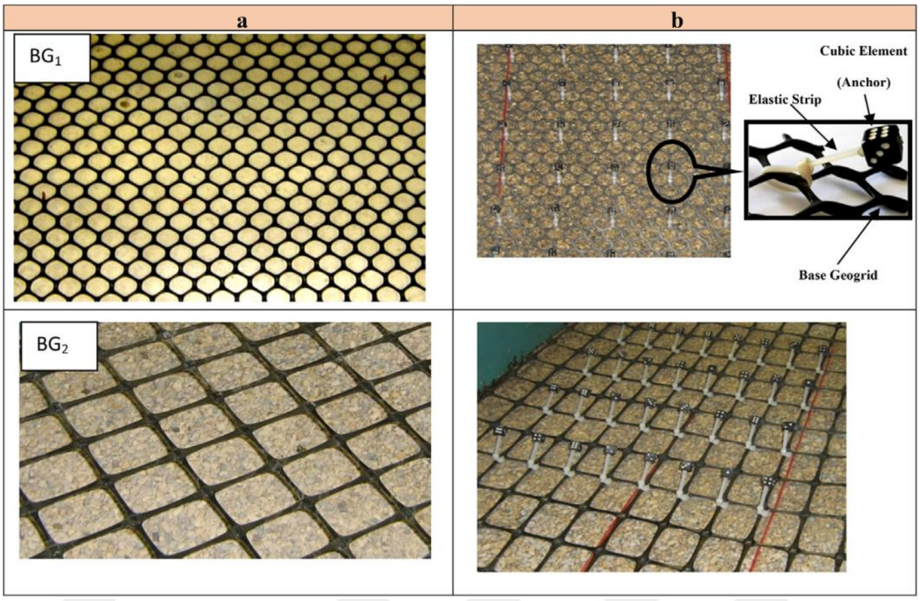

Figure 4.17. *a) Conventional geogrids and b) Grid-Anchor system (Mosallanezhad et al., 2016)*

Due to direct shearing, the sliding mechanism transpired on the upper part of the soil on the reinforcement (Mosallanezhad et al., 2016). Anchors enhanced the direct shear strength since provide a protection against sliding. As depicted in Figure 4.18, the introduction of anchors to the geogrid resulted in an increase in adhesion and internal friction angle. Relative to scenarios employing only geogrid, the interaction of the G-A system with the soil exhibited significantly superior performance. The G-A system achieved the same effect as normal geogrid but with a reduced length. Thus, the adoption of the G-A system proved more efficient than traditional geogrid in locales with restricted rear clearance. The inclusion of anchors mitigated direct shear sliding on the upper surface of the geogrid.

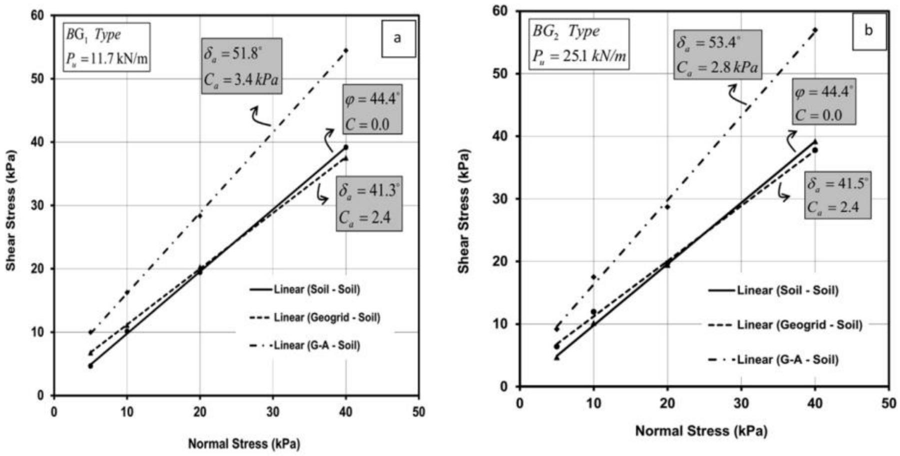

Figure 4.18. *Normal stress-shear stress graph; a) Lower tensile strength and b) Higher tensile strength (Mosallanezhad et al., 2016)*

To investigate the pullout resistance of geogrid in clayey soil, 18 experiments were conducted using miscellaneous clay samples with varying moisture content by Altay et al. (2019). A specialized head, illustrated in Figure 4.19, was devised for executing pullout tests within the shear box test setup, enabling the examination of geogrid pullout behavior in clayey soil. Small-scale geogrids were employed in the experiments. The clay soil was classified as CH through sieve analysis and hydrometer tests. The proctor test determined an optimum moisture content of 21.00%. Alongside the specimen with optimal moisture content, samples with 19.00% and 29.00% moisture content were utilized to analyze the impact of moisture content on the shear box and pullout tests. Normal stresses of 27.20 kPa, 54.40 kPa, and 108.80 kPa were applied to the specimens.

Figure 4.19. *Special cap for direct shear test (Altay et al., 2019)*

The highest pullout force was achieved at the optimal moisture content (Figure 4.20). Notably, the force required to pull the geogrid in clay soil surpassed the maximum force in the shear box test under equivalent stress and displacement conditions for clayey soil (Altay et al., 2019). This indicated that the interaction between the clay soil and geogrid surfaces was better than the interaction within the clay soil itself. According to shear box tests, it was evident that the specimen with optimal moisture content (21.00%) attained higher failure loads. The interlocking effect improved with the increased interaction between geogrid and soil particles. Given that the highest density was attained at the optimum moisture content, the authors pointed out that the locking effect would similarly increase. The findings affirmed that geogrid utilization in clayey soil contributed significantly to pullout resistance.

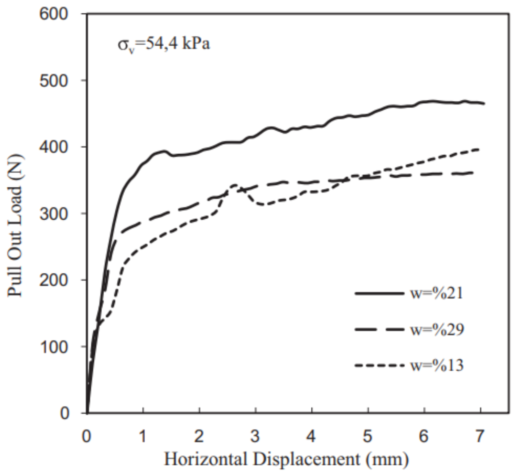

Figure 4.20. *Pullout load-horizontal displacement graph at 54.40 kPa normal stress (Altay et al., 2019)*

Table 4.2 presents a summary of the literature review on direct shear tests for geogrid. The abbreviation "Reinf. Type" in the table denotes "Reinforcement Type". Additionally, geogrid is abbreviated as geog.

Table 4.2. *Studies in the literature related to direct shear tests to determine pullout resistance of geogrid*

Author	Objective	Box Sizes (cm)	Normal Stress (kPa)	Soil Properties					Reinf. Type
				Type	D_r (%)	γ_{dmax} (kN/m^3)	ϕ (°)	D_{50} (mm)	
Mirzaali mohammadi et al. (2019)	Impact of the improved reinfoecement system	30 30 15	20 50 100	SP	97	15.84	36	-	Geog.
Han et al. (2018)	The effect of soil particle size	50 50 36	50 100 150	-	58	-	-	-	Geog.
Kayadelen et al. (2018)	Geogrid Pullout in Sandy Soil	6 6 3	27 54 109	SP	50 60 70	17.06	-	-	Geog.
Mosallanezhad et al. (2016)	Experimental evaluation of Geogrid-Anchorage system versus traditional geogrid	120 60 50	5 10 20 40	SW	70	19.10	44	-	Geog.

Table 4.2. (Continued) *Studies in the literature related to direct shear tests to determine pullout resistance of geogrid*

Altay et al. (2019)	Pullout resistance of geogrid in clayey soil	6 6 3	27.2 54.4 108.8	CH	-	15.01	-	0.005	Geog.

4.3. Load Bearing Tests

Hatami and Doger (2021) investigated the impact of various facing types and reinforcement spacing in geosynthetic-reinforced soil fills. A 2.75 m height testing setup was employed, subjecting it to strip footing loading. Wire extensometers were strategically placed through holes in the test setup for strain measurements, as shown in Figure 4.21. Additionally, hangers were constructed at the front of the test setup to measure lateral deformations during the tests using extensometers suspended from these hangers. The displacements at the top were measured using two wire extensometers. Manual measurements of lateral deformations during construction were taken at 20.00 cm, 60.00 cm, and 100.00 cm distances from the inner wall. The first model incorporated 12 rows of concrete masonry units spaced 0.20 m apart for soil reinforcement, resulting in a total height of 2.40 m. Models two and three utilized four large solid concrete blocks measuring 60.00 cm * 60.00 cm * 120.00 cm, with a total height of 2.51 m and reinforcement spacings of 20 cm in model 2 and 30 cm in model 3. In the case of using concrete masonry units (model 1), the last three blocks, following FHWA recommendations, were filled with steel reinforcement to enhance stability, resulting in a total of 230.00 cm of reinforcement with an additional 115.00 cm layer. Geotextile was placed only 20 cm between the large concrete blocks to minimize interlocking since the thickness of the concrete wall element panels is 20.00 cm. A 3/8" #2 aggregate was utilized, and the internal friction angle of the fill material was 48.00°, with a maximum dry unit weight of 16.50 kN/m³. Concrete masonry units measuring 0.20 m * 0.20 m * 0.40 m and large concrete solid blocks measuring 0.60 m * 0.60 m * 1.20 m were used as facing materials. Concrete wall elements were manually carried, while large concrete blocks were transported using a forklift. Polypropylene woven geotextile was employed as the reinforcement material. Compaction of the fill material was performed using a Jumping Jack, occurring 0.45 m away from the facing to avoid disturbances. A 0.25 m * 0.25 m hand tamper was used to prevent the movements of facing. In models 1 and 2, the main reinforcement material had a spacing of 0.20 m, consisting of 11 layers. A shorter reinforcement material spacing of 0.10 m, with 3 layers, was used according to ASTM. Extensometers were placed where the four reinforcement materials were located in the central region. In model 3, a spacing of 0.30 m was used for 7 layers of reinforcement material, and a spacing of 0.15 m was used for 3 layers of short reinforcement material. A beam measuring 2.45 m in length and 0.20 m in width was used to apply the load from the top. The load was incrementally increased by 50.00-100.00 kPa before each step to ensure the stability of the load cell for the next step. The load was gradually released. The sensors used were carefully removed and calibrated. According to FHWA bridge fill design criteria, a maximum settlement of 0.50% * H is allowed, and it must withstand a stress of 190.00 kPa. Although a considerable load was applied to determine the carrying capacity of model 1, no settlement occurred when the device reached its maximum capacity, so the load was cut off at the 1000.00 kN level. Therefore, while settlement was 160.00 mm in model 1, it was 60.00 mm and 55.00 mm in models 2 and 3, respectively. Under stress of 190 kPa, settlements were below FHWA limits, with settlements of 56.00% and 19.00% lower than model 1 for models 2 and 3, respectively. These results indicate compliance with FHWA design criteria and highlight the contribution of large solid concrete blocks. Surface deformation during loading for models 1, 2, and 3 was 130.00 mm, 15.00 mm, and 25.00 mm, respectively. Despite adjustments to reduce interlocking with large concrete blocks, no sliding occurrence was observed. According to FHWA, surface deformation up to 1.00% of the fill height is allowed, and all models met this condition. Surface deformation under 190.00 kPa stress was 0.60 mm, 0.25 mm, and 0.35 mm for models 1, 2, and 3, respectively. As the load increased, strains also increased. Strains for the second layer of reinforcement material in models 1 and 2 were 0.75H and 0.79H, respectively, while in model 3, the maximum strain in the uppermost layer was 0.88H. Generally, higher reinforcement strains were observed in model 1. All models met FHWA design limits. It was concluded that large concrete blocks are stiffer than concrete wall element covers. The use of large concrete blocks enhances the performance and carrying capacity of geosynthetic-reinforced walls.

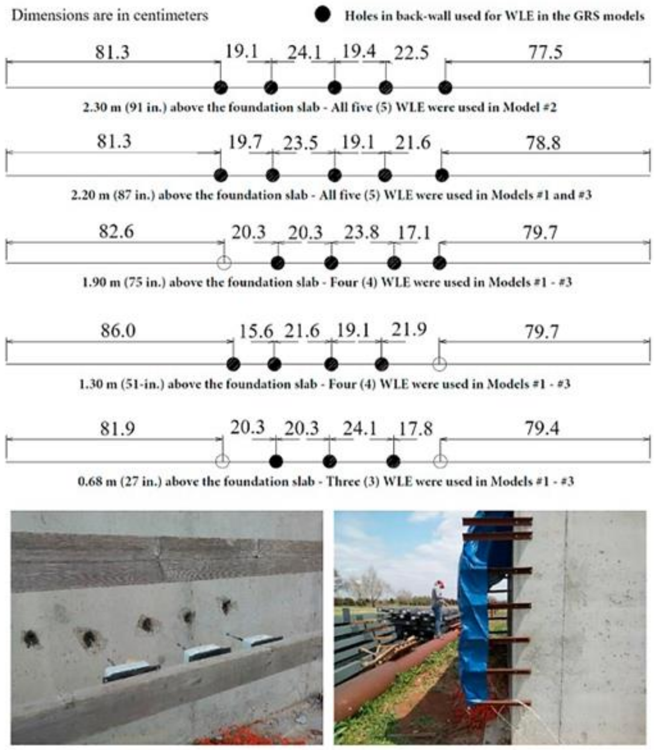

Figure 4.21. *Holes in the rear wall of the test setup, wire-line extensometers, and hangers (Hatami & Doger, 2021)*

Rahmaninezhad and Han (2021) conducted research on 68 geosynthetic-reinforced retaining structures, investigating the impact of foundation load on stability and facing bending. Both wrap-around and modular block facings were utilized in their study. The limit equilibrium method proved highly successful in analyzing slope stability. In that study, the safety factor for 68 geosynthetic-reinforced retaining structures was calculated using the Bishop method, focusing on the critical sliding surface. The critical sliding surface was divided into stable and unstable regions of the geosynthetic-reinforced wall. The contribution of geosynthetic reinforcement depended on the front and rear pullout capacity, as well as the long-term strength of the reinforcement. The Bishop method was an applicable approach for slopes without soil reinforcement. The study incorporated scaled experimental walls, full-scale experimental walls, observed field walls, and numerically modeled walls exposed to foundation loads. As the geogrid length increased, so did the safety factor. Comparing wrap-around facing with modular block facing, the latter's greater rigidity provided a higher safety factor. It's crucial to note that the primary factor influencing the safety factor was not the geogrid. The maximum surface covering deflection was determined by the safety factor calculated through limit equilibrium analysis. The provided equation offered a 95.00% accurate prediction for the maximum lateral surface deflection. The utilization of long soil reinforcement and wrap-around surface covering resulted in a high safety factor. The safety factor for modular block surface covering was higher than that for wrap-around surface covering. The geogrid's impact on the safety factor was noteworthy. As the calculated safety factor decreased with the improved Bishop method, the maximum lateral deflections under foundation load increased. Considering the FHWA standard for surface covering deflection, a safety factor of 2.50 was recommended.

Wang et al. (2020) investigated the mechanical behavior and deformation characteristics of both soil and reinforced soil under the load of a strip footing. In this investigation, the discrete element method was employed. The dimensions of the symmetric part of the soil structure were 50.00 cm in width and 60.00 cm in height. This research explored scenarios involving unreinforced soil, single-layer reinforced soil, and double-layer reinforced soil. The distance between the top surface and the geogrid, along with the openings of the geogrids, was set at 5.00 cm. The case with no geogrid and one layer of geogrid exhibited similarities to a prior laboratory experiment. In the scenario with two layers of geogrid, the bearing capacity was found to be twice that reported in the literature. Maximum tensile forces were concentrated at the geometric boundary, specifically the midpoint of the full-sized geogrid. Under a strip footing load of 80.00 kPa, shear deformation surfaces were revealed at depths of 1.5B and 3.1B. Geogrid stress distribution effectively reduced the maximum stress and alleviated settlements. In an alternative scenario, the behavior of a geogrid-reinforced slope under a strip footing load was scrutinized. Soil reinforcement significantly enhanced the bearing capacity of the slopes. No failure occurred due to soil sliding over the geogrid, and maximum displacements were observed at the top of the slope. In cases involving geogrid usage, punching shear failure was observed, with an increase in the number of used geogrids correlating with an increase in the soil's bearing capacity. Geogrid-reinforced slopes exhibited a substantial increase in bearing capacity.

The application of geosynthetic reinforcement in bridge approaches is a cost-effective solution. The study by Doger and Hatami, (2020) aimed to analyze various facings on bridge approaches subjected to strip footing loads using a full-scale experimental setup. The test box dimensions were 2.75 m in height, 2.45 m in width, and 4.75 m in length. Potentiometer cables were threaded through holes at the back of the experimental setup, with potentiometers placed at heights of 0.70 m, 1.30 m, 1.90 m, and

2.20 m for measuring reinforcement deformation. In the first model (Figure 4.22(a)), 12 rows of concrete masonry units were employed, with no mechanical connection between the reinforcement and facing. In the second model (Figure 4.22(b)) large solid concrete blocks were utilized, and due to the 20.00 cm width of the concrete wall element, only 20.00 cm of geotextile was placed between these blocks. FHWA specified a maximum reinforcement spacing of 30.00 cm, and the vertical spacing used in the study was 20.00 cm. The beam applying the load was positioned 60.00 cm away from the surface covering, adhering to FHWA recommendations. The backfill material consisted of 10.00 mm diameter aggregates, with an internal friction angle of 48.00° and a maximum unit weight of 16.50 kN/m³. A concrete masonry unit measuring 20.00 cm * 20.00 cm * 40.00 cm was used, and large solid concrete blocks measured 60.00 cm * 60.00 cm * 120.00 cm. The top of the large solid concrete blocks featured shear keys. The primary advantage of the concrete masonry unit was its ease of manual placement, whereas a forklift was necessary for the large concrete blocks. Polypropylene woven geotextile served as soil reinforcement, meeting ASTM D4595 standards with a tensile strength of 70.00 kN/m in the machine direction. The experiment initiated with a 7.50 cm thick layer of sand, and facings commenced over this layer. Compaction was carried out 45 cm away from the back of the covering using a jumping jack compactor, with a 25.00 cm * 25.00 cm rammer applied to the front side. A load was applied using a beam measuring 2.45 m in length and 0.20 m in width. Surface covering deformations and vertical settlements were measured during the experiment, with extensometers covered in sand to prevent granular particle damage. The model with a concrete wall element exhibited a maximum load of 1571.00 kN, resulting in an upper surface settlement of 16.00 cm without failure. In the model using large solid concrete blocks, the maximum stress was 2260.00 kPa, and the surface settlement was 5.60 cm. Under a design stress of 190.00 kPa, the model with large solid concrete blocks exhibited 56.00% less settlement than the model with a concrete masonry unit and 74.00% less settlement according to FHWA limits. At the deformation limit of 0.5%H settlement set by FHWA, the design load increased to 3.375 times. Both models met FHWA standards, with the performance improvement of large solid concrete blocks highlighted. According to FHWA, the maximum facing deformation under service stress of 190.00 kPa should not exceed 1%H. Both models satisfied this condition. In the model with a concrete masonry unit, when the FHWA-specified service stress was applied at 7.50 times the recommended level, the maximum limit deformation of 12.00

mm was exceeded. In the model using large solid concrete blocks, even when the service stress was increased to 10 times FHWA recommendations, this limit was not exceeded. According to FHWA, the maximum reinforcement deformation should not exceed 2.00%. Even at a stress of 1900.00 kPa, ten times the service stress, the reinforcement deformations did not exceed the FHWA limit. The use of large solid concrete block facings resulted in lower surface displacements compared to the model with a concrete wall element, indicating an enhancement in bearing capacity and structural performance.

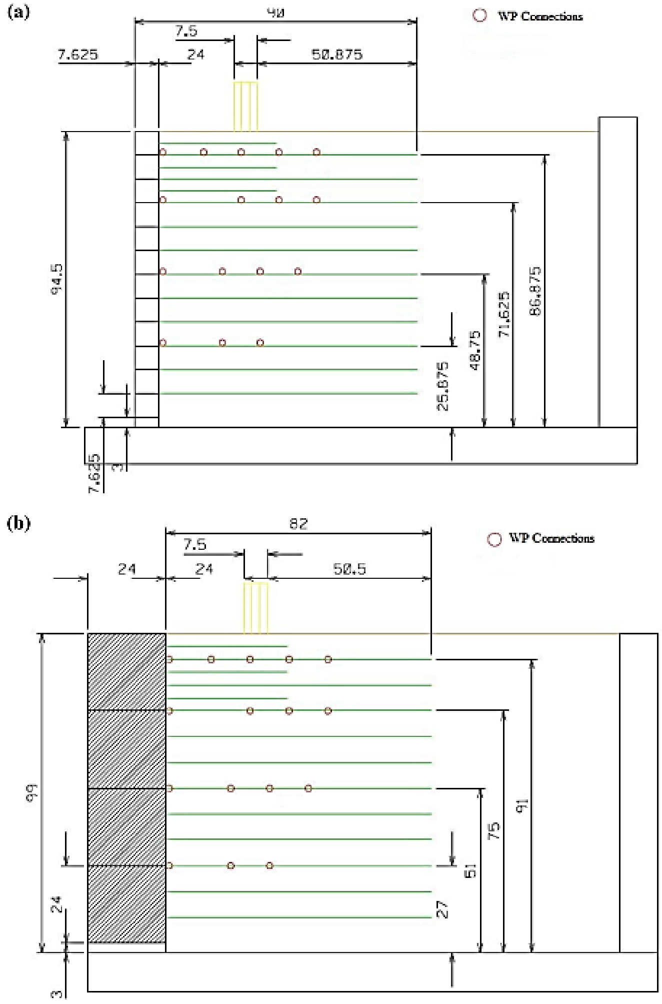

Figure 4.22. *Cross-section of a) Concrete masonry unit model and b) Large solid concrete block model (Doger & Hatami, 2020)*

Zhang et al. (2022) investigated the impact of modular block facing, full-height panel facing, and wrap-around facing on the load-bearing capacity, using dry quartz sand as the fill material. The soil belonged to class SP, with a relative density of 70.00%. The internal friction angle of the soil was 45.00°. A biaxial geogrid with a cell aperture of 30.00 mm * 30.00 mm was used, with a maximum tensile strength of 10.00 kN/m. The bridge approach model was scaled at ¼ (scaling factor $\lambda = 4$) and had a height of 1.2 m since general the height of the bridge approach was 4.8 m. The length of the geogrids was 0.7H and the model dimensions were 1.20 m in length and 1.00 m in width. Experiments were conducted in a steel box measuring 1.60 * 1.00 * 1.60 m. The inside of the box was coated with a 1.00 mm thick PTFE film, and industrial oil was applied to reduce friction. At the bottom of the setup, there was a concrete foundation with a height of 10 cm and a thickness of 30 cm. The modular block's dimensions were 20.00 cm in length, 10.00 cm in width, and 5.00 cm in thickness. Steel pins were used to secure the geogrid to the modular block. The rigid panel facing consisted of a 10.00 cm thick reinforced concrete panel. In contrast, a wrap-around facing was made using geotextile to prevent soil from leaking through the openings of the biaxial geogrid. All LVDT readings were taken from the center, and strain gauges were placed on specific geogrid layers with a calibration factor of 1.16. A piston with a capacity of 300.00 kN was utilized, and the loading beam had a cross-sectional thickness of 2.00 cm and dimensions of 96.00 cm * 30.00 cm. The distance from the loading beam to the surface was 8.00 cm. Loading was applied in increments of 20 kPa up to 100 kPa and then in increments of 50 kPa above 100 kPa, with each step lasting 10 minutes. The experiments were halted when a unit deformation of 4.00% of the structure height was reached. Footing settlements were linear. In the full-size panel facing, it was crucial to note the significant importance of the panel-geosynthetic interface. Under 50 kPa pressure, considering the 1/4 scale, this was equivalent to 200 kPa, and the vertical strain remained below 1.00%, meeting FHWA conditions for service load. As seen in Fig, Surface displacements increased from bottom to top, reached a maximum at 2/3H levels, and subsequently decreased upward direction (Figure 4.23). The highest surface displacement was observed in the wrap-around facing. Stress increase decreased with increasing depth, with the highest stress increase seen in the full-size panel. Lateral stress increase was calculated using FHWA and AASHTO methods, with AASHTO proving more successful in matching experimental data. Geogrid strain increases were examined at different distances from the wall surface. Flexible surface facings yielded higher unit deformation values. Under 50 kPa service pressure, unit deformations were below 2.00%, as recommended by FHWA. Footing settlements and surface displacements were highest in wrap-around facing and lowest in full-size panel facing. All facings met FHWA conditions, indicating the usability of wrap-around facing. The rigid facing resulted in higher stresses. The AASHTO method was more successful in calculating lateral and vertical stress increases. FHWA's use of the

Boussinesq method, based on an elastic region, led to less accurate calculations. Strains due to tension were higher in the case of flexible facings, with more significant deformations in the top layers and at the connections with surface panels.

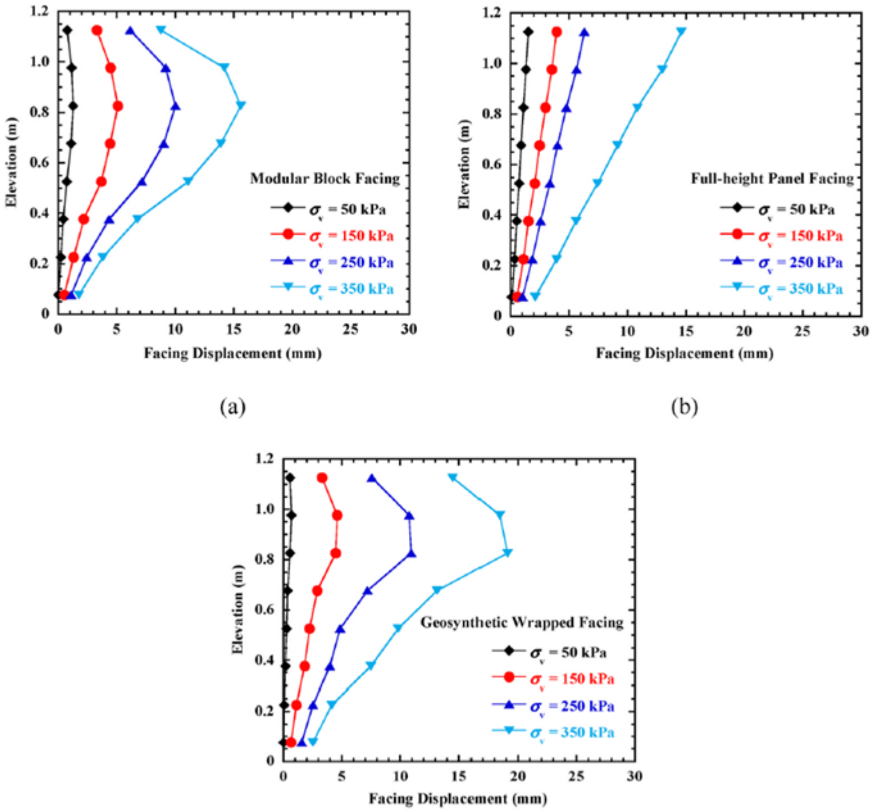

Figure 4.23. *Facing displacement a) Modular block, b) Full-height panel, and c) Wrap-around (Zhang et al., 2022)*

Table 4.3 provides a concise overview of the load bearing tests literature. Geogrid and geotextile are abbreviated as geog. and geot., respectively.

Table 4.3. *Studies in the literature related to load bearing tests for reinforced soil*

Author	Objective	Wall Height (cm)	Facing Type	Soil Properties					Reinf. Type
				Type	D_r (%)	γ_{dmax} (kN/m^3)	ϕ (°)	D_{50} (mm)	
Hatami and Doger (2021)	Impact of facing types and reinforcement spacing on load bearing	240	Concrete masonry units and large solid concrete blocks	3/8”	-	16.50	48	-	Geot.

Table 4.3. (Continued) *Studies in the literature related to load bearing tests for reinforced soil*

Wang et al. (2020)	Mechanical and deformation behavior of reinforced soil	60	-	Sand	70	17.14	41	0.48	Geog.
Doger and Hatami (2020)	Influence of facing type on load bearing performance	275	Concrete masonry units and large solid concrete blocks	3/8”	-	16.50	48	-	Geot.
Zhang et al. (2022)	Impact of facing type on load bearing capacity	120	Modular blocks Full-height panels Wrap-around	SP	70	-	45	-	Geog.

4.4. Reinforced Soil Failure Studies

Geosynthetic soil reinforcements enable the construction of steeper slopes, presenting an opportunity for more efficient land utilization. By this way, Liu et al. (2012) explored the failure mechanisms of a steepened slope reinforced with PET geogrid due to various factors. The reinforced slope, with a height ranging from 10.00 to 40.00 m and an inclination of 40°, was incrementally built in 10.00 m segments. After completing the lower-tier construction in 1994, excavation for the upper tier revealed localized failure, confined to the unreinforced lower tier during intense rainfall. The origin of the sliding was identified as the clay layer. Following the 1999 7.3-magnitude Chi-Chi earthquake, the 40.00 m-high retaining wall, comprising four tiers, experienced sliding (Figure 4.24). There were no indications of geogrid tearing or drainage pipe leakage. Repair work occurred between 2002 and 2004. In 2004, excessive rainfall caused sliding in the clayey natural soil above the reinforced soil, closely resembling the 1994 incident. Below 15.00 m due to soil conditions, a mixture of clay and granular soil was encountered. The groundwater level was at a depth of 100.00 m. Analyses using limit equilibrium and finite difference methods were conducted. The 1994 sliding incident was attributed to a reduction in the apparent cohesion of the water-absorbing clay layer. The 1999 sliding occurred during a high seismic acceleration of 30 seconds, resulting in stress concentration between the backfill, clay layer, and gravel layer interfaces. No internal pullout of the geogrid was observed. The seismic acceleration exceeded the design seismic acceleration. The primary cause of the 2004 sliding was the loss of cohesion in the clay layer and water infiltration at the gravel-clay interface due to heavy rainfall. Issues with subsurface drainage were evident. Rain-induced loss of strength in the clay layer and weakening between the clay and gravel layers led to the sliding. The study concluded that reliance on apparent cohesion in structures reinforced with soil reinforcements is not advisable. The excessive fine content in the backfill and inadequate drainage were identified as fundamental errors. The use of geosynthetics in steep slopes demonstrated successful performance, even though the burial depth of the geosynthetic in high slopes could be costly.

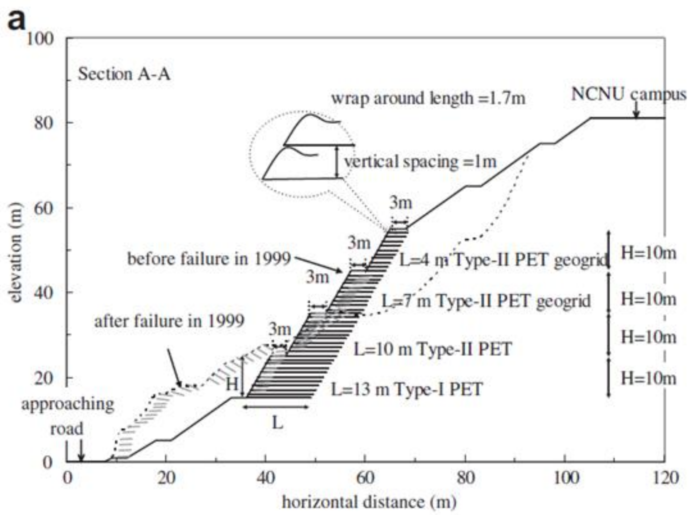

Figure 4.24. *Reinforced slope cross-section before and after Chi-Chi earthquake (Liu et al., 2012)*

Reinforcement length should be at least 70% of wall height (H) according to specifications and guidelines. When its length becomes shorter, higher tensile strength is demanded. The external failure modes of the reinforced earth wall are sliding, overturning, bearing capacity, eccentricity, settlement, and global failures. The internal stability is about pullout and rupture failure modes. The study by Bilgin (2009) aimed to determine the main failure reason when the required minimum length of geogrid reinforcement was applied and to look into its usability as its length was shorter than %70 of H under different conditions. During the external stability analysis, reinforced soil is assumed as a complete rigid body. If the friction force between soil and reinforcement is less than the tensile force, pullout failure is an occurrence. Moreover, the tensile force more than its tensile strength is called rupture failure which is not first-hand about reinforcement length. For this reason, pullout failure was only investigated mode for internal stability. Various parameters such as the height of the wall, surcharge load, vertical spacing of reinforcement, unit weight, and friction angle of reinforced soil, foundation, and backfill soils were investigated. Even if pullout was the main failure mode shown in Figure 4.25, external stability was so important to detect the required minimum reinforcement length. The minimum length of the reinforcement over wall height ratio was 65.00% according to the pullout failure governing mode. When backfill unit weight increased, minimum reinforcement length increased too for external failure modes because of the rise in horizontal force, but the main failure mode was still pullout. The minimum length of reinforcement was suggested to be 0.58H according to backfill unit weight. The governing failure mode changed regarding to backfill friction angle. If it was lower than 34.00°, eccentricity was the main failure mode. The pullout was the main failure when the backfill friction angle was higher than 34.00°. The reinforcement vertical spacing range did not affect the required minimum length of the reinforcement. The required minimum length of reinforcement was reduced by increasing the reinforced soil unit weight for external failure mode, but there was no change in minimum length for pullout governing failure mode. The main failure mode varied in regard to the reinforced soil friction angle. Whereas the pullout failure mode was dominated by a low angle of friction, the eccentricity was the main failure mode for a higher friction angle. Surcharge load ranging between 0.00 and 20.00 kN/m2 was affected after 15.00 kN/m2 since the slope for the pullout changed and it exceeded the minimum requirement length in the resistant zone which was 0.9 m. The unit weight of the foundation soil had no influence pullout governing failure mode, but it minimally affected bearing capacity. The friction angle of soil which is for all such as foundation, backfill, etc. had the most remarkable effect on the required minimum reinforcement length. The most prevalent failure mode is pullout. Hence, the required minimum reinforcement length can be decreased by increasing pullout capacity. It prevents problems caused by limited space behind the wall. Also, reinforcement can connect anchors or nails to the rigid zone. The length of the reinforcement can be 0.5H in favorable conditions. Length of reinforcement impacts lateral wall deformations.

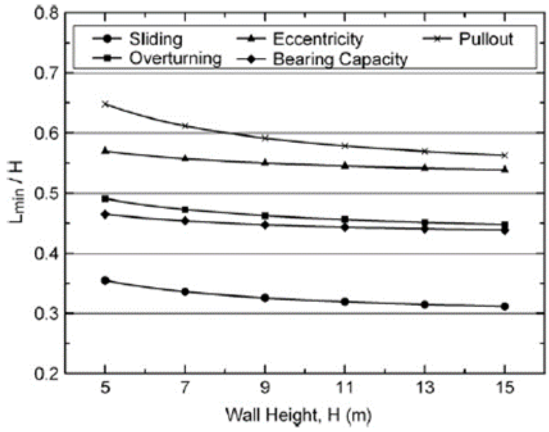

Figure 4.25. *Impact of wall height on required minimum reinforcement length for different failure types (Bilgin, 2009)*

Chen et al. (2000) studied a fundamental analysis of a reinforced soil slope failure induced by the Chi-Chi Earthquake in Taiwan. A comprehensive field observation was carried out to examine the construction of the reinforced zone and collect data on the failure. The primary cause of the failure was not an internal failure mechanism such as pullout or tensile failure. In other words, the factor of safety for the external failure mechanism was found to be less than one according to the analysis.

Segmental retaining walls (SRWs) gained widespread acceptance in North America as a cost-effective alternative to mechanically stabilized earth (MSE) walls that used metallic reinforcing, as well as traditional cast-in-place concrete retaining walls. However, numerous SRWs failed to function as intended, leading to failures across the country. The primary causes of these failures included poor construction and engineering practices, subpar material quality, external factors, and insufficient coordination of responsibilities among the owner, design consultants, and contractor. The investigation by Collin (2001) focused on a retaining wall that exceeded 120.00 m in length and reached a maximum height of 8.50 m, constructed in New England. The primary reinforcement consisted of steel mesh, with geogrid serving as secondary reinforcement. The initial failure occurred at the wall's highest section during a rainstorm in 1999. A second failure transpired during a hurricane later that year, causing the geogrid reinforcement and reinforced fill to detach from the steel mesh-reinforced earth. While every layer, except the top one, met the safety requirements for the pullout, an extension of the top layer of reinforcement was necessary to fulfill the pullout requirement. An essential consideration during both the design and construction of these systems was the connection between the reinforcement and the facing of a segmental retaining wall.

Ling et al. (2001) conducted a study on the Chi-Chi Taiwan earthquake. The wall's designer failed to account for seismic activity, possibly influenced by topographic and economic considerations leading to suboptimal design. Cracks in the wall indicated instances of compound failures or inadequate global stability in some constructions. The transverse direction of reinforcement must be large enough to withstand the dynamic earth pressure. Comparative analysis revealed that the reinforced section of the wall exhibited superior performance compared to the unreinforced portion.

Drainage issues, heavy equipment operating near the wall face, and inadequate compaction of the reinforced fill were common problems that led to the failure of reinforced earth walls. Scarborough (2005) investigated two walls. Wall A, with clayey backfill and a height of 9.1 m, used segmental masonry blocks as facing. The observed failure primarily occurred in the wall's block and crushed stone facing in front of the reinforced backfill. While the reinforced soil mass seemed largely intact, the geogrid reinforcement appeared to have pulled away from individual blocks. Wall B, standing at 8.5 m, used geogrid and clayey backfill, with segmental masonry blocks for facing. Movement of retained backfill caused the failure. Investigations revealed that the lack of drainage was the main reason for the devastating failure of Wall A. Unstable compaction and clayey backfill within the reinforced zone also contributed to the failure. Wall B's failure was attributed to the use of short geogrid, directly linked to the failure of global stability analyses during its design. The use of clayey backfill within the reinforced zone may have played a role in the failure. These incidents underscored the importance of avoiding clayey or poorly draining soils.

The first 6-year lifespan of a 300.00 m section of segmental geosynthetic reinforced retaining wall was examined by Yoo (2004). The maximum height of it was 9.80 m. Modular blocks were used to build the wall. The wall had experienced major construction-related issues, ranging from extreme lateral bulging to a partial collapse, according to an assessment of the available construction documentation. Extreme strains in the reinforcement were observed during the construction stage due to substantial wall movement. This work shows how important construction quality is.

The failure and failure triggering mechanism of geosynthetic reinforced segmental retaining wall was studied by Yoo and Jung (2006). It collapsed 2 months after the construction stage. The factor of safety for external and internal stability was lower than the standards. The soil quality of the site did not meet the project since it contained fine-grained particles. Lack of drainage led to failure during heavy rainfall. The importance of backfill soil, design of structure, and following principles of geotechnical engineering were understood.

5. MATERIALS

5.1. Soil

The soil used as backfill in the pullout and load-bearing experiments was taken from the site of the MSE wall project site in Bursa, Mudanya. Therefore, the utility of real soil would lead to more authentic outcomes within the context of experimental studies, instead of artificial soil mixture. The construction details of the MSE wall and the modular block facing are given in Figure 5.1.

Figure 5.1. *The construction site of the MSE wall*

Sieve analysis and hydrometer test were conducted according to ASTM D6913/D6913M-17 and ASTM D7928-21e1, respectively. The soil predominantly adhered to the gradation range specified by the Technical Specification of the General Directorate of Highways of the Türkiye (2013), with minor deviations (Figure 5.2). Nevertheless, despite the fine content of the soil measuring 16.21%, surpassing the stipulated 15.00% limit for MSE structures, the decision to utilize this soil as fill material was made. This determination was based on both the modest exceedance of the 15.00% limit by only 1.21% and the practical consideration of sourcing the soil from a real construction site. Despite the presence of relatively large-diameter granular particles in the field, significant pieces were manually removed due to the inadequacy of the pullout test apparatus for these particle sizes. Consequently, the fine content of the soil used in the study was higher compared to the field soil.

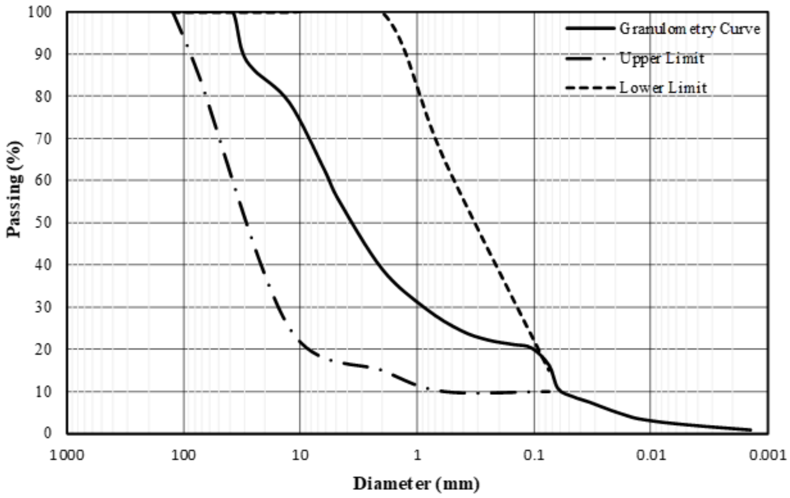

Figure 5.2. *Granulometry curve of backfill soil*

Using the D_{10}, D_{30}, and D_{60} values provided in Table *5.1*, the C_u and C_c values were calculated as 93.37 and 2.30 by using Equations (5.1) and (5.2), respectively. Additionally, the soil's gravel, sand, silt, and clay contents are 44.59%, 39.20%, 15.07%, and 1.14%, respectively.

Table 5.1. *Diameter of soil particles according to passing percentage*

D_{10}	0.061 mm
D_{30}	0.900 mm
D_{50}	3.848 mm
D_{60}	5.732 mm

$$C_u = \frac{D_{60}}{D_{10}} \tag{5.1}$$

$$C_c = \frac{{D_{30}}^2}{D_{10} * D_{60}} \tag{5.2}$$

The soil that passed through the No. 40 sieve in a dry state exhibited non-plastic characteristics, as the liquid limit was not determined through Atterberg limit tests following the guidelines of ASTM D4318-17. Non-plastic soils are categorized as silt (M). Consequently, based on the Unified Soil Classification System (USCS), the soil was designated as silty gravel with sand (GM), as illustrated in the provided Figure 5.3.

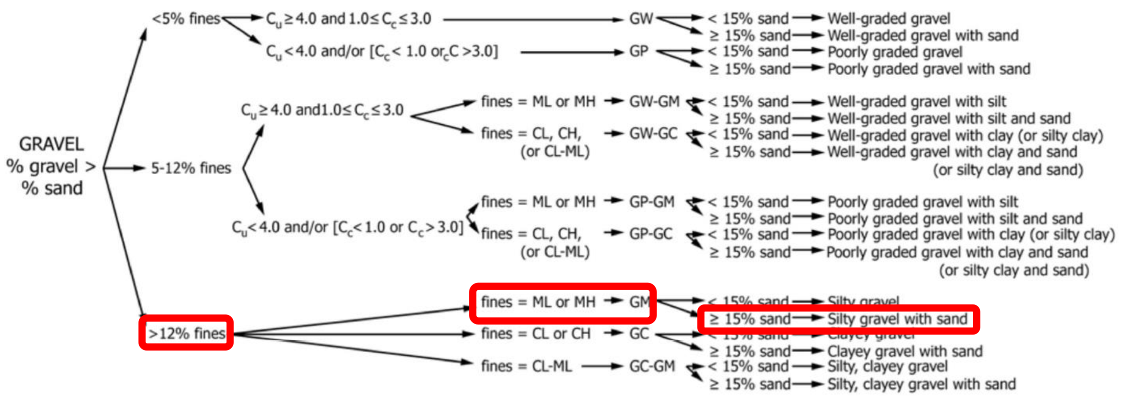

Figure 5.3. *Soil classification schema for gravel* (ASTM Standard D2487-17)

The determination of specific gravity followed the procedures outlined in ASTM D854-14. Two tests were performed, and the average result is presented in Table 5.2. Utilizing the Equation (5.3) with a water density (ρ_w) of 0.997 g/cm³, the specific gravity (G_s) was calculated to be 2.70.

Table 5.2. *Specific gravity of soil*

	Test 1	**Test 2**
Dry soil mass (m_1), g	50.00	70.00
Water + Pycnometer mass (m_2), g	658.70	658.45
Water + Pycnometer + Soil mass (m_3), g	690.22	702.65
Specific gravity (G_s)	2.70	2.71
Average Specific gravity (G_s)	**2.70**	

$$G_s = \frac{\rho_w * m_1}{m_1 + m_2 - m_3} \tag{5.3}$$

The outcome of the Proctor test conducted in accordance with ASTM D698-12 revealed that the maximum dry unit weight (γ_{dmax}) of the soil was established at 22.78 kN/m³, with an associated optimum water content (ω_{opt}) of 13.16% (Figure *5.4*).

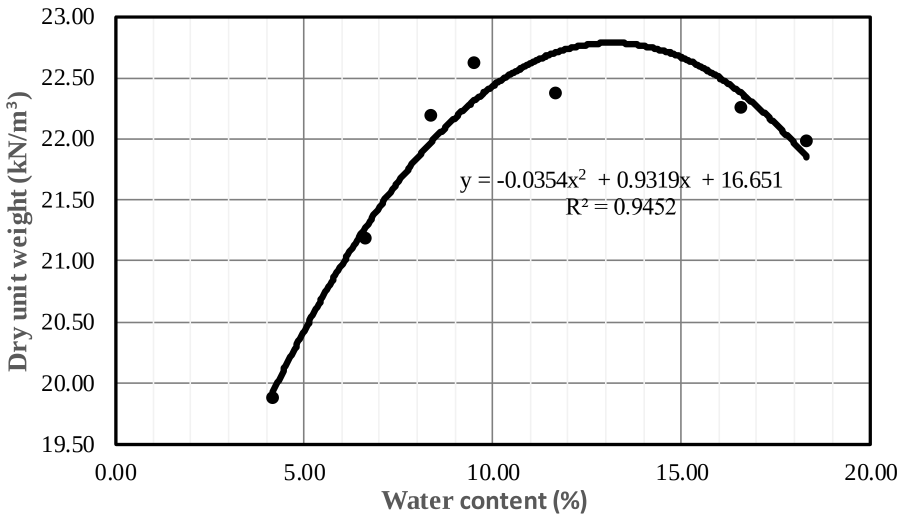

Figure 5.4. *Standard proctor test graph*

The ASTM D1556/D1556M-15e1 standard sand-cone method was employed to ascertain the unit weight of compacted soil for pullout and load bearing tests in order to determine the in-situ unit weight. The experimental stages are given in Figure 5.5. The water content of the soil obtained from the excavated pits for pullout and load bearing tests was measured at 0.47% and 1.34%, respectively. The natural unit weights (γ_n) of the compacted soil of the pullout and load bearing tests was determined as 22.69 kN/m³ and 21.04 kN/m³, respectively. Even though the water content of soil was low enough to be ignored, the dry unit weights (γ_d) for pullout and load bearing were calculated 22.59 kN/m^3 and 20.77 kN/m^3 according to Equation(5.4). The calculated γd from the sand-cone test and γdmax from the Proctor test were then utilized to find the compaction ratio (R_c). The compaction ratios were determined to be 99.13% and 91.15% for pullout and load-bearing tests, respectively, using the Equation(5.5).

$$\gamma_d = \frac{\gamma_n}{1 + \omega} \tag{5.4}$$

$$R_c = \frac{\gamma_d}{\gamma_{dmax}} \tag{5.5}$$

(a) (b)

(c) (d)

Figure 5.5. *The stages of sand-cone test; a) Locating and fixing metal ring, b) Digging pit and collecting the soil, Pouring the standard sand into the pit c) in pullout test setup and d) in load bearing test setup*

The strength parameters of soil were assessed through the application of the direct shear test (ASTM D3080/D3080M-23). The configuration of the disassembled direct shear test box and the direct shear test device are illustrated in Figure 5.6 (a) and (b). Testing was conducted at normal stress levels of 50.00, 100.00, and 150.00 kPa. The corresponding maximum shear stress for each normal stress level is given in Figure 5.7. For pullout and load bearing experiments, the compaction ratios of the soils varied, leading to the determination of the quantities of soil required for the direct shear test based on their respective natural unit weights. The cohesion value of soil was assumed to be 30.00 kPa. The friction angle (ϕ) and cohesion (c) values for the soil used in pullout tests at the 99.13% compaction ratio, were computed as 56.19° and 30.00 kPa, respectively (Equation(5.6), Figure 5.7(a)). In the load bearing tests, employing soil at a 91.15% compaction level, the cohesion (c) and friction angle (ϕ) values were found to be 30.00 kPa and 51.86°, respectively (Figure 5.7(b)).

$$\tau_f = \sigma * \tan(\phi) + c \tag{5.6}$$

(a) (b)

Figure 5.6. *The direct shear a) disassembled box and b) test device*

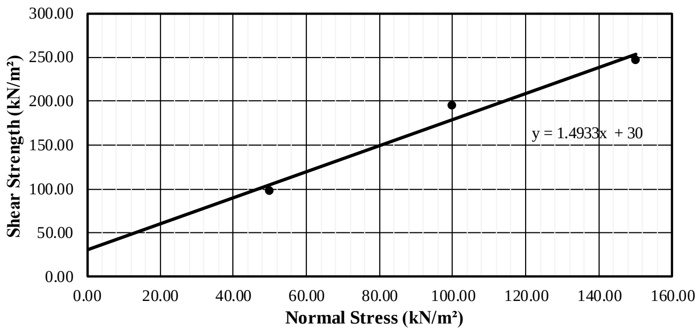

(a)

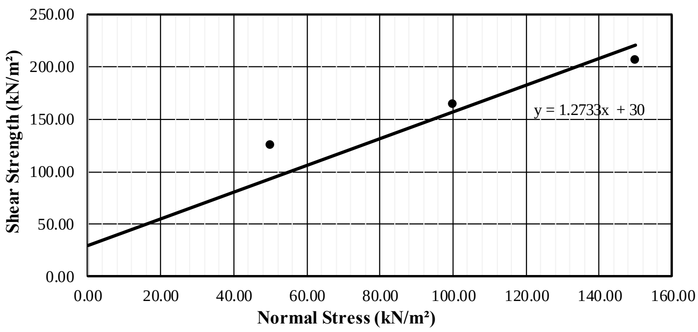

(b)

Figure 5.7. *Shear strength versus normal stress graph; a) Pullout and b) Load bearing*

5.2. Geogrid

In this study, biaxial PET geogrid was utilized. Material properties were presented in Table 5.3, and the tensile tests for machine direction (MD) and counter machine direction (CMD) were conducted according to the EN ISO Standard 10319. The aperture sizes of geogrid were 22.00 mm for longitudinal ribs and 18.00 mm for transverse ribs (Figure 5.8). In addition, the width of the transverse ribs, the width of the longitudinal ribs, and the thickness of both ribs were 10.00 mm, 6.75 mm, and 2.50 mm, respectively.

Table 5.3. *Properties of geogrid*

Property	Direction	Value
Tensile Strength (kN/m)	MD	108.00
Extension at nominal tensile load (%)		10(±3)
Tensile Strength (kN/m)	CMD	≥ 100.00
Extension at nominal tensile load (%)		10(±3)

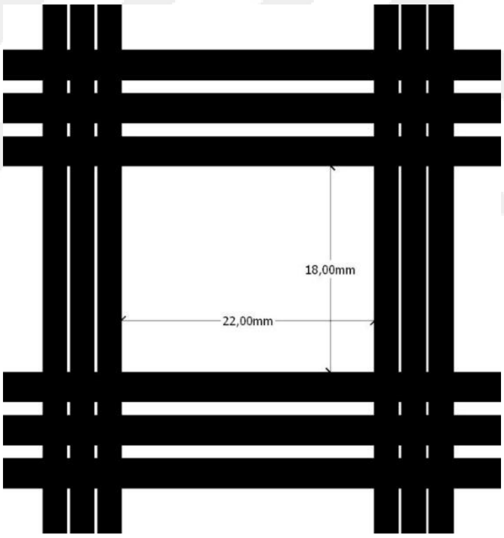

Figure 5.8. *Aperture detail of geogrid*

5.3. Geomembrane

In the context of this study, a 2.00 mm-thick HDPE geomembrane has been employed, which has commonly used in solid and liquid waste storage areas, tunnels, water channels, roofs, pools, and artificial lakes. This material, placed perpendicular to the geogrid plane with the transverse fibers in front, aims to enhance the bearing resistance value. The specifications of the geomembrane are presented in Table 5.4, obtained from the company that provided the geomembrane for this project.

Table 5.4. *Geomembrane properties*

Property	Value
Thickness (mm)	2.00
Density (g/cm^3)	0.96
Tensile strength (N/mm^2)	≥ 24.00 (Fracture)
	≥ 16.00 (Yield)
Strain (%)	≥ 600.00 (Fracture)
	≥ 9.00 (Yield)
Tear resistance (kN)	≥ 125.00
California Bearing Ratio (kN)	> 3.00
Permeability (m^3/ (m^2 day))	≤ 4*10^{-6}
Carbon black content (%/mass)	2.00-3.00
Oxidation time (min)	≥ 100.00

5.4. Geogrid with Geomembrane Barriers

After undergoing specific processes, geogrid and geomembrane were combined. These processes were explained step by step.

- As the first step, geomembranes were cut to the desired length and height. Initially, after setting a specific height, geomembrane pieces obtained through cutting devices (Figure 5.9). The height of geomembrane barriers was 32.00 mm, and the length was 488.75 mm for pullout and 1392.00 mm for load-bearing.

(a) (b)

Figure 5.9. *Geomembrane cutting process a) Fast-cutting device and b) Cutting tool*

- For the geomembranes undergoing the cutting process, study involved the use of a specially designed perforation blade (Figure 5.10) to create the required gaps for passing the geogrid longitudinal ribs. These openings were created at 20.00 mm intervals, with a height of 17.00 mm and a width of 8.75 mm (Figure 5.11).

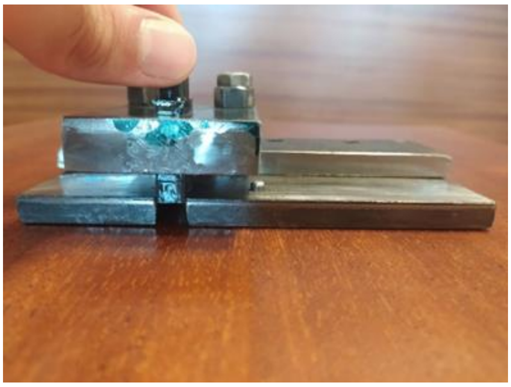

(a)

(b)

Figure 5.10. *Specially designed perforation blade a) Front view and b) Isometric view*

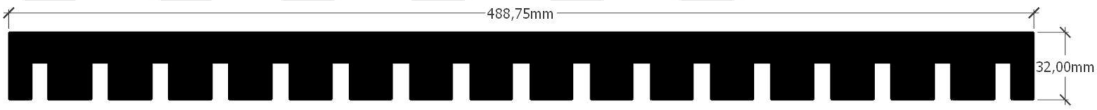

(a)

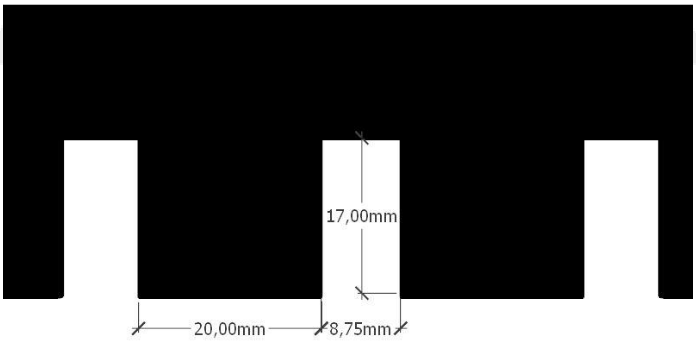

(b)

Figure 5.11. *Gaps in the geomembrane a) Front view and b) Details*

- After passing the longitudinal ribs of the geogrid through the opened gaps, geomembranes of height 14.25 mm were cut to cover the hole gap that remained at the bottom. When selecting the height 14.25, it was adjusted to leave a gap of 2.75 mm after joining, considering the thickness of the geogrid's longitudinal ribs as 2.00 mm. Despite attempting to secure the cut geomembranes to the lower part by melting them with heat to find another option for joining, this method proved unsuccessful (Figure 5.12(a)). The joining process was achieved using staples, which were provided for the lower and upper pieces and the assembled state within every two rows (Figure 5.12(b)).

(a) (b)

Figure 5.12. *a) Attempt to fuse geomembrane pieces by melting with heat, and b) Lower piece, upper piece, and geomembrane joined with staples*

- For the pullout test, geogrids were cut into 1400.00 mm and 490.00 mm dimensions. For the load-bearing test, two geogrids of dimensions 1040.00 mm and 1250.00 mm were overlapped by 640.00 mm and joined with the geomembrane barrier (Figure 5.13). In the joining process, the gaps in the upper part of the geomembrane were first placed onto the longitudinal ribs of the geogrid, and then the lower geomembrane piece was stapled. This method was believed to be much more effective for achieving overlaps.

Figure 5.13. *The assembled form of geogrid with additional transverse elements*

- Samples without geomembrane and samples containing geomembrane barriers with every 2 ribs, every 4 ribs, and every 8 ribs were created (Figure 5.14). The fundamental purpose of using geomembrane at different intervals was to investigate the impact of geomembrane barrier spacing on bearing resistance. The distances between the elements were 56.00 mm, 112.00 mm, and 224.00 mm for cases every 2, 4, and 8 ribs, respectively. In pullout and load bearing tests, 4, 8, and 16 geomembrane barriers were utilized. Since pullout tests were conducted under 3 different normal stresses, 3 samples were produced for each specimen. In addition, as experiments were also applied to standard geogrids without additional elements, a total of 12 samples were created for the pullout (Figure 5.14). For load bearing, the total number of samples was 9, including both samples with and without additional elements (Figure 5.15).

Note: *Throughout the thesis, the elements added in front of the transverse ribs of the geogrid were referred to as either geomembrane barriers or additional transverse elements. Following this section of the thesis, samples without geomembrane barriers were denoted as "reference," while samples containing 4, 8, and 16 geomembranes were designated as "4T," "8T," and "16T," respectively.*

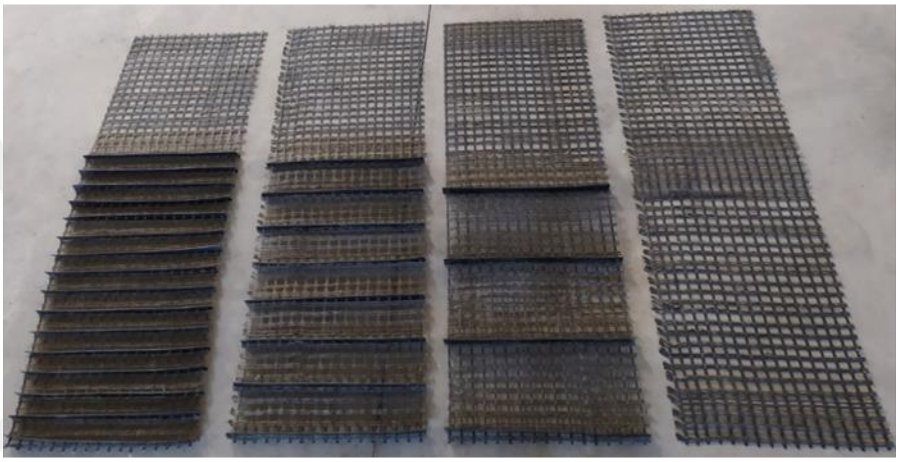

Figure 5.14. *Specimens of pullout tests, from left to right: 16T, 8T, 4T, and reference samples*

(a)

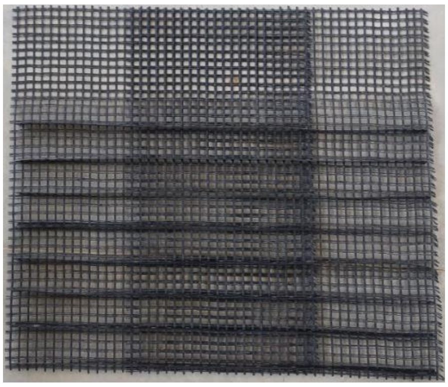

(b)

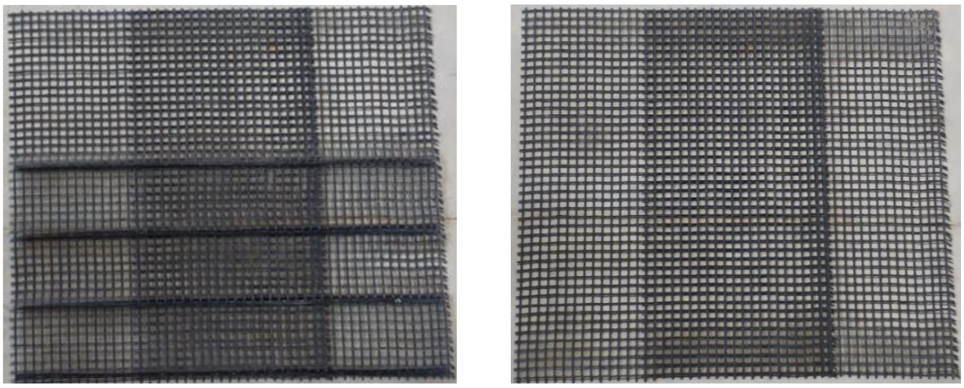

(c) (d)

Figure 5.15. *Specimens of load bearing tests, a) 16T, b) 8T, c) 4T and d) Reference*

The rolled form of the geogrid created by adding transverse elements is shown in Figure 5.16. These elements allowed it to be rolled up, eliminating the need for extra space in the trucks used for transportation. Therefore, it does not acquire extra transportation costs.

Figure 5.16. *The rolled form of the sample containing additional transverse elements (16T)*

5.5. Modular Block

For the conducted load bearing experiments, the facing of the MSE wall was consisted of modular blocks. These modular blocks, with dimensions of 400.00 mm in length, 240.00 mm in width, and 250.00 mm in height, were the same blocks used in the construction site where the soil was obtained. The Figure 5.17 depicts the dimensions and on-site appearance of the utilized modular blocks. They achieved a more effective interaction because they had protrusions that fit into each other's spaces. Moreover, mass of a modular block was 25.50 kg.

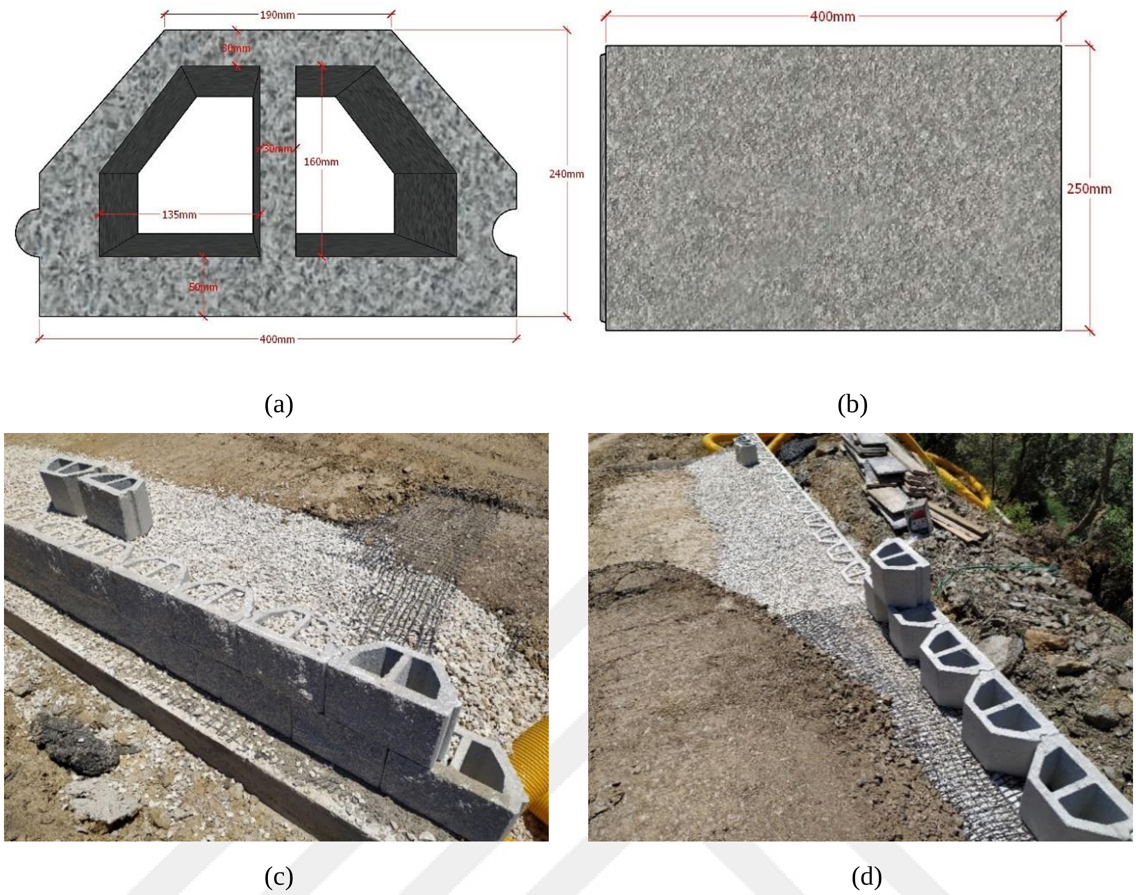

Figure 5.17. *a) Top view and b) Front view of the modular block in the SketchUP model; c) Front view and d) Isometric view of modular blocks on-site*

6. PULLOUT TEST

The experiment was conducted with the objective of evaluating the resistance to the pullout of soil reinforcements from the soil. Within the framework of our research, this experiment was conducted following the ASTM Standard D6706-01.

6.1. Pullout Test Setup

Considering the specifications outlined in the ASTM D6706-1 standard, a testing box measuring 1080.00 mm (length), 600.00 mm (width), and 440.00 mm (height) was fabricated within the facilities of the Central Workshop at Eskisehir Technical University. The primary framework of the testing box was constructed through the welding of metal profiles with dimensions of 40.00 mm * 40.00 mm. Later, all surfaces formed by these profiles (without the top side only), were sealed by welding 3.00 mm thick metal plates (Figure 6.1). The upper section remained open as normal stresses were applied from the top. Normal stresses were induced using 30.00 mm thick metal plates with surface areas of 510.00 mm * 510.00 mm and 510.00 mm * 455.00 mm. The larger plate had a mass of 60.62 kg, while the smaller plate had a mass of 53.86 kg.

Figure 6.1. *Welding of metal plates*

In the central region of the front face through which the geogrid crossed, a space of 30.00 mm was carefully left. To mitigate the potential issue of soil particle spillage from this space, brushes were added. Also, in anticipation of stresses occurring on the front face during pullout, metal profiles were placed both above and below the space to enhance the structural strength. Upon the completion of the test setup construction, efforts were made to minimize friction between the soil and the test box by applying grease between the surfaces and introducing two layers of expanded polystyrene (EPS). This approach aimed to reduce friction to a minimum, aligning with similar endeavors in other referenced studies (Briançon et al., 2011; Cardile et al., 2017; Cazzuffi et al., 2014; Zhou et al., 2012). To circumvent the impact of the front face, various methods were employed in the pullout apparatus, including the direct application of pulling force from within the box (Lajevardi et al., 2014) or the placement of geomembrane on the front face (Mirzaalimohammadi et al., 2019). Through the application of EPS and grease, the flexibility of the front face was enhanced, thereby influencing the rigidity of the frontal face without affecting the pullout test results. In the EPS application, a preliminary step involved the application of grease to the surfaces. Subsequently, EPS with a thickness of 20.00 mm, cutting to the desired dimensions and thickness (Figure 6.2(a) and (b)), was positioned on the greased surfaces as seen in fig. A second layer of EPS, also 20.00 mm thick, was then added, and by applying grease, a test box featuring EPS-covered internal surfaces was achieved (Figure 6.2(c)).

(a) (b) (c)

Figure 6.2. *Application of grease and EPS inside the box: a) Cutting of EPS, b) Adjustment of EPS thickness to 20.00 mm, c) Application of grease, d) Final state of the box with applied EPS*

The plan view and profile view of the experimental setup were depicted in Figure 6.3. Despite being a profile view, EPS, soil, and geogrid were included to provide a more accurate representation of the internal dimensions of the box. Following the placement of EPS, the interior volume of the box has narrowed to 1000.00 mm * 520.00 mm * 360.00 mm. The Linear Variable Differential Transformers (LVDTs) employed for measuring head displacement had a capacity of 100.00 mm, while the hydraulic jack and load cell had a load capacity of 100.00 kN were assembled. At the maximum normal stress level, strain gauges (SG) were strategically positioned at distances of 225.00 mm and 680.00 mm from the back of the geogrid (Figure 6.5). SGs were specifically placed on the longitudinal rib situated in the center of the geogrid, exposed to the highest axial stress due to transverse ribs. The SG at a 225.00 mm distance from the geogrid's back had 1, 2, and 4 remaining transverse elements behind it in samples 4T, 8T, and 16T, respectively.

Likewise, different numbers of transverse elements were present behind the other SG. The objective was to investigate the impact of varying transverse element numbers on the longitudinal rib. In the implementation of the strain gauge, the designated area was thoroughly cleaned with acetone as the initial step. Subsequently, quick adhesive was applied to the strain gauge, and it was affixed to its intended position with a gentle, controlled pressure using teflon paper. To ensure the stability of the strain gauge cable and prevent any displacement, it was firmly secured to the adjacent junction using cable tape (Figure 6.5). For data collection during the experiments, a datalogger and laptop were utilized (Figure 6.4).

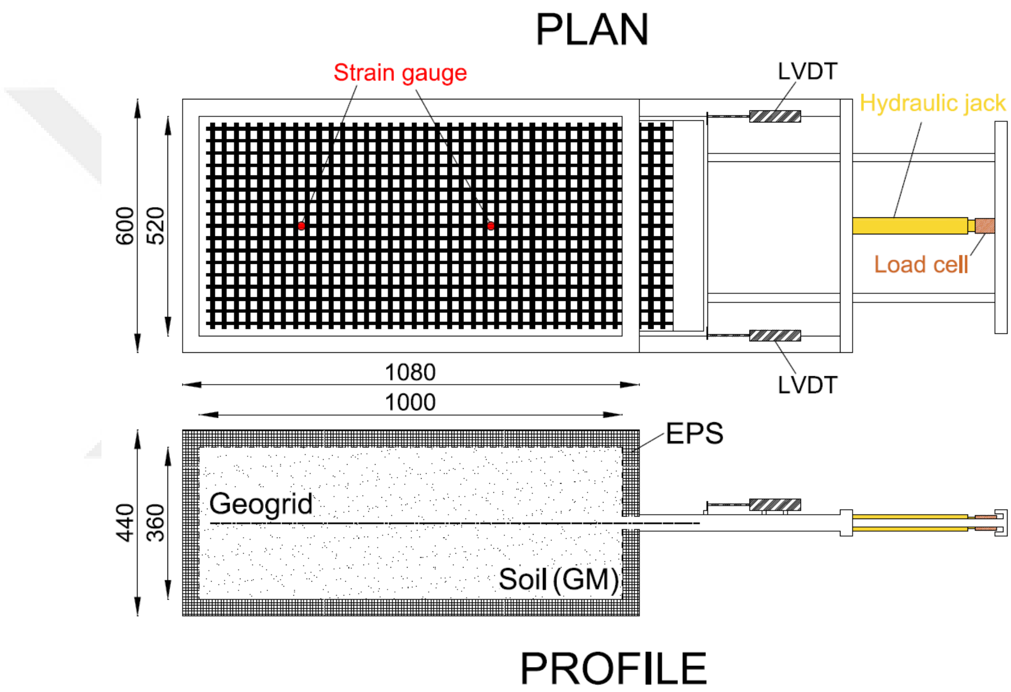

Figure 6.3. *Plan and profile view of pullout test setup and dimensions in mm*

(a) (b)

Figure 6.4. *a) Pullout test setup, and b) Datalogger*

Figure 6.5. *The 4T sample with two strain gauges*

6.2. Pullout Procedure

In the initial phase, soil up to a height of 120.00 mm was compacted using a soil vibration plate compactor with a 2.00-ton force, that was moving from the rear of the experimental setup to the front within 5 seconds (Figure 6.6(a)). Special attention was given to prevent the compactor from contacting the surfaces of the box during this process. Areas inaccessible to the compactor were compacted using a compaction hammer while dropping a cubic object mass of 6.30 kg from a height of 1.00 m, applied 15.43 kJ/m^3 of energy to compact the soil (Figure 6.6(b)).

(a) (b)

Figure 6.6. *a) Soil compactor and b) Compaction hammer*

In the next phase, an additional 60.00 mm layer of soil was added onto the previously compacted soil with a height of 120.00 mm to achieve a smooth surface.

Geogrid was then positioned over this surface, passing through the designated gap on the front face of the apparatus. The frontal section of the geogrid was folded by 200.00 mm, accurately placed into the clamp, and secured with tightened bolts. It was crucial to ensure the firm tightening of bolts, as any looseness could cause the geogrid to slip off or failure during the experiment (Figure 6.7). During the placement of the 60.00 mm soil over the geogrid, attention was paid to preserving the vertical alignment of geomembrane barriers and preventing any deviation from the transverse ribs. With the addition of the 60.00 mm high soil, the identical compaction procedure applied to the first soil layer was applied to this layer upon completing the second layer with a height of 120.00 mm. Then, the third soil layer, measuring 120.00 mm in height, was incorporated into the structure, bringing the total height to 240.00 mm, and subjected to the same compaction process. After undergoing a three-stage compaction process, the outcome was a soil layer measuring 360.00 mm in height, exhibiting a compaction degree of 99.13% regarding to proctor and a unit weight of 22.69 kN/m³.

Figure 6.7. *Unsuccessful pullout test due to the loosen of bolts*

In the third stage, plates for generating normal stress were placed through the top opening of the test setup using a load-lifting magnet and lifter (Figure 6.8). Experiments were conducted at three different levels of normal stress, calculated according to the Equation(6.1) and denoted as 6.24, 8.40, and 10.56 in kPa.

$$\sigma_N = \sigma_s + \sigma_a \tag{6.1}$$

σ_N : Normal stress, kPa

σ_s : Normal stress created by surcharge load over the geosynthetic

σ_a : Normal stress due to applied load

Figure 6.8. *The lifting operation of loading plates*

The experiments adhered to the ASTM D6706-01 standard and were conducted at a rate of 1.00 mm/min. Due to the use of a hydraulic jack as the pullout force loading device, the rate was manually adjusted during the test based on real-time readings. The experiments concluded when an average LVDT reading of 80.00 mm was achieved. At the initial stage, the elements of the pullout test setup, which had been subjected to high stresses, were strengthened through implemented improvements (Figure 6.9).

(a) (b)

Figure 6.9. *The pullout test setup a) Before and b) After improvement*

6.3. Results and Discussions

The results of pullout tests conducted to determine the influence of transverse elements are presented in Figure 6.10. The average displacement values obtained from both sides of the clamp, where the front part of the geogrid was fixed, were plotted along the x-axis of the graphs. The y-axis represents the effect of force applied by the hydraulic jack per unit width. Equation(6.2) from ASTM D6706-01 was employed to determine the pullout resistance per unit width. Upon examination of the graphs, the clear impact of geomembrane barriers was evident.

$$P_r = \frac{F_p * n_g}{N_g} \tag{6.2}$$

P_r : Pullout resistance, kN/m

F_p : Pullout force, kN

n_g : Number of longitudinal ribs per unit width

N_g : Number of longitudinal ribs of the geogrid test specimen

The experiments were conducted at three different normal stresses, 6.24 kPa, 8.40 kPa, and 10.56 kPa. At 6.24 kPa, the peak pullout resistances of the samples varied between 21.73 kN/m and 38.46 kN/m. As seen in Figure 6.10(a), the slope of the curve for 16T was steeper than the other samples in the initial stage. This could indicate that the sample with more geomembrane barrier achieved strength more rapidly compared to other samples. The impact of using 4 additional transverse elements was relatively low, as the maximum pullout resistance difference between the reference and 4T samples was around 3.00 kN/m. In particular, the 8T and 16T samples demonstrated significantly successful performance, exhibiting pullout resistance increases of 59.00% and 77.00% due to the reference specimen, respectively. At a normal pressure of 8.40 kPa, the 4T sample exhibited an improvement of around 25.00% compared to the reference sample, showcasing superior performance than at the 6.24 kPa normal stress level. Figure 6.10(b) shows that the 16T sample reached a pullout resistance value of 40.58 kN/m. Upon examining the results under 10.56 kPa normal stress in Figure 6.10(c), both the 4T and 8T samples displayed nearly identical curves. Despite the anticipation of an increase with the additional elements, the primary reason for obtaining similar results in both 4T and 8T was the 4T sample achieving a higher pullout value than expected. The increment of the pullout resistance of 4T sample compared to the reference samples was 14.20%, 24.65%, and 41.48% at normal stresses of 6.24 kPa, 8.40 kPa, and 10.56 kPa, respectively. As evident from the percentage increases, the result under 10.56 kPa normal stress was higher than anticipated, potentially attributed to an experimental error. In experiments under 8.40 kPa and 10.56 kPa normal stresses, the 16T sample reached its maximum resistance after experiencing higher displacements compared to the others. Pullout resistance values increased with rising normal stresses. Moreover, augmenting the number of geomembrane barriers, which enhances soil-geogrid interaction, positively influenced pullout performance. The pullout increase achieved with the added elements compared to the reference samples ranged from 14.20% to 77.00%.

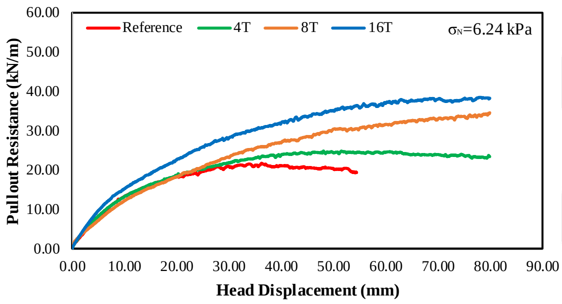

(a)

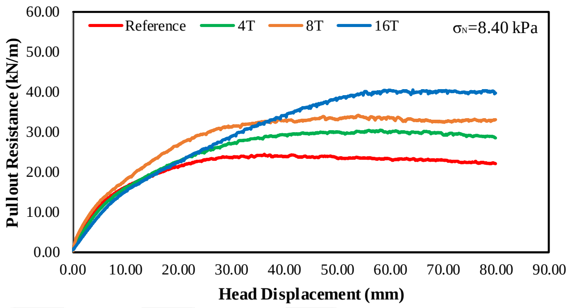

(b)

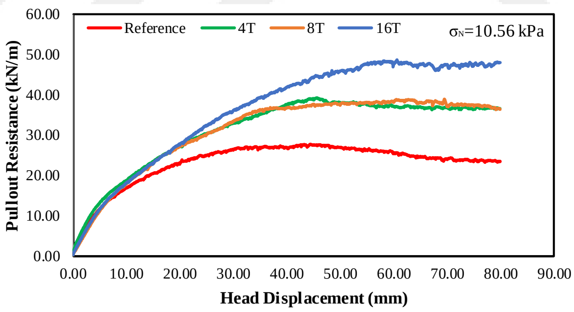

(c)

Figure 6.10. *The change in pullout resistance subjected to the normal pressure of; a) 6.24 kPa, b) 8.40 kPa, and c) 10.56 kPa*

In the study, strain values were taken from the longitudinal ribs under a normal stress of 10.56 kPa within the scope of identifying the elongation levels. It was understood that readings taken due to the placement of the strain gauges (SG) between the soil and geogrid were meaningful up to a certain point. Therefore, only significant data was shared in the graphs. Hence, focusing on the force-strain relationship rather than maximum strain values would be more reasonable. Two SGs were placed for each sample, except for the reference, with distances of 22.50 cm and 68.00 cm from the back of the geogrid. The SG close to the back of the geogrid was named SG-1, and the one farther away was named

SG-2. Although each sample normally had two SGs, in the reference sample, a SG was also placed between the first and second longitudinal ribs at the back, named SG-0. The results of the longitudinal rib located in the center of the reference sample are presented in Figure 6.11. In SG-0 and SG-2 readings, strains began to reveal themselves in the range of 5.00-7.50 kN/m pullout resistance, or around 2.00 mm head displacement. SG-0 strain values started to increase later compared to other reading points because strains began to mobilize from the front to the back due to the force applied from the front of the geogrid. Although SG-2 was expected to mobilize earlier than SG-1, due to potential difficulties during the experiment, such as the contact of a granular particle, SG-1 mobilized earlier than SG-2. When transverse ribs started to work, it created stress on the junction, which increased the strain value of the longitudinal rib. A significant strain increase was observed in SG-0 after being exposed to a pullout force of 23.00 kN/m which was about 2.00 cm displacement. As observed in the study of Pant et al. (2019), it can be concluded that the bearing resistance in the transverse ribs of the geogrid occurred after a 2.00 cm displacement.

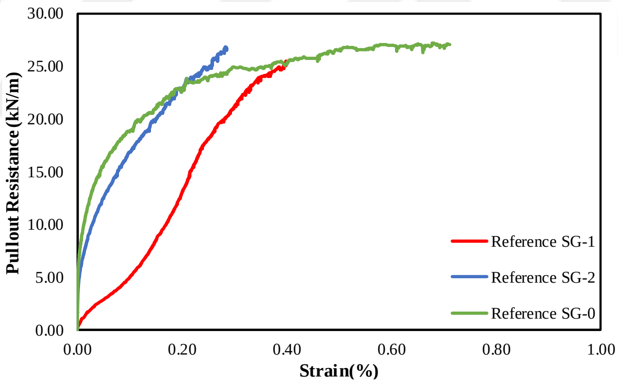

Figure 6.11. *Reference sample strains at a normal pressure of 10.56 kPa.*

It became apparent that both the 16T and 8T samples, after measuring strain values up to a certain point, likely lost contact with the geogrid surface, leading to an inability to record further measurements (Figure 6.12(a)). The perpendicular parts in the graph were attributed to this phenomenon. On the other hand, readings from SG-2, located at the front of the geogrid, provided more consistent results. In Figure 6.12(b), a comparison revealed that the reference sample demonstrated lower strain values at equivalent pullout resistance levels. This situation was primarily attributed to additional stresses on the transverse ribs due to additional transverse elements, resulting in extra strains. The extra stresses transferred from the junction to the geogrid longitudinal rib caused samples with transverse elements to reach higher strain values at equivalent pullout resistance levels.

The strain values for 4T and 16T were quite close. Although it was expected that 8T samples would exhibit higher strain values at the same force levels due to the greater number of added transverse elements in the 16T sample, the 8T samples actually reached higher strain values at equivalent force levels. In addition, the 16T sample had significant deformations, especially at the front, and even lost its connection with the junction of the transverse ribs (Figure 6.13). This occurrence may have resulted in the insufficient transfer of stresses from the transverse rib to the longitudinal rib, leading to lower-than-expected strain values. Figure 6.14, Figure 6.15, and Figure 6.16 further depicted significant deformations and rib failures in the 8T, 4T, and reference samples. However, in the sample with the highest number of geomembrane barriers, higher deformations were observed in the part where SG-2 took readings. Based on SG-1 data in Figure 6.12(a), at the same tensile force, the reference sample exhibited higher strain than the 4T sample. Strains mobilized quickly in the front ribs of the geogrid, while mobilization occurred later in the rear part. Initially, longitudinal ribs near the applied force started elongating, while those far from the force experienced delayed elongation. Due to the additional transverse elements, elongations may have concentrated in the front and transferred to the rear at lower levels.

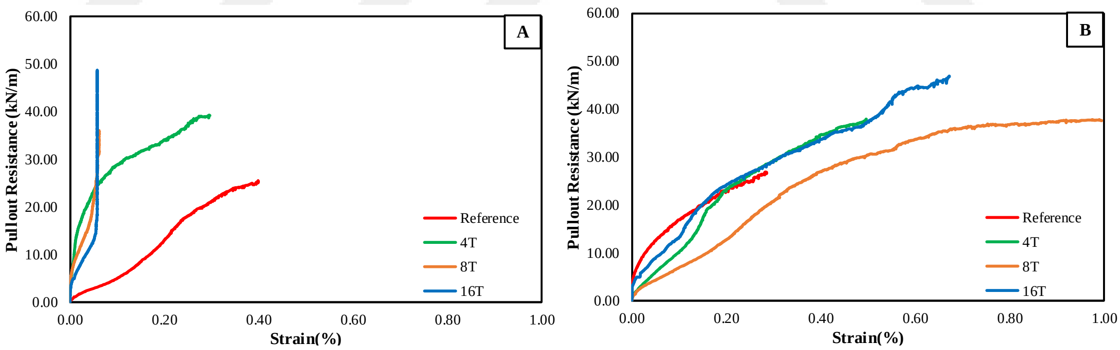

Figure 6.12. *The strain values: a) Rear of geogrid and b) Front of geogrid*

(a) (b)

Figure 6.13. *16T sample after applying a pullout test at normal pressure of 10.56 kPa a) Top view and b) Detailed view of the front side of deformed geogrid*


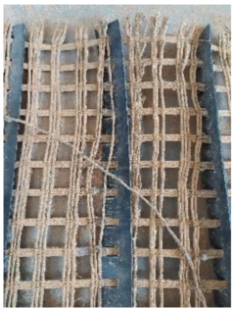

(a) (b)

Figure 6.14. *8T sample after applying a pullout test at normal pressure of 10.56 kPa a) Top view and b) Detailed view of the front side of deformed geogrid*


(a) (b)

Figure 6.15. *4T sample after applying a pullout test at normal pressure of 10.56 kPa a) Top view and b) Detailed view of the front side of deformed geogrid*


(a) (b)

Figure 6.16. *Reference sample after applying a pullout test at normal pressure of 10.56 kPa a) Top view and b) Detailed view of the front side of deformed geogrid*

In relation to the thickness of the transverse ribs, the height of the geomembrane barriers was considerably higher. Therefore, the soil mass applying passive resistance to the geomembrane barrier during pullout was also substantial. So, as a result of the movement caused by pullout, a portion of the soil moved together with the geomembrane barriers. Figure 6.17 illustrates the cracks that emerged as a consequence of this displacement, primarily occurring in the rear section of the soil within the pullout test setup. These cracks were observed in almost all samples containing geomembrane barriers. While deformations in the transverse ribs were noticeable in the reference samples at various normal pressures, the addition of transverse elements led to a frequent occurrence of detachment of transverse ribs from the junction (Figure 6.18). Fortifying the strength of the junction points could mitigate these detachments, thereby enabling the attainment of higher pullout resistance values.

(a) (b)

Figure 6.17. *The view of the soil surface after pullout test of a) 4T at 6.24 kPa and b) 16T at 8.40 kPa*

(a) (b)

Figure 6.18. *The ribs lost connection with junction a) Front and b) Rear of geogrid*

7. COST ANALYSIS

The unit prices of the geogrid and geomembrane used in this study were 2.19 USD and 3.00 USD per square meter, respectively. The upper surface of the geomembrane was considered as a whole without considering the gaps created in the geomembranes. Additionally, the cost of a staple was included in the calculation at a rate of 0.00033 USD per staple wire. The cost calculation only took into account the material cost used; therefore, labor was not included in this calculation (Table 7.1). Equations(7.1), (7.2), and (7.3) were employed to assess various aspects of the geomembrane barrier-containing samples in relation to the reference sample. Specifically, Equation(7.1) was utilized to calculate the cost increase percentage (C), while Equation(7.2) was applied to determine the improvement ratios in pullout resistance (PIR) compared to the reference sample. In addition, Equation(7.3) provided the pullout resistance improvement ratio based on the cost increase percentage (PIRC). As shown in Figure 7.1, PIRC values varied in the range of 53.81-157.24%. The 8T sample stood out at low normal stress magnitudes, while the 4T sample was prominent at high normal stresses. Many of the geomembrane barrier-containing samples did not provide the expected economic contribution. However, when faced with pullout problems and limited backfill clearance, the use of geogrids containing geomembrane barriers proved to be economically beneficial compared to opting for a different improvement method. Additionally, the use of geomembrane barriers, resulting in a reduction in the length of the geogrid, can lead to potential cost savings in backfill materials by decreasing the required width of the backfill. Furthermore, the production of geogrid barriers using cheaper raw materials could be a subject of investigation for future studies.

Table 7.1. *Cost of 0.49 m^2 geogrid samples*

Sample Name	Cost (USD)
Reference	1.07
4T	1.36
8T	1.64
16T	2.21

$$C = \left(\frac{Cost\ of\ geogrid\ sample\ with\ barrier}{Cost\ of\ reference\ sample} * 100\right) - 100 \tag{7.1}$$

$$PIR = \left(\frac{P_R \; of \;\; geogrid \; sample \; with \; barrier}{P_R \; of \; reference \; sample} * 100\right) - 100 \tag{7.2}$$

$$PIRC = \frac{PIR}{C} * 100 \tag{7.3}$$

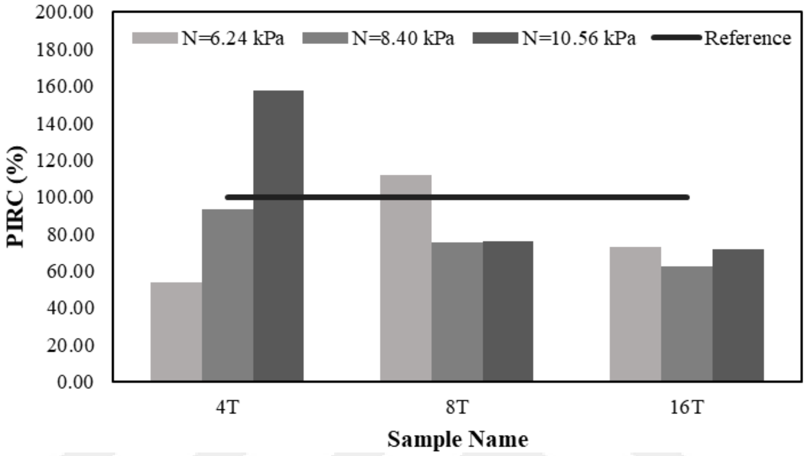

Figure 7.1. *The PIRC ratios of geogrid samples at various normal stresses*

8. LOAD BEARING TEST

One of the purposes of the study was to evaluate the impact of the geomembrane barriers used in the MSE wall constructed at a 1/4 scale through load-bearing tests. For this purpose, four experiments were conducted, namely reference, 4T, 8T, and 16T.

8.1. Load Bearing Test Setup

The experimental tests were conducted within a steel box with inner dimensions measuring 1500.00 mm * 1500.00 mm * 1500.00 mm. The front side of the apparatus was equipped with detachable steel profiles, enabling the opening and closing of the frontal section. To prevent direct contact between the bottom of the constructed MSE wall for the experiment and the steel test box as well as to ensure more realistic boundary conditions, a 75.00 mm high layer of sandy soil was situated at the bottom of the experimental setup according to Doger and Hatami (2020). The composition of this layer involved mixing and compacting 75.00% silica sand and 25.00% kaolinite clay at the optimal water content, classifying it as silty sand (SM) based on the Unified Soil Classification System (USCS). The soil layer's maximum dry unit weight and optimum water content were 20.70 kN/m³ and 11.67%, respectively. Furthermore, it exhibited a friction angle of 35.40° and a cohesion of 41.40 kPa. The compaction process of clay and sand in the test setup is visually represented in Figure 8.1, with areas inaccessible to the soil vibration plate compactor being compacted using the compaction hammer (Figure 8.1(c)).

(a) (b) (c)

Figure 8.1. *75.00 mm thick SM layer; a) Mixing, and compaction with b) soil vibration plate compactor, and c) compaction hammer*

The construction of the MSE wall involved placing modular blocks on the 75.00 mm thick sand layer. With the box width at 1500.00 mm, three modular blocks of 400.00 mm width each fit precisely, requiring the fourth block to be trimmed. As depicted in

Figure 8.2, the width of the modular block was reduced to 265.00 mm through the cutting process. Despite the expected dimension being 300.00 mm, an extra 35.00 mm was trimmed to accommodate potential gaps where modular blocks were locked. Furthermore, creating a small clearance between the steel box's side surfaces and the modular blocks aimed to prevent direct contact.

Figure 8.2. *Cutting process of modular block*

In next step, steel screws were used to secure the geogrid to the modular block, allowing them to move together under vertical load, similar to the approach by Zhang et al. (2022). Pegs (Figure 8.3(b)) were driven into predrilled holes. Small screws were then mounted into the pegs using a cordless drill. Since these mounted screws would hold the transverse ribs of the geogrid, they protruded approximately 5.00 mm above the modular block level (Figure 8.3(c)). To avoid causing an inclination in the modular blocks placed on top of the screwed modular block, locations for the screws on the lower parts of the blocks were identified, and the necessary holes were drilled at the bottom of the other modular block. The modular blocks were numbered to ensure the same arrangement was used for each experiment, as seen in Figure 8.4.

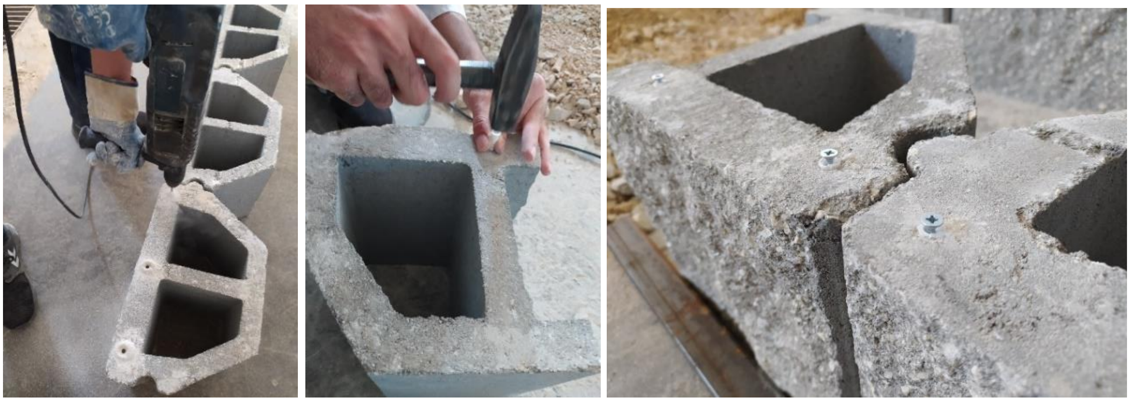

(a) (b) (c)

Figure 8.3. *a) Drilling with a drill, b) Embedding anchors, and c) Placing screws in modular blocks*

Figure 8.4. *Numbered modular blocks*

Facing displacement measurements were conducted using hangers, as employed in Hatami and Doger's study (2021). Hangers were utilized, and a thin EPS was inserted between the hangers and the modular block for screwing using a cordless drill (Figure 8.5(a)). The finalized installation of hangers mounted in the middle of the modular blocks is presented in Figure 8.5(b). Facing displacements transferred via hangers were measured using LVDTs mounted on steel profiles fixed with bolts on the front surface of the test box. Figure 8.5(c) shows the completed system for measuring facing displacement. Additionally, the points where displacement measurements were taken are indicated on the two-dimensional drawing in Figure 8.8, including the names of the LVDTs. The measurement capacity of the LVDTs used to measure facing displacement was 50.00 mm.

(a) (b) (c)

Figure 8.5. *a) Installation process of hangers, b) Installed hangers, c) and d) Hangers and LVDTs*

In the Figure 8.12, a 1.00 m high MSE wall was constructed by stacking four rows of modular blocks on top of each other. Zhang et al. (2022) stated that MSE walls designed for the bridge approach were 4.80 m. Accordingly, the scaling factor in our study was approximately 1/5. A reference sample was used between the MSE wall and the SM soil layer and between the first and second modular blocks. Geogrids placed at heights of 500.00 mm and 750.00 mm varied according to the type of experiment, namely reference, 4T, 8T, and 16T. A strain gauge was placed at a distance of 620.00 mm from the edge of the geogrid away from the facing for the geogrid at a height of 500.00 mm. This strain gauge was named SG-1 and was placed on the longitudinal rib in the middle of the geogrid with a width of 1445.00 mm. This middle part was placed on the lower part of bonding because it corresponded to the part where bonding was performed. For the geogrid at a height of 750.00 mm, 4 SGs were placed. These SGs were named SG-2, SG-3, SG-4, and SG-5, respectively, moving from the edge far from the facing towards the facing. According to the distance from the edge far from the facing, SG-2, SG-3, SG-4, and SG-5 were 60.00 mm, 340.00 mm, 620.00 mm, and 900.00 mm, respectively. In this geogrid, SG was glued to the middle longitudinal rib. Strain gauges attached to geogrids at heights of 500.00 mm and 750.00 mm (Figure 8.6).

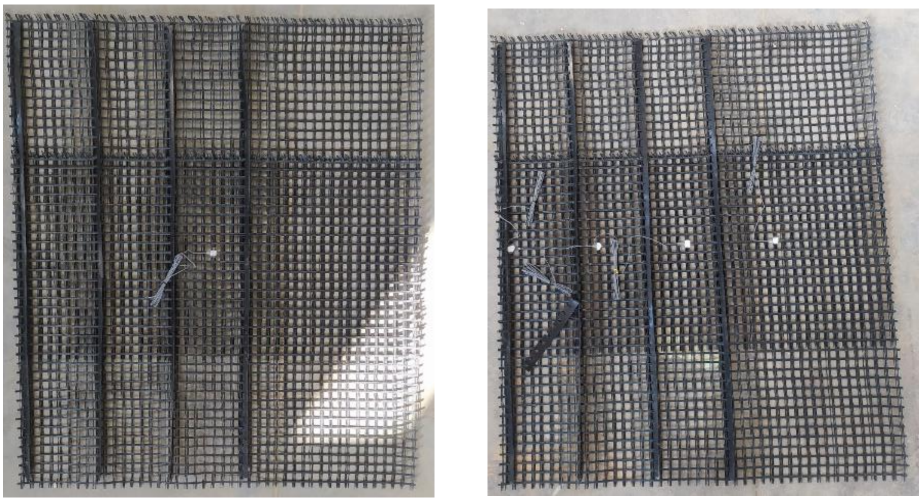

(a) (b)

Figure 8.6. *4T samples with SGs used at a) 500.00 mm height and b) 750.00 mm height*

An anticipated vertical force was generated through the hydraulic jack connected to the beam mounted on top of the box. To measure the force coming from the hydraulic jack and a load cell, 1000.00 kN capacity, was utilized. A loading beam was employed to transfer the load from the hydraulic jack to the MSE wall. This way, the MSE wall was subjected to strip loading procedure thanks to the H-cross-section beam, with a length of 1200.00 mm, had a depth of 240.00 mm and a width of 240.00 mm. Additionally, the web and flange thicknesses were 10.00 mm and 20.00 mm, respectively. According to Zhang et al.'s (2022) study, the distance between the back of the modular block and the loading beam was 8.00 cm. In this study with an MSE wall height of 2.75 m, this distance was 61.00 cm (Doger & Hatami, 2020). Based on these studies, the distance between the back of the facing and the loading beam was approximately 243.00 mm. Moreover, to prevent bending in the loading beam during the experiment, steel plates welded to the beam increased the flexural strength. Two LVDTs with a measurement capacity of 10.00 cm were used to examine the settling of the loading beam under vertical load. The upper part of the experimental setup where the vertical force was generated is shown in Figure 8.7(a). A data logger used in pullout tests was employed for data collection. Furthermore, the top-view photographs were taken using the setup during the experiment (Figure 8.7(b)).

(a) (b)

Figure 8.7. *a) Top side of the experimental setup and b) Facing displacement photography system*

The 2D drawing of the experimental setup is presented in Figure 8.8. In the figure, the red-colored geogrids varied based on the applied test type, while the green-colored geogrids represented the reference specimen. As shown in Figure 8.8, a 240.00 mm portion of the geogrids was located between the modular blocks. The distance between the back surface of the geogrid and the test setup was 90.00 mm. Additionally, GM-class soil with a compaction ratio of 91.15% was utilized as backfill.

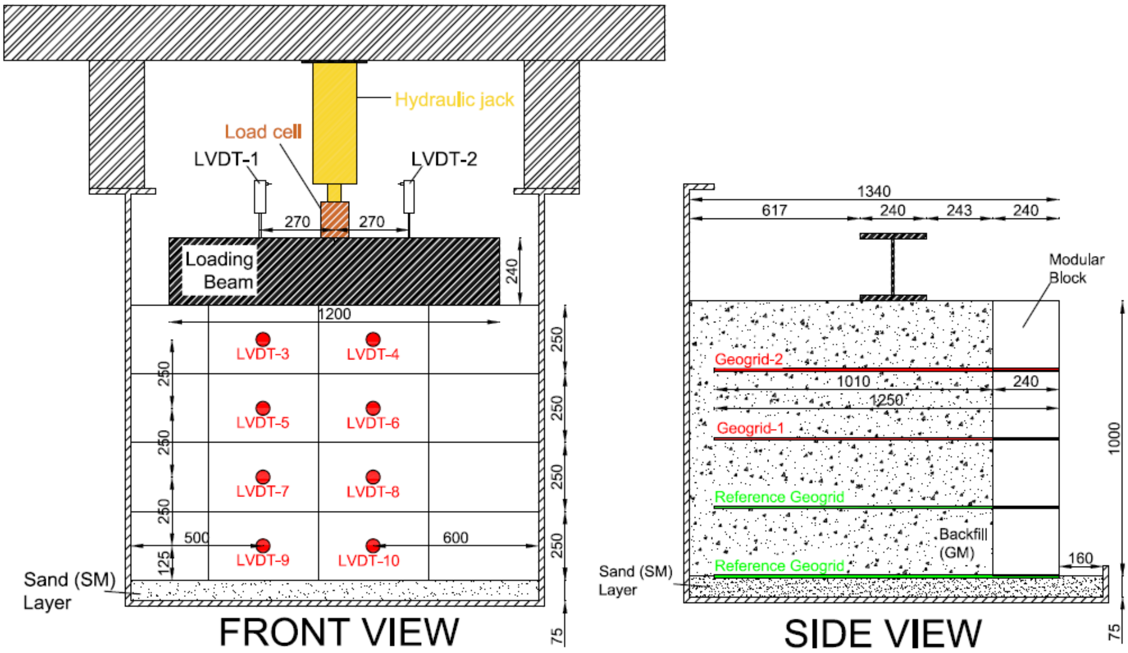

Figure 8.8. *Front and side view of load bearing test setup in mm*

8.2. Load Bearing Procedure

During the initial phase, the Reference geogrids were spread over a 75.00 mm-thick layer of sand. Following this, the first row of modular blocks was positioned 160.00 mm away from the front side of the test setup over the laid geogrid. A rectangular steel profile was used as a guide to eliminate the out of plane problem of wall (Figure 8.9(a)). Later, the GM class backfill material was placed until it reached the same level as the modular blocks, achieving a layer thickness of 250.00 mm. The voids within the modular blocks were also filled with soil. Similar to the study by Doger and Hatami (2020), the soil vibration plate compactor was strategically placed 45.00 cm away from the facing to prevent displacements during the initial construction phase. In sections where compaction was needed, a compaction hammer was utilized, concluding the compaction process for the entire layer with 5 blows for every uncompacted area (Figure 8.9(b)). The compaction ratio for the compacted soil stood at 91.15%.

(a) (b)

Figure 8.9. *a) Placement of modular blocks, and b) Compaction process with a compaction hammer.*

The first modular block was laid with a reference sample without a geomembrane barrier, and its transverse rib was fitted in front of the modular block's screws. Next, the second row of modular blocks was positioned above the laid geogrid, and the same soil placement process was repeated. Between the second and third rows of modular blocks, distinct samples—Reference, 4T, 8T, or 16T, contingent on the experiment—were used. Following uniform filling and compaction procedures, the chosen sample found its place above the 750.00 mm-high modular block. Special attention was given to ensure the vertical alignment of the geomembrane barriers on the placed geogrids. Figure 8.10(b) described the use of iron rods during soil filling to uphold the geogrids in a tensioning condition. Upon situating the fourth row of modular blocks atop the geogrid, the construction of the MSE wall finished with detailed filling and compaction processes

(Figure 8.10(c)). The first two rows consistently utilized a reference geogrid, while the upper two rows were designated for the samples under investigation. For instance, in experiments involving 8T, a reference sample was consistently positioned above the sand layer and at a height of 250.00 mm, while 8T samples were placed at heights of 500.00 mm and 750.00 mm, respectively.

(a) (b) (c)

Figure 8.10. *a) Filling process of the backfill material, b) Tensioning of the sample with the help of steel rods, and c) Constructed MSE wall*

The upper section of the completed MSE wall experimental arrangement was positioned onto the MSE wall and firmly fastened using bolts (Figure 8.11(a)). Additionally, the steel profiles housing LVDTs were securely attached to the front surface of the test box through bolts, ensuring proper contact between the hangers and LVDTs. The fully assembled experimental setup is shown in the Figure 8.12. The experiments were continued until reaching about 320.00 kN except reference sample because of unexpected experimental setup deformations were observed after 240.00 kN for mentioned one. After identifying partly fractures from welding point in the initial experiment, which was reference case, the affected areas were welded better to enhance the setup (Figure 8.11(b)). This improvement enabled the attainment of a vertical force of approximately 320.00 kN in subsequent experiments, which were 4T, 8T, and 16T. Average loading rate was about 3.00 mm/min according to beam settlement.

 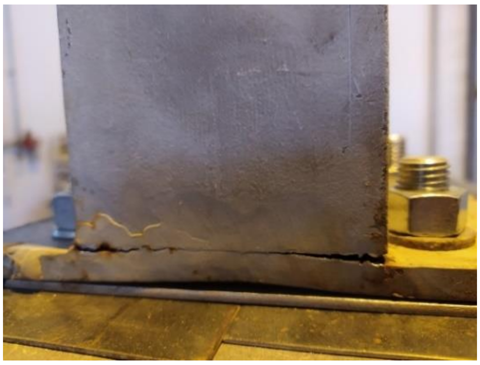

(a) (b)

Figure 8.11. *a) Placement of the upper part of the experimental setup, and b) Fractures from welding point occurring in the upper part of the experimental setup*

Figure 8.12. *Experimental setup ready to start the experiment*

8.3. Results and Discussions

In this section, the results obtained from the conducted load-bearing experiments were analyzed and compared in terms of the tensile strain of geogrids, facing displacements at various heights of the wall, vertical load- settlement.

8.3.1. Load settlement performance

The load-settlement performance was investigated for MSE walls at a height of 1.00 m using different geogrid samples. Since the experiments were halted before any failure occurrence due to the test setup, the graph in Figure 8.13 does not reach the maximum vertical stress values for MSE walls. Therefore, evaluating settlements at the specified stress magnitudes would be more accurate. According to FHWA, a maximum settlement of 0.50% of the wall height is allowed at the design stress of 190.00 kPa for bridge approaches. In other words, our settlement values should not exceed 5.00 mm under a vertical stress of 190.00 kPa. For walls using Reference, 4T, 8T, and 16T samples under 190.00 kPa vertical pressure, the footing settlements were 10.56 mm, 13.03 mm, 14.13 mm, and 15.17 mm, respectively. However, in Zhang et al.'s study, a scale factor of 1/4 was applied, resulting in the design stress being divided by 4. Taking this into account, with the scale factor in our study being 1/5, the design vertical stress magnitude was 38.00 kPa. The footing settlements for Reference, 4T, 8T, and 16T are 1.40 mm, 2.49 mm, 3.43 mm, and 2.63 mm at 38.00 kPa, respectively. Notably, these settlement magnitudes remain below 5.00 mm, ensuring compliance with FHWA standards for allowable settlement.

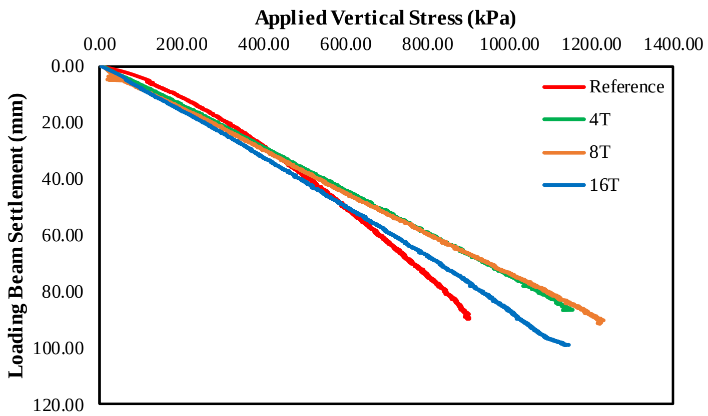

Figure 8.13. *The change in surface settlement under applied vertical stress*

The MSE wall utilizing the reference sample demonstrated the least settlements until stress magnitudes of 400 kPa (Figure 8.13). However, beyond 400 kPa, walls constructed with the 4T and 8T samples exhibited diminished settlements according to reference case. Notably, after reaching the 600.00 kPa threshold, walls prepared with the 16T sample displayed settlement values lower than the reference sample. This underscored the evolving role of geomembrane barriers in settlement behavior, with their contribution becoming more pronounced as vertical pressure increased. At the maximum of vertical stress reached up to 900.00 kPa for reference sample, the settlements of the 4T, 8T, and 16T samples experienced reductions of 32.03%, 32.77%, and 15.23% according to reference one, respectively. This finding emphasized that additional transverse elements contribute not only to pullout resistance but also to the strength of the reinforced soil. Due to the presence of geomembrane barriers, interaction with a greater mass of soil occurred. In addition to the mass of the soil, the barriers created an additional confinement through their heights exceeding the thickness of geogrid ribs. As a result, an increase in strength was observed in the reinforced soil. Additionally, it was considered that the extra confinement contributed to a more homogeneous distribution of vertical stresses. While the load-settlement performances of the 4T and 8T samples exhibited similarities, the performance of the 16T sample lagged behind. It is conceivable that experiments reaching higher vertical stresses may reveal an enhancement in the performance of the 16T sample.

8.3.2. Facing displacements

Figure 8.14 presented displacements corresponding to different heights of the wall. These values were computed by averaging the measurements from two LVDTs at each height level. For instance, in Figure 8.14(b) (h=62.5), the values were derived by plotting a graph based on the average data obtained from LVDT 5 and LVDT 6. In the Figure 8.14(a), Despite the reference sample displaying lower facing displacements than others up to 450.00 kPa, samples incorporating additional transverse elements demonstrated superior performance at higher stress magnitudes, particularly beyond 450.00 kPa. As the activation of transverse elements necessitates a specific displacement, the reference sample exhibited more effective performance at lower stresses. Considering the slope of the reference sample for a wall height of 62.5 cm (Figure 8.14(b)), it became apparent that it would reach higher facing displacement values than samples with geomembrane barriers after approximately 1150.00 kPa. Furthermore, when studying the 4T, 8T, and 16T samples, the initiation of bearing resistance due to geomembrane barriers was assessed by examining the graph slopes after approximately 10.00 mm displacement. Facing displacements can be likened to head displacement in geogrid pullout tests, as they move in together due to the screws integrated into the modular blocks. Figure 8.14(c) and Figure 8.14(d) were constructed using data collected from the lower sections of the wall, resulting in notably lower and closely clustered displacement values. Overall, the impact of geomembrane barriers on pullout resistance became evident at elevated stress magnitudes, as a specific displacement was required for their effectiveness.

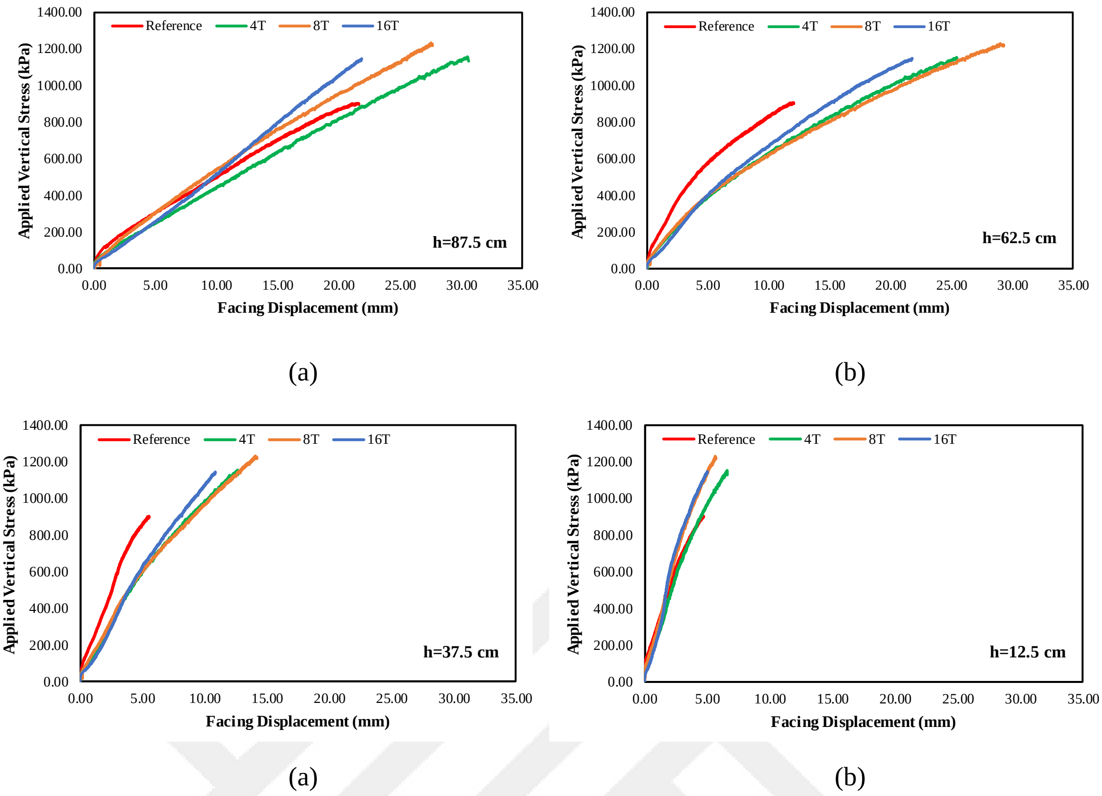

Figure 8.14. *The change in facing displacement values according to vertical stress at various height of the wall; a) 87.50 cm, b) 62.5 cm, c) 37.5 cm and d) 12.5 cm*

According to FHWA guideline, facing displacements should not exceed 1.00% of the wall height under a design stress of 190.00 kPa. Considering our MSE wall height of 1000.00 mm, facing displacements were supposed to not exceed 10.00 mm. Under 190.00 kPa, the maximum facing displacements for Reference, 4T, 8T, and 16T were 2.34 mm, 3.47 mm, 2.67 mm, and 3.62 mm, respectively (Figure 8.15). Since displacements were below 10.00 mm, the constructed walls complied with FHWA guideline in terms of facing settlement. While the assessment technically should have been based on the 38.00 kPa corresponding to a 1/5 scale factor, it was unnecessary to evaluate at 38.00 kPa since the allowable facing displacement was not exceeded under 190.00 kPa. With increasing vertical stress, wall displacements also increased. When comparing the graph of displacements for the wall constructed using the Reference geogrid (Figure 8.15(a)) with those for samples containing geomembrane barriers (Figure 8.15(b), (c), and (d)), a notable difference in displacement behavior at heights of 62.50 cm and 87.5 cm was observed with rising vertical stresses. Facing displacement increased significantly in the reference sample as one proceeded from the bottom to the top of the wall, but it increased much less in the samples with geomembrane barriers than in the reference. This behaviour was particularly pronounced at high vertical stress levels. Additionally, it should be noted that samples containing additional transverse elements were located at heights of 50.00 cm and 75.00 cm. At 900.00 kPa vertical stress, for the elevation 87.5 cm on the wall, compared to the displacement of the modular block below (relative displacement), the displacement for reference, 4T, 8T, and 16T increased by 79.94%, 32.27%, 4.71%, and 12.72%, respectively. This result indicated a significant effect of the geomembrane barrier in reducing facing displacement. While the 4T sample may not have performed as well as 8T and 16T, it had nearly halved the relative displacement ratio compared to the reference at the top modular blocks. The 8T and 16T samples demonstrated highly successful performance, proving the effectiveness of geogrid barriers, with the 8T sample particularly excelling in relative facing displacement. Additionally, geomembrane barriers clearly demonstrated their impact on relative modular block displacement from the vertical stress level of 400.00 onwards.

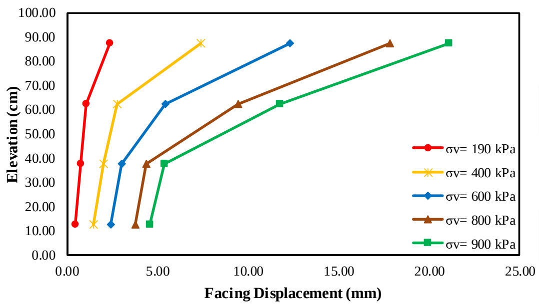

(a)

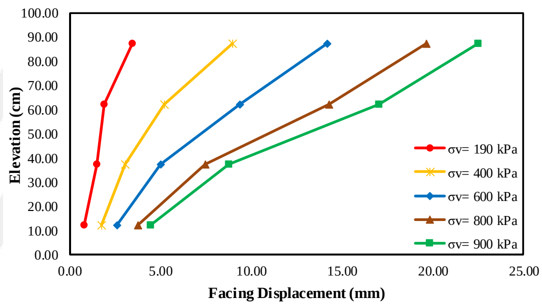

(b)

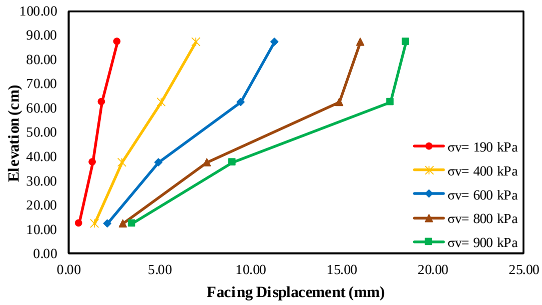

(a)

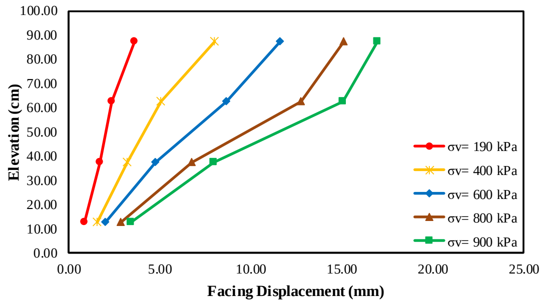

(b)

Figure 8.15. *Facing displacements at various elevations of the MSE wall under specific stress magnitudes: a) Reference, b) 4T, c) 8T, d) 16T*

The photographs depicting the start and finish of the 8T sample test, showing facing displacement, are provided in Figure 8.16.

(a)

(b)

Figure 8.16. *Top view of facing displacement of 8T at a) Initial and b) End of the load bearing test*

8.3.3. Strain behaviour of geogrids

Strain gauges (SGs) were strategically positioned at different locations along the geogrids. Specifically, at the height of 500.00 mm, SGs were exclusively placed to align with the loading beam, while SGs were distributed across four distinct locations on the geogrid at a height of 750.00 mm (Figure 8.17). The strain gauge situated on the geogrid at a height of 500.00 mm was denoted as SG1.

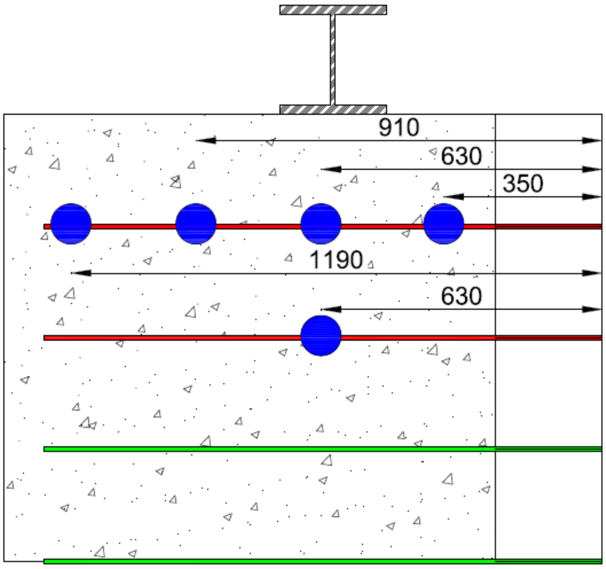

Figure 8.17. *The locations of strain gauges*

Axial strain values at different positions of the geogrid specimens are given in Figure 8.18. Positive strain values indicate longitudinal elongation, while negative values signify shortening. Figure 8.18(c) and Figure 8.18 (d) show negative strain values for the 16T specimens. Despite not expecting any contraction in geogrids, strain gauges (SGs) located at the furthest point from the loading beam suggest shortening. Although no shortening was anticipated in the geogrid, this could be attributed to the pushout region as discussed in Derksen et al.'s study. In the indirectly active geogrid, regions farther from the loading point may experience greater soil displacement compared to geogrid displacement. In these pushout regions, the geogrid transverse rib creates a reverse bearing resistance. As observed in the graphs, the prevalence of this phenomenon in the 16T sample could be due to its higher inclusion of geomembrane barriers, enhancing bearing resistance in the pushout region. It is also possible that the contact of SGs in the 16T sample with granular soil particles led to inaccurate measurements. In Figure 8.18(b), where geogrids aligned with the loading beam were provided, data from SG1 at a height of 500.00 mm are represented by a dashed line. Although strain behaviors were quite similar for geogrid specimens at heights of 500.00 mm and 750.00 mm, the longitudinal rib at 750.00 mm, exposed to higher incremental stress, exhibits greater elongation. Additionally, the region located directly beneath the loading beam, at a distance of 630.00 mm from the facing, had significantly higher axial strain values compared to other SG measurements. This is attributed to the indirectly active geogrid being in the interlocking region, where substantial confinement effects occur, leading to high stresses and substantial deformations in geogrid ribs. In Figure 8.18(a), the location where SG is positioned at a distance of 350.00 mm from the facing was presumed to be in the pullout region. Furthermore, axial strain values at 910.00 and 1190.00 were quite small. Overall, indirectly active geogrid regions became more pronounced with the presence of geomembrane barriers. Moreover, meaningful data were not obtained from the 4T sample in Visual 2(a) and the 8T sample in Visual 2(b), and therefore, they are not included in the graphs.

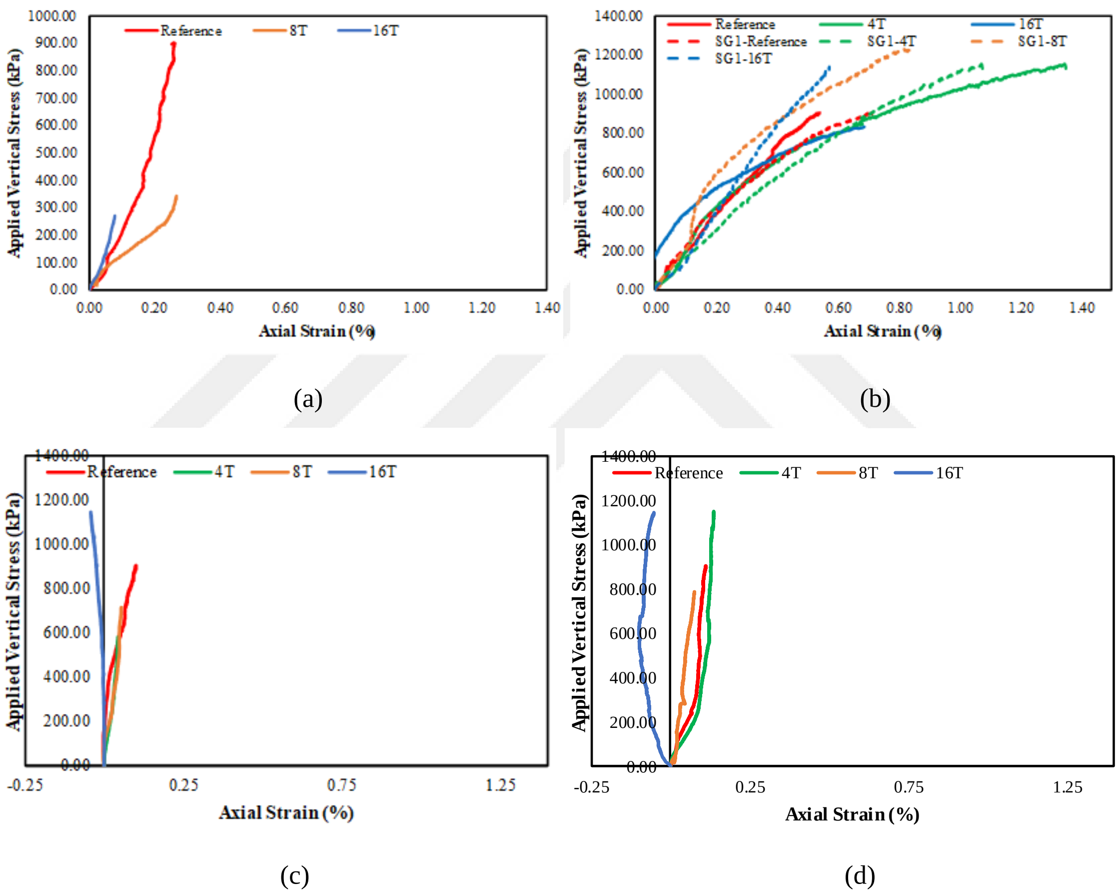

Figure 8.18. *The change in axial strains taken from different dimensions of geogrid according to facing; a) 35.00 cm, b) 63.00 cm, c) 91.00 cm, and d) 119.00 cm*

Figure 8.19 presented variations in axial strain at different distances from the facing for various vertical stresses applied to the geogrid specimens. Notably, the graphs exclusively focused on strain increases, and data for contraction in the longitudinal rib were omitted. Furthermore, data points with inconclusive results were not incorporated into the graphs. In compliance with FHWA guidelines, the specimens did not exceed a tensile strain of 2.00% under a design stress of 190.00 kPa. As our specimens exhibited axial strains below 0.20%, they remained within the allowable strain limits set by FHWA.

A visible increase in axial strain was observed at a distance of 63.00 cm from the facing for the reference specimen, aligning with the loading beam (Figure 8.19(a)). In the case of graphs featuring the 4T, 8T, and 16T specimens (Figure 8.19(b), Figure 8.19(c), Figure 8.19(d)), the axial strain increases tended to concentrate in proximity to the facing, resembling the behavior observed in pullout tests. Additionally, due to the absence of meaningful data from the 8T sample at a distance of 63.00 cm, data from SG1 were utilized.

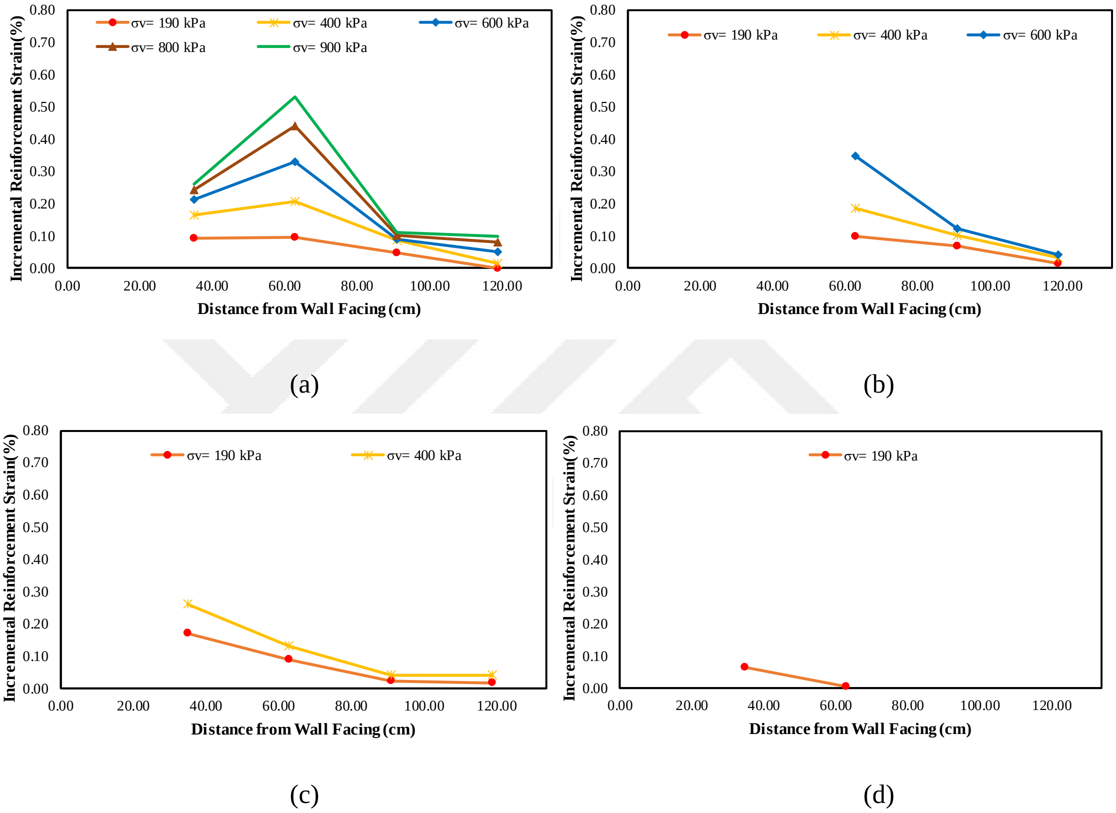

Figure 8.19. *Strain distributions of geogrid specimens: a) Reference, b) 4T, c) 8T, and d) 16T*

9. CONCLUSION

In this study, the performance of geomembrane barriers placed perpendicular to the front of the geogrid transverse rib was investigated through pullout tests and load-bearing tests. Besides, the effect of geomembrane barrier spacing was examined by placing them at intervals of two, four, and eight geogrid transverse ribs.

- Geomembrane barriers were demonstrated to enhance pullout resistance in the range of 14.20% to 77.00%, by increasing the bearing resistance that is a constituent of pullout resistance. The contribution to pullout resistance increased as the spacing of geogrid barriers decreased.
- During the pullout motion, bearing resistance emerged in the transverse elements after an approximate displacement of 2.00 cm. Tensile strains in the geogrid's longitudinal rib rapidly mobilized on the side where the pullout force was applied, although maintains significantly lower levels on the rear side of the geogrid. The inclusion of geomembrane barriers highlighted elongations, primarily concentrating on the front section of the geogrid.
- Certain transverse fibers detached from the junction due to the presence of geomembrane barriers during the pullout. The strengthening of the geogrid junctions is recommended to achieve a more effective enhancement when utilizing geomembrane barriers.
- In cases where the back clearance of the mechanically stabilized earth wall is limited, geomembrane barrier-containing geogrids can be employed. Additionally, the use of barriers enables sufficient pullout resistance with a shorter geogrid length, thereby resulting in potential savings on backfill material.
- Geogrid barriers contributed not only to the pullout but also to the bearing capacity of the soil. Reductions in settlements were observed up to a value of 32.80%, and the use of an every eight-rib geomembrane barrier proved to be highly effective. In addition, the contribution of the added barriers became apparent after a vertical stress of 40.00 kPa.
- In the MSE wall, facing displacements increased as one moved upward from the bottom to the top of the wall. The relative displacements made by the wall under the top modular block in comparison to the one beneath it were 79.94% and 4.71% for the geogrid without geomembrane barriers and

geogrid with every eight rib geomembrane barrier samples, respectively. The additional pullout resistance obtained through the inclusion of geomembrane barriers minimized the relative displacements in the facing.

- The significant elongations observed in the regions where vertical stress was applied to the geogrid indicated a high confinement effect. This region could be described as the interlocking region observed in the indirectly active geogrid. On the other hand, in the portions of the geogrid distant from the facing, a pushout region formed where the soil underwent greater displacement compared to the geogrid. In samples where geomembranes were used, the regions of the indirectly active geogrid were more clearly observed.

REFERENCES

Abdi, M. R., & Mirzaeifar, H. (2017). Experimental and PIV evaluation of grain size and distribution on soil–geogrid interactions in pullout test. *Soils and Foundations*, 57(6), 1045–1058.

Abdi, M. R., Mirzaeifar, H., & Asgardun, Y. (2022). Novel soil-pegged geogrid (PG) interactions in pull-out loading conditions. *Geotextiles and Geomembranes*, 50(4), 764–778.

Abdi, M. R., & Zandieh, A. R. (2014). Experimental and numerical analysis of large scale pull out tests conducted on clays reinforced with geogrids encapsulated with coarse material. *Geotextiles and Geomembranes*, 42(5), 494–504.

Altay, G., Kayadelen, C., Taşkıran, T., & Kaya, Y. Z. (2019). A laboratory study on pull-out resistance of geogrid in clay soil. *Measurement*, 139, 301–307.

ASTM D698-12. (2014). *Standard Test Methods for Laboratory Compaction Characteristics of Soil Using Standard Effort (12 400 ft-lbf/ft3 (600 kN-m/m3))*.

ASTM D854-14. (2023). *Standard Test Methods for Specific Gravity of Soil Solids by Water Pycnometer*.

ASTM D1556/D1556M-15e1. (2016). *Standard Test Method for Density and Unit Weight of Soil in Place by Sand-Cone Method*.

ASTM D3080/D3080M − 23. (n.d.). *Standard Test Method for Direct Shear Test of Soils Under Consolidated Drained Conditions*.

ASTM D4318-17. (2018). *Standard Test Methods for Liquid Limit, Plastic Limit, and Plasticity Index of Soils*.

ASTM D6637-11. (2015). *Standard Test Method for Determining Tensile Properties of Geogrids by the Single or Multi-Rib Tensile Method*.

ASTM D6913/D6913M-17. (2021). *Standard Test Methods for Particle-Size Distribution (Gradation) of Soils Using Sieve Analysis*.

ASTM D7928-21e1. (2021). *Standard Test Method for Particle-Size Distribution (Gradation) of Fine-Grained Soils Using the Sedimentation (Hydrometer) Analysis*.

ASTM Standard D2487-17. (2020). *Standard Practice for Classification of Soils for Engineering Purposes (Unified Soil Classification System)*.

ASTM Standard D6706-01. (2021). *Standard Test Method for Measuring Geosynthetic Pullout Resistance in Soil*.

Bagli, S. P. (2022). A Tryst with Geosynthetics. *Indian Geotechnical Journal*, 52(5), 1003–1053.

Berg, R., Christopher, B., & Samtani, N. (2009). *Design of Mechanically Stabilized Earth Walls and Reinforced Soil Slopes—Volume 1*. Washington: Federal Highway Administration

Biabani, M. M., Ngo, N. T., & Indraratna, B. (2016). Performance evaluation of railway subballast stabilised with geocell based on pull-out testing. *Geotextiles and Geomembranes*, 44(4), 579–591.

Bilgin, Ö. (2009). Failure mechanisms governing reinforcement length of geogrid reinforced soil retaining walls. *Engineering Structures*, 31(9), 1967–1975.

Bouazza, A. (2002). Geosynthetic clay liners. *Geotextiles and Geomembranes,* 20(1), 3–17.

Briançon, L., Girard, H., & Gourc, J. P. (2011). A new procedure for measuring geosynthetic friction with an inclined plane. *Geotextiles and Geomembranes*, 29(5), 472–482.

Cardile, G., Gioffrè, D., Moraci, N., & Calvarano, L. S. (2017). Modelling interference between the geogrid bearing members under pullout loading conditions. *Geotextiles and Geomembranes*, 45(3), 169–177.

Cazzuffi, D., Moraci, N., Calvarano, L., Cardile, G., Gioffrè, D., & Recalcati, P. (2014). The influence of vertical effective stress and geogrid length on interface behavior under pullout conditions. *Geosynthetics*, 32(2), 40–50.

Chen, R.-H., Liu, C.-N., Chen, K.-S., & Chen, T.-J. (2000). Analysis of a reinforced slope failure induced by The Chi-Chi (Taiwan) earthquake. *Journal of the Chinese Institute of Engineers*, 23(4), 429–437.

Collin, J. G. (2001). Lessons learned from a segmental retaining wall failure. *Geotextiles and Geomembranes*, 19(7), 445–454.

Derksen, J., Ziegler, M., & Fuentes, R. (2021). Geogrid-soil interaction: A new conceptual model and testing apparatus. *Geotextiles and Geomembranes*, 49(5), 1393–1406.

Dickinson, S., Brachman, R. W. I., & Rowe, R. K. (2010). Thickness and Hydraulic Performance of Geosynthetic Clay Liners Overlying a Geonet. *Journal of Geotechnical and Geoenvironmental Engineering*, 136(4), 552–561.

Doger, R., & Hatami, K. (2020). Influence of Facing on the Performance of GRS Bridge Abutments. *International Journal of Geosynthetics and Ground Engineering*, 6, 1–14.

Emir, A. S. (2005). *Donatılı Zemin İstinat Duvarlarının Statik Ve Dinamik Yüklere Göre Tasarımı* [M.Sc.]. İstanbul: İstanbul Technical University, Institute of Graduate Education.

EN ISO Standard 10319. (2015). *ISO 10319:2015 - Geosynthetics — Wide-width tensile test*.

Esfandiari, J., & Selamat, M. R. (2012). Laboratory investigation on the effect of transverse member on pull out capacity of metal strip reinforcement in sand. *Geotextiles and Geomembranes*, 35, 41–49.

Evirgen, B., Buyuk, B., Cil, G. T., & Deger, T. (2021). Experimental Performance of Polyester-Fiber-Based Soil Geogrids against Reflective Cracks. *Transportation Research Record*, 2675(12), 53–64.

Federal Highway Administration. (2011). *Geosynthetic Reinforced Soil Integrated Bridge System Synthesis*. Washington: FHWA

Gamski, K. (1984). Geomembranes: Classification, use and performance. *Geotextiles and Geomembranes*, 1(2), 85–117.

General Directorate of Highways of the Türkiye. (2013). *Karayolları Teknik Şartnamesi*. Ankara: Highway Technical Specifications.

Gültekin, A. A., & Evirgen, B. (2021). The Effect of Various Fences on the Geogrid Performance. *6th International Mediterranean Science and Engineering Congress (IMSEC 2021),* Antalya: Lonicera Hotel, 726–730.

Han, B., Ling, J., Shu, X., Gong, H., & Huang, B. (2018). Laboratory investigation of particle size effects on the shear behavior of aggregate-geogrid interface. *Construction and Building Materials*, 158, 1015–1025.

Han, J. G., Lee, K. W., Lee, J. Y., Hong, G., & Park, J. (2021). Experimental Study on the Pullout Resistance of Smooth Steel Strip Reinforcement with Transverse Members. *Applied Sciences*, 11(6), 2776.

Hatami, K., & Doger, R. (2021). Load-bearing performance of model GRS bridge abutments with different facing and reinforcement spacing configurations. *Geotextiles and Geomembranes*, 49(5), 1139–1148.

Holtz, R. D. (2004). Geosynthetics R&D-The 'Early'Days (1960s to Circa 1985). *In Proceedings from the 2004 Symposium Honouring the Research Achievements of Dr. Robert M. Koerner*.

Jewell, R. A. (1985). Material properties for the design of geotextile reinforced slopes. *Geotextiles and Geomembranes*, 2(2), 83–109.

Kayadelen, C., Önal, T. Ö., & Altay, G. (2018). Experimental study on pull-out response of geogrid embedded in sand. *Measurement*, 117, 390–396.

Khushefati, W. H., Ahmed, N. U., & Alim, M. A. (2015). Review on the Potential Applications of Geofoam Material in Saudi Arabia for Highways and Building Construction. *JKAU: Eng. Sci*, 26(2), 23–47.

Koerner, R. M. (2016). *Designing with Geosynthetics - 6Th Edition Vol. 1*.

Kong, D. J., Wu, H. N., Chai, J. C., & Arulrajah, A. (2017). State-Of-The-Art Review of Geosynthetic Clay Liners. *Sustainability*, 9(11), 2110.

Lajevardi, S. H., Briançon, L., & Dias, D. (2014). Experimental studies of the geosynthetic anchorage – Effect of geometric parameters and efficiency of anchorages. *Geotextiles and Geomembranes,* 42(5), 505–514.

Lavoie, F. L., Valentin, C. A., Kobelnik, M., da Silva, J. L., & Lopes, M. de L. (2020). HDPE Geomembranes for Environmental Protection: Two Case Studies. *Sustainability*, 12(20), 8682.

Lawrence, C. A. (2014). High performance textiles for geotechnical engineering: geotextiles and related materials. In *High Performance Textiles and Their Applications* (pp. 256–350). Cambridge: Woodhead Publishing.

Ling, H., Leshchinsky, D., & Chou, N. N. S. (2001). Post-earthquake investigation on several geosynthetic-reinforced soil retaining walls and slopes during the Ji-Ji earthquake of Taiwan. *Soil Dynamics and Earthquake Engineering*, 21(4), 297–313.

Liu, C.-N., Yang, K.-H., Ho, Y.-H., & Chang, C.-M. (2012). Lessons learned from three failures on a high steep geogrid-reinforced slope. *Geotextiles and Geomembranes*, 34, 429–437.

Mirzaalimohammadi, A., Ghazavi, M., Roustaei, M., & Lajevardi, S. H. (2019). Pullout response of strengthened geosynthetic interacting with fine sand. *Geotextiles and Geomembranes*, 47(4), 530–541.

Mittal, A. (2018). Geosynthetics : An Overview. *IJSRSET*, *4*(4), 231–238.

Moraci, N., Sarah, C. L., Cardile, G., Cazzuffi, D., Calvarano, L. S., Gioffrè, D., & Recalcati, P. (2014). European experience in pullout tests: The influence of soil type on interface behavior under pullout conditions. *Geosynthetics*, 42–50.

Mosallanezhad, M., Alfaro, M. C., Hataf, N., & Sadat Taghavi, S. H. (2016). Performance of the new reinforcement system in the increase of shear strength of typical geogrid interface with soil. *Geotextiles and Geomembranes*, 44(3), 457–462.

Narejo, D., Li, M., Zimmel, E., & Wu, Y. (2013). A monolithic layered nonwoven–woven geotextile for use with drainage geocomposites in coal combustion residual projects. *Geotextiles and Geomembranes*, 37, 16–22.

Pant, A., Datta, M., Ramana, G. V., & Bansal, D. (2019). Measurement of role of transverse and longitudinal members on pullout resistance of PET geogrid. *Measurement*, 148, 106944.

Puppala, A. J., Ruttanaporamakul, P., & Congress, S. S. C. (2019). Design and construction of lightweight EPS geofoam embedded geomaterial embankment system for control of settlements. *Geotextiles and Geomembranes*, 47(3), 295–305.

Rahmaninezhad, S. M., & Han, J. (2021). Lateral facing deflections of geosynthetic-reinforced retaining walls under footing loading. *Transportation Geotechnics*, 30, 100594.

Scarborough, J. A. (2005). A Tale of Two Walls: Case Histories of Failed MSE Walls. *GeoFrontiers 2005*, 1–12.

Sheikh, I. R., & Shah, M. Y. (2021). State-of-the-Art Review on the Role of Geocells in Soil Reinforcement. *Geotechnical and Geological Engineering*, 39(3), 1727–1741.

Shukla, S. Kumar., & Yin, J.-Hua. (2006). *Fundamentals of geosynthetic engineering*. Leiden: Taylor & Francis/Balkema.

Shukla, S. K., & Yin, J. H. (2003). Time-dependent settlement analysis of a geosynthetic-reinforced soil. *Geosynthetics International*, 10(2), 70–76.

Suksiripattanapong, C., Horpibulsuk, S., Udomchai, A., Arulrajah, A., & Tangsutthinon, T. (2020). Pullout resistance mechanism of bearing reinforcement embedded in coarse-grained soils: Laboratory and field investigations. *Transportation Geotechnics*, 22, 100297.

Tezcan, S. S., & Buket, Z. S. (1999). *Donatılı zemin istinat duvarları için sayısal örnekler*. İstanbul: Türkiye Deprem Vakfı.

Tos, M., Ozbakan, N., & Evirgen, B. (2023). A Sanding Technique to Improve the Pullout Behavior of Geogrids. *International Journal of Geosynthetics and Ground Engineering*, 9(6).

Wang, Z., Jacobs, F., Ziegler, M., & Yang, G. (2020). Visualisation and quantification of geogrid reinforcing effects under strip footing loads using discrete element method. *Geotextiles and Geomembranes*, 48(1), 62–70.

Ye, Y., Han, J., Liu, H., Rachford, S. M., Parsons, R. L., Dolton, B., & O'Reilly, M. (2022). Pullout resistance of geogrid and steel reinforcement embedded in lightweight cellular concrete backfill. *Geotextiles and Geomembranes*, 50(3), 432–443.

Yoo, C. (2004). Performance of a 6-year-old geosynthetic-reinforced segmental retaining wall. *Geotextiles and Geomembranes*, 22(5), 377–397.

Yoo, C., & Jung, H.-Y. (2006). Case history of geosynthetic reinforced segmental retaining wall failure. *Journal of Geotechnical and Geoenvironmental Engineering*, 132(12).

Zhang, J., Jia, Y., Guo, W., Zhao, J., Ling, J., & Zheng, Y. (2022). Experimental study on the load bearing behavior of geosynthetic reinforced soil bridge abutments with different facing conditions. *Geotextiles and Geomembranes*, 50(4), 632–643.

Zhou, J., Chen, J. F., Xue, J. F., & Wang, J. Q. (2012). Micro-mechanism of the interaction between sand and geogrid transverse ribs. *Geosynthetics International*, 19(6), 426–437.

Ziegler, M. (2017). Application of geogrid reinforced constructions: history, recent and future developments. *Procedia Engineering*, 172, 42–51.

Zornberg, J. G. (2017). Functions and Applications of Geosynthetics In Roadways. *Procedia Engineering*, 189, 298–306.

http-1:https://www.istanbulteknik.com/tr/urundetay/14/fortex-gg-cift-yonlu-geogrid (Retrieved:14/01/2024)

http-2:https://www.tensar.co.uk/solutions/geogrids/triax-tx-geogrid (Retrieved:14/01/2024)

http-3:https://www.linkedin.com/pulse/woven-geogrid-production-wendy-fu/ (Retrieved:14/01/2024)

CURRICULUM VITAE

ORCID ID: 0000-0001-8315-4598

Name Surname : Asker Alp GÜLTEKİN

Foreign Language : English

Education and Professional Background:

- 2024, TUNGE Project, Geotechnical Enigeer
- 2023, INSA Lyon, the GEOMA Laboratory, Intern Geotechnical Engineer
- 2021, Eskişehir Technical University, Engineering Faculty, Civil Engineering Department (3,81/4,00)
- 2020, Nisan Project, Intern Civil Engineer
- 2020, Anatek Company, Researcher
- 2019, Siyah Kalem Engineering and Construction Company, Intern Civil Engineer
- 2019, Brno University of Technology, Engineering Faculty, Civil Engineering Department (ERASMUS+ European Union Student Exchange Program)
- 2017, Anadolu University, English Prep School (B2 Upper Intermediate (73/100))

Publications and/or Scientific/Artistic Activities:

- 2024, TÜBİTAK 2210-A National MSc Scholarship Program, Scientific and Technological Research Council of Türkiye (TÜBİTAK)
- Evirgen, B., Kara, H. O., Ucun, M. S., Gültekin, A. A., Tos, M., and Öztürk, V. (2024). The effect of the geometrical properties of geocell reinforcementsbetween a two-layered road structure under overload conditions. Case Studies in Construction Materials, 20: e02793.
- Evirgen, B., Özbakan, N., Gültekin, A. A., Tos, M., and Tuncan, M. (2024). Liquefaction mitigation using sodium polyacrylate: Large-scale in-situ applications with a unique grouting apparatus. Soil Dynamics and Earthquake Engineering, 179: 108540.
- 2023, Multiple Injection Apparatus Patent, Turkish Patent and Trademark Office

- 2022, TÜBİTAK 1001 The Scientific and Technological Research Project Funding, Scientific and Technological Research Council of Türkiye (TÜBİTAK)
- Gültekin, A. A., and Evirgen, B. (2022). An investigation of the freezing resistance in liquefiable soil containing gel. BSEU Journal of Science, 9(1), 269-276.
- Gültekin, A. A., and Evirgen, B. (2021). The Effect of Various Fences on the Geogrid Performance. 6th International Mediterranean Science and Engineering Congress (IMSEC 2021), Antalya/Türkiye, 726-730.
- 2021, TÜBİTAK 2247-C Intern Researcher Scholarship Program (STAR), Scientific and Technological Research Council of Türkiye (TÜBİTAK)
- 2021, ESTÜ-209 Undergraduate Student Projects, Eskişehir Technical University Scientific Research Projects
- 2021, TÜBİTAK 2209-B Undergraduate Research Program Supported by Industry, Scientific and Technological Research Council of Türkiye (TÜBİTAK)

Awards:

- 2023, 1st, the Best Becholar Degree Thesis in Engineering Faculty, Eskişehir Technical University
- 2021, 1st, the 14th Project Fair Competition, Eskişehir Technical University

Professional Union/Association/Organization Memberships:

- 2024, TMMOB Chamber of Civil Engineers, Türkiye